Superlattice Modulation Spectroscopy of Ultracold Atoms in Optical Lattices

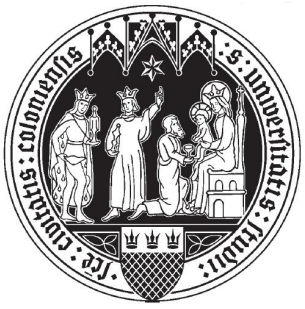

Master Thesis

by

Karla Loida

submitted to

Universität zu Köln

written at

Rheinische Friedrich-Wilhelms-Universität Bonn

supervised by

Prof. Dr. Achim Rosch
Prof. Dr. Corinna Kollath

November 2014

Abstract

We study the influence of a periodic superlattice modulation onto bosonic and fermionic atoms trapped in an optical lattice. The superlattice modulation is applied along one direction and injects momentum into the system which strongly affects the nature of excitations. We study the spectral response within linear response theory, as well as beyond, by employing a time-dependent density matrix renormalization group study. We deduce possible experimental probes that are favored by the distinct type of our perturbation. In the bosonic case, we observe a particularly narrow spectral response which may serve as an accurate measure when calibrating the lattice depth. In the fermionic case, we find strong temperature dependence and propose a new scheme to measure the temperature in the optical lattice. Our proposal is particularly simple in both, theory and experiment, and extends down to remarkably low temperatures, notably below the Néel temperature where antiferromagnetic ordering is expected to occur.

Introduction

Research in the field of quantum phenomena driven by the interplay of a macroscopic number of atoms has been on the rise since the realization of Bose-Einstein Condensation [1–3] and quantum degenerate Fermi gases [4] in the late 90s. In particular, with the realization of effectively strong and tunable interactions, strongly correlated many-body systems have been in the focus. Strong interactions may be achieved in two ways. One option is to employ Feshbach resonances [5] which allow to directly tune the effective scattering length of atoms. The other option is to load ultracold atoms into periodic optical lattice potentials where the suppression of tunneling leads to an effective enhancement of interaction [6]. Ultracold atoms in optical lattices constitute a marvelous laboratory to tackle effects of strong correlations in quantum systems due to the high controllability of parameters, interactions and dimensions by laser light [5]. They have proved to be powerful simulators for the investigation of both, static quantum phases as well as the dynamic evolution of strongly correlated many-body systems. An outstanding example is the first experimental study of the superfluid to Mott-insulator transition of bosonic atoms trapped in an optical lattice [7] in 2002.
From the theory side, ultracold atoms in optical lattices provide a natural realization of various kinds of Hubbard type models [8] that allow one to study the intriguing interplay of quantum kinetic processes and local interaction. Hubbard models are well known from condensed-matter physics where they are typically only rough approximations, though. In contrast, in cold atomic systems Hubbard models may be realized in its cleanest form which enables us to simulate its physics and to test its theoretical predictions in a controlled way. For example, the Mott-insulating phase has been observed in both, bosonic and fermionic, systems [7, 9, 10]. This has led to the concept of quantum simulation which can be viewed as an implementation of Feynman's pioneering ideas for simulating one quantum system by another [11]. Experimentalists have succeeded in mapping out the Bose-Hubbard phase diagram [12]. But many open questions remain concerning for example dynamics or disorder [13].
Many-body phases are quite generally characterized by their excitations. They give insights into the properties of the phase and the underlying physics. For example, the superfluid to Mott-insulator transition is characterized by the opening of a gap in the excitation spectrum when entering the Mott-insulating phase. Excitations may be studied by externally perturbing the system and different approaches have already been intensively investigated in the early stages of optical lattice experiments, in particular probing the superfluid to Mott-insulator transition [7, 14]. However, the physics is much richer and other excitations may occur such as the Higg's amplitude mode in the superfluid phase [15, 16]. We take this as a starting point, that is we aim at finding out more about possible excitations in lattice systems by periodic lattice modulation. We consider a superlattice modulation spectroscopy scheme serving as a probe for both, bosonic and fermionic, atoms confined to optical lattices. As a particular characteristic this perturbation injects momentum π in the system which strongly affects the underlying physics. This contrasts standard lattice shaking setups where momentum is conserved [14, 17].
In Chapter 1 we introduce the physics of ultracold bosons and fermions confined to an

optical lattice and define how we probe the system by superlattice modulation. We then outline the theoretical methods used throughout this work in Chapter 2.
In Chapter 3 we consider ultracold bosons in a one-dimensional optical lattice. The ground state phase diagram is well understood [18–20]. However, dynamics are not and remain an objective of current research. We subject the system to a periodic superlattice modulation and study the nature of excitations, both numerically and analytically. We find interesting dynamics, both deep in the Mott insulating regime as well as close to the phase transition to the superfluid state, due to the particular properties of the superlattice modulation. For instance, the spectral response as usual exhibits a peak around the on-site interaction strength which corresponds to the energy needed to create an excitation. However, the width is strongly reduced compared to standard lattice shaking experiments [14]. The spectral response is sometimes used for lattice depth calibration [21] such that this setup potentially serves as an improved calibration scheme making it attractive for experimentalists as the implementation remains simple.
The low-temperature phase diagram of the fermionic Hubbard model is considerably richer than its bosonic counterpart due to the additional spin degree of freedom. Many details remain unknown since computational studies of fermionic systems are severely limited. The concept of quantum simulation is expected to provide answers to various open questions such as frustrated magnetism and d-wave superfluidity [22]. There has been progress in fermionic experiments and the strongly correlated regime of the repulsive Fermi-Hubbard model is indeed accessible in experiment. The observation of a Mott-insulating state [9, 10] was possible not long after the first Fermi gas in a lattice was prepared [23]. However, experiments still encounter difficulties. One of the challenges is a further reduction in temperature to probe regimes of interesting physics. Additionally, the possibilities to probe these systems in order to accurately characterize them are still very limited. In particular, experimentalists lack reliable methods to adequately measure the temperature of a Fermi gas confined to an optical lattice which is a key ingredient in experimentally determining the Fermi-Hubbard phase diagram. Consequently, the development of new thermometry schemes constitutes a tantalizing challenge. In Chapter 4 we propose a scheme to directly measure the temperature of fermionic atoms confined to an optical lattice by superlattice modulation and we specify the experimental implementation in great detail. It is temptingly simple, in both theory and experiment, and works down to very low temperatures of about 10% of the hopping strength that have not been observed in experiment so far.

Contents

Chapter 1.

Physics of cold atomic gases in optical lattices

Ultracold atoms in a periodic trapping potential constitute a physical system which is closely related to systems in condensed matter physics. The basic physical mechanism to create a periodic lattice potential for neutral atoms [6] is the optical dipole interaction between the atoms and a light field [24, 25]. The light-induced dipole moment of the atom interacts with the light field which causes a shift of the energy levels of the atom. This is called the ac-Stark shift. If the light field is sufficiently far detuned from the atomic resonance, the number of optical excitations is low such that the dissipative radiation force due to photon scattering is negligible compared to the optical dipole force. The energy shift can then be used to create a conservative trapping potential for neutral atoms which is proportional to the light intensity. Thus, spatially modulated light fields lead to space-dependent potentials, for example optical lattices. One possibility to create such a lattice potential in three dimensions is to orthogonally superimpose three retro-reflected laser beams with polarizations between the three standing waves that are mutually orthogonal [25]. In this simple three-dimensional case the optical lattice potential is of the form

$$V_0(\vec{x}) = V_0 \sum_{d=1}^{3} \sin^2(k_d x_d), \tag{1.1}$$

with wave vector $k_d = 2\pi/\lambda_d$, where λ_d is the laser wave length in each direction $d = x, y, z$.

1.1. Bosonic atoms in optical lattices

An ultracold gas of bosonic atoms in an optical lattice can be described by a Bose-Hubbard model in a wide range of parameters,

$$H_{\mathrm{BH}} = -J \sum_{\langle j,j' \rangle} (a^\dagger_{j,\sigma} a_{j',\sigma} + \mathrm{h.c.}) + \frac{U}{2} \sum_j n_j(n_j - 1), \tag{1.2}$$

where a_j and $a^\dagger_j$ represent the bosonic annihilation and creation operators at site j, $n_j = a^\dagger_j a_j$ is the local particle number operator and $\langle j, j' \rangle$ denotes nearest-neighbors. The hopping amplitude J, which is the tunneling matrix element, characterizes the kinetic part and the on-site interaction strength is given by U. The system parameters J and U are controlled by laser light. In tight-binding theory one can deduce the Bose-Hubbard model starting from the Hamiltonian operator for bosonic atoms in an

external trapping potential [8]

$$H = \int \mathrm{d}^3x\ \Psi^\dagger(\vec{x}) \left(-\frac{\hbar^2}{2m}\nabla^2 + V_0(\vec{x}) + V_T(\vec{x}) \right) \Psi(\vec{x}) \tag{1.3}$$

$$+\frac{1}{2}\frac{4\pi a_s \hbar^2}{m} \int \mathrm{d}^3x \Psi^\dagger(\vec{x})\Psi^\dagger(\vec{x})\Psi(\vec{x})\Psi(\vec{x}), \tag{1.4}$$

where $\Psi(\vec{x})$ is a bosonic field operator, $V_0(\vec{x})$ is the optical lattice potential and $V_T(\vec{x})$ is an additional trapping potential. As mostly done, we assume that the complicated inter-atomic potential can be replaced by an effective contact interaction $U(\vec{x}) = 4\pi\hbar^2 a_s/m \cdot \delta(\vec{x})$, where a_s is the s-wave scattering length and m is the mass of the atoms. This is valid for a wide range of situations in dilute atomic gases as long as no longer-range interactions contribute such as for example the dipole-dipole interaction in dipolar gases [5].
We consider a general periodic potential $V_0(\vec{x}) = V_0(\vec{x} + \vec{x}_i)$ where $\vec{x}_i$ is the position of the i^{th} lattice site. According to Bloch's theorem, single-particle eigenstates are described by Bloch waves $\Phi^n_{\vec{k}}(\vec{x})$ of discrete band index n and quasimomentum $\vec{k}$ within the first Brillouin zone of the reciprocal lattice [26]. We can construct an alternative single-particle basis from a combination of Bloch functions. The so-called Wannier functions are obtained by summing over all quasimomenta $\vec{k}$ in the first Brillouin zone,

$$w_n(\vec{x} - \vec{x}_i) = \frac{1}{\sqrt{N}} \cdot \sum_{\vec{k}} \mathrm{e}^{-i\vec{k}\vec{x}_i} \Phi^n_{\vec{k}}(\vec{x}), \tag{1.5}$$

where N is a normalization constant. The Wannier functions are typically well localized on individual lattice sites i.
The strength of the lattice potential V_0 is conveniently measured in units of the recoil energy $E_r = (\hbar k)^2/2m$ where k is the laser wavelength. For deep lattices $V_0 \gg E_r$ each well can be approximated by a harmonic trapping potential with energy levels $\hbar\omega_0 = 2E_r\sqrt{V_0/E_r} \gg E_r$. Each well supports a number of vibrational levels. One assumes the energies involved in the system dynamics, i.e. recoil energy E_r, on-site interaction strength U and temperature T, to be small compared to excitation energies to the second band at a distance of $\hbar\omega_0$ from the lowest band. Atoms are then restricted to the lowest vibrational level at each site, remaining in the lowest Bloch band. One obtains the Bose-Hubbard Hamiltonian by expanding the field operators in the Hamiltonian operator in the Wannier basis

$$\Psi(\vec{x}) = \sum_i a_i w(\vec{x} - \vec{x}_i), \tag{1.6}$$

where we drop the band index n because only the lowest vibrational level is considered as justified above. The kinetic energy is frozen except for a small tunneling amplitude to neighboring sites which leads to a finite width of the lowest Bloch band. The strength of the on-site interaction is given by

$$U = \frac{4\pi\hbar^2 a_s}{m} \int d^3x |w(\vec{x})|^4. \tag{1.7}$$

The tunneling matrix element between neighboring lattice sites i and j is given by

$$J = \int \mathrm{d}^3x w^*(\vec{x} - \vec{x}_i) \left[-\frac{\hbar^2}{2m}\nabla^2 + V_0(\vec{x}) \right] w(\vec{x} - \vec{x}_j). \tag{1.8}$$

The nearest-neighbor repulsion and the next-nearest-neighbor tunneling amplitude are typically two orders of magnitude smaller and can be neglected [8]. For the cubic lattice given by (1.1) and in the limit $V_0 \gg E_r$, the hopping amplitude J and the on-site repulsion U can be explicitly calculated [5, 27],

$$J(V_0) = \frac{4}{\sqrt{\pi}} E_r \left(\frac{V_0}{E_r}\right)^{3/4} e^{-2\sqrt{V_0/E_R}}, \tag{1.9}$$

$$U(V_0) = \sqrt{\frac{8}{\pi}} k a_s E_r \left(\frac{V_0}{E_r}\right)^{3/4}, \tag{1.10}$$

where U is calculated for a Gaussian ground state in the local oscillator approximation. The kinetic energy drops exponentially whereas the interaction energy increases for increasing V_0/E_r.
For the general periodic potential, the tunneling matrix element in a given band n connecting lattice sites of arbitrary distance $\vec{x}_i$, $J_n(\vec{x}_i)$, is also directly related to the Bloch band energies $\epsilon_n(\vec{k})$ [5] via

$$\epsilon_n(\vec{k}) = \sum_{\vec{x}_i} J_n(\vec{x}_i) e^{i\vec{k}\vec{x}_i}. \tag{1.11}$$

This formula provides a practical way to determine the hopping amplitudes as $\epsilon_n(\vec{k})$ can be determined from numeric band structure calculations.

The Bose-Hubbard model at commensurate filling $\bar{n}$ exhibits a quantum phase transition between a superfluid phase of delocalized nature and a Mott-insulating phase of localized nature at a critical value of U/J as first discussed in [18]. The qualitative structure is similar in one-, two- or three-dimensional lattices and a schematic drawing of the phase diagram at commensurate filling $\bar{n}$ is shown in Figure 1.1. Quantitatively, there is considerable differences between the different dimensions. However, we will focus on general aspects and the one-dimensional case here.
In the superfluid phase, the ground state wave function consists of delocalized wave functions and local number fluctuations are large. The single-particle dispersion is linear at low energies and becomes particle-like at higher energies. The ground state wave function in the limit $U = 0$ is given by

$$|GS\rangle = \frac{1}{\sqrt{N!}} (a_{k=0}^\dagger)^N |0\rangle, \tag{1.12}$$

where N is the number of particles and

$$a_k = \frac{1}{\sqrt{L}} \sum_j \mathrm{e}^{-ikaj} a_j \tag{1.13}$$

with lattice spacing a. All particles occupy the same momentum state of $k = 0$ and are delocalized over the entire lattice. The ground state energy is $E_{GS} = -2NJ$. The low-energy excitation spectrum is continuous for $L \to \infty$.
In contrast, the Mott-insulating ground state consists of localized wave functions. In this case, local density fluctuations become energetically costly and are suppressed at commensurate filling. Low energy excitations are localized defects of energy U. In the atomic limit $J = 0$, the ground state wave function for a filling $\bar{n} = 1$ is given by

$$|GS\rangle = \prod_{j=1}^{L} a_j^\dagger |0\rangle, \tag{1.14}$$

where L is the number of lattice sites. The ground state energy is $E_{GS} = 0$. The first excited state consists of one site being occupied by two particles and one site being empty. The energy of the first excited state is $E_1 = U$ such that a finite excitation energy is needed to create a local defect. This is the so-called Mott gap. One essential

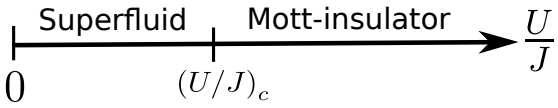

Figure 1.1. – Qualitative sketch of the zero temperature phase diagram of the homogeneous Bose-Hubbard model at commensurate filling $\bar{n}$. A quantum phase transition between the delocalized superfluid phase and the localized Mott-insulating occurs at a critical value $(U/J)_c$.

feature of the phase transition is that this gap opens in the excitation spectrum when entering the Mott-insulating phase. The quantum phase transition in one dimension is of Kosterlitz-Thouless type and occurs at a critical value of $(U/J)_c \sim 3.4$ for a filling $\bar{n} = 1$ [20, 28–30].

1.2. Fermionic atoms in optical lattices

Analogously to the preceding bosonic case, interacting fermions in a periodic potential can be described by the Hubbard Hamiltonian in a wide range of parameters as long as the lattice is sufficiently deep and temperatures are sufficiently low such that the single band tight-binding approximation applies. The single band Hubbard model for fermionic particles is given by

$$H_{FH} = -J \sum_{\langle j,j' \rangle,\sigma} (c^\dagger_{j,\sigma} c_{j',\sigma} + \text{h.c.}) + U \sum_j n_{j,\uparrow} n_{j,\downarrow} - \mu \sum_{j,\sigma} n_{j,\sigma}, \tag{1.15}$$

where $c^\dagger_{j,\sigma}$ and $c_{j,\sigma}$ are the local fermionic creation and annihilation operators, $n_{j,\sigma}$ is the local number operator, μ is the chemical potential, $\langle j, j' \rangle$ denotes nearest neighbors and the spin σ corresponds to two different hyperfine states. The reduction to tight-binding starting from the Hamiltonian operator for fermionic atoms in an optical lattice potential is analogous to the bosonic case described in 1.1.
This model was originally introduced to describe electrons in a solid [31] that have spin 1/2 where $\sigma = \uparrow, \downarrow$ denotes the two eigenstates of opposite spin. The hopping J conserves this internal spin degree of freedom. Local interaction U is only possible between two opposite spins since the Pauli principle prevents two fermions of same spin to be on the same site. In good metals the Coulomb interaction between electrons is typically screened with a short screening length of the order of the lattice spacing which justifies the replacement by a local interaction U [26]. However, the Hubbard model remains an approximation in metals where the screening length may vary and discrepancies to the pure Hubbard model inevitably occur. In contrast, ultracold fermions in optical lattices constitute a clean realization of this model [22] in a wide range of parameters.

The underlying physics is diverse and rich. Intriguing quantum phenomena occur due to fermionic statistics and the spin degree of freedom, reaching from liquids to Mott-insulators and long-range antiferromagnetic order. In Figure 1.2 the phase diagram of the homogeneous Hubbard model for a three-dimensional cubic lattice with commensurate filling of one particle per site is shown [32,33]. At moderate temperatures, when increasing the repulsive coupling U/J one crosses over from a metallic phase (fermionic

liquid) at weak interactions to an incompressible Mott-insulator at larger interactions through some intermediate state which is a 'bad metal' or poor insulator [34]. At strong interactions charge fluctuations are suppressed. The lowest excitations are particle-hole like and cost an energy $\Delta \sim U$. The dash-dotted line indicates the opening of the Mott gap Δ when entering the incompressible Mott-insulator. At lower temperatures below the Néel temperature $T_N(U)$ antiferromagnetic long-range order occurs in which spin and translational symmetries are broken. The transition is indicated by the solid line in Figure 1.2. The transition is of different physical character depending on what phase the transition line is approached from. At strong coupling and small temperatures where the temperature is much smaller than the Mott gap, particles are localized in a Mott-insulating state and density fluctuations are frozen out. Only spin degrees of freedom are active that are described by an effective Heisenberg model. At $U \gg J$ the so-called superexchange process occurs which is a second order hopping process of neighboring fermionic particles, via an intermediate doubly occupied state which is highly energetic, with coupling strength $4J^2/U$. Spin ordering occurs as a low-energy instability as soon as the temperature drops below the Néel temperature T_N which is controlled by the antiferromagnetic super-exchange coupling $T_N \propto J^2/U$. In contrast, at weak coupling the transition from the liquid phase where density fluctuations are high, a distinction between charge order (blocking of translational degrees of freedom) and long-range magnetic order is not possible. The transition to long-range magnetic order directly corresponds to spin ordering described by a spin-density wave picture where opening of the charge gap and antiferromagnetic order occur simultaneously.

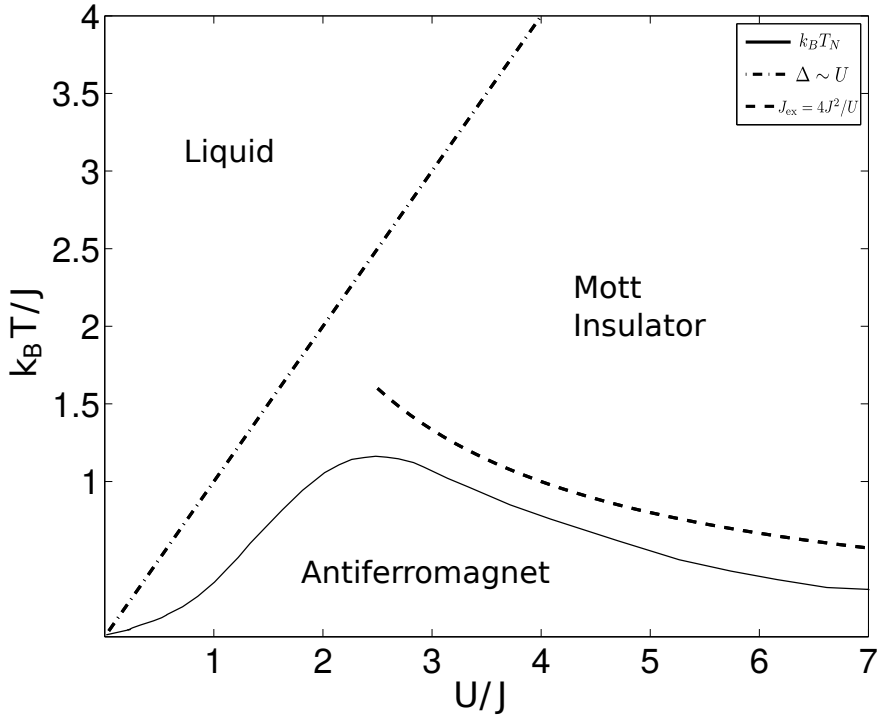

Figure 1.2. – Qualitative sketch of the finite temperature phase diagram of the homogeneous Hubbard model for a three-dimensional cubic lattice at half-filling. At moderate temperatures a crossover from a Fermi liquid phase to a Mott-insulating phase takes place when the Mott gap (dash-dotted line) opens. At lower temperatures a phase transition (solid line) into a long-range ordered antiferromagnetic phase occurs.

The ratio U/J controls the strength of interaction effects and a wide range is already accessible in cold atom experiments. The hopping J may be controlled by changing the lattice depth of the optical lattice and U can be directly changed by Feshbach resonances [5]. By using Feshbach resonances, one can tune the scattering length a_s from attractive to repulsive and thus also adjust to zero interaction $U = 0$. Ultimately, the hope is to use fermionic atoms in optical lattices to measure the full Fermi-Hubbard phase diagram.

1.3. Probing cold atomic gases in optical lattices

As motivated in the Introduction many-body phases are quite generally characterized by their excitations which may be studied by externally perturbing the system. For example, the system may be excited by introducing a potential gradient that tilts the lattice. Tunneling in the Mott-insulating regime becomes possible as soon as the potential difference between neighboring sites is approximately of the order of the on-site interaction U [7]. Alternatively, one can excite the system by periodically modulating the amplitude of the lattice [14]. Both experiments observe a broad excitation spectrum in the superfluid regime and the observations at stronger interactions agree with a gapped spectrum. But the physics of these phases is even richer and other excitations are possible in the system such as the Higg's amplitude mode which is gapped deep in the superfluid region which was experimentally probed by periodically modulating the lattice amplitude [16]. However, many details of these phases remain unknown and further studies of the Bose-Hubbard and Fermi-Hubbard phase diagrams are an objective in current research.
The aim of this project is to find out more about possible excitations in the system by periodic lattice modulation. The modulation we choose is incommensurate with the underlying equilibrium lattice in contrast to the commensurate amplitude modulation in reference [14].

The perturbation The basic setup is the following. We consider an optical lattice in one dimension given by Equation (1.1) restricted to one direction. We superimpose a second laser of half or twice the wavelength which creates a so-called superlattice. We periodically modulate the superlattice amplitude with frequency ω that is much smaller than the laser frequency and with a small amplitude of modulation. The exact experimental setup may be adjusted in such a way that the bottom offset of the superlattice is constant and the periodic modulation changes between the two configurations as shown in Figure 1.3 within half the modulation period $T = 2\pi/\omega$.

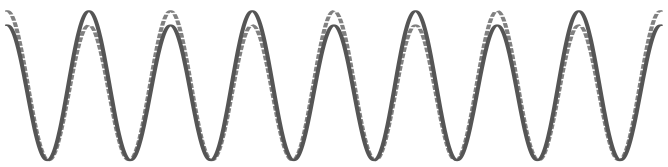

Figure 1.3. – Periodic modulation of the superlattice amplitude with frequency ω and a small amplitude of the modulation h between the two configurations that are indicated by solid and dashed lines.

The potential created is of the form

$$V(x) = V_0(x) + \delta V(x,t), \tag{1.16}$$

where $V_0(x)$ is the equilibrium lattice potential created by the first laser beam. The perturbation

$$\delta V(x,t) = h\sin(\omega t)\tilde{V}(x) \tag{1.17}$$

is of small amplitude h and explicitly time-dependent. If the wells are sufficiently deep, the superlattice Wannier functions may be approximated by their $V_0(x)$-solutions such that $U(V(x)) \approx U(V_0) = U$ given by equation (1.10). For the hopping amplitude we replace V_0 by $V_0 + \delta V(x,t)$ in equation (1.9) and expand in the small perturbation such that the lattice modulation translates into a modulation of the hopping parameter in the lattice description,

$$J_j(t) = -(J + h(-1)^j \sin(\omega t)). \tag{1.18}$$

This is a reasonable approximation for sufficiently small perturbations. Defining the full problem the following explicitly time-dependent many-body Hamiltonian is induced

$$H = H_0 + H_{\text{pert}}, \tag{1.19}$$

where the equilibrium Hamiltonian H_0 is given by the Bose-Hubbard Hamiltonian (1.2) or the Fermi-Hubbard Hamiltonian (1.15) depending on the kind of particles trapped in the lattice. Thus, the perturbation is of the following form

$$H_{\text{pert}} = h\sin(\omega t)O_{\text{B,F}}, \tag{1.20}$$

$$O_B = \sum_j (-1)^j (a_j^\dagger a_{j+1} + \text{h.c.}), \tag{1.21}$$

$$O_F = \sum_{j,\sigma} (-1)^j (c_{j,\sigma}^\dagger c_{j+1,\sigma} + \text{h.c.}), \tag{1.22}$$

with a small amplitude of the perturbation $h \ll J$ and the superlattice or dimerized hopping operator $O_{B,F}$ to which it couples. We denote bosons by B and fermions by F. Throughout this work we set the energy scale by choosing $J = 1$ and $\hbar \equiv 1$ except for some cases where we insert experimental parameters and units.
An important characteristic of the superlattice operator O is that it does not conserve momentum. The perturbation introduces an extra momentum kick of π into the system. This is due to the dimerization which doubles the size of the unit cell and this strongly affects the nature of possible excitations. This may be directly seen from the Fourier transform of the perturbing operator. We show this exemplified for the bosonic case. We set lattice spacing $a \equiv 1$ and introduce the Fourier transform $a_j = (1/\sqrt{L})\sum_k \exp(ikj)a_k$. The perturbing operator becomes

$$O = 2i\sum_k \sin(k) a_{k+\pi}^\dagger a_k, \tag{1.23}$$

where $k = 2\pi q/L$, $m = 1, ..., L$. A particle of momentum k is annihilated and a particle of momentum $k+\pi$ is created by the operator which adds momentum π to the system. In the case of the bosonic Mott insulator with integer filling this gives rise to an intuitive interpretation. The action of $a_{k+\pi}^\dagger$ may be interpreted as the creation of a doublon of momentum $k_d = k + \pi$ and a_k as the creation of a hole of momentum $k_h = -k$ such that the center of mass momentum of the created pair is given by $k_d + k_h = \pi$.

The measurement The perturbation injects energy into the system such that the study of the energy absorbed by the system gives information about the excitations in the system and insights into the underlying physics. In standard lattice shaking experiments with bosonic atoms the energy absorbed by the system is estimated from the broadening of the central peak of the momentum distribution measured in a time-of-flight absorption image after sudden switch off [14, 35]. However, in the case of fermionic atoms this is not a good measure for the absorbed energy since the momentum distribution is broad and less sensitive to heating. We will show how a measure of the quasimomentum distribution $\langle n_k(t)\rangle$ constitutes a reliable method to study the absorbed energy in the particular case of exciting to higher Bloch bands. This is experimentally appealing because the quasimomentum distribution may be measured fairly easily by adiabatic band mapping [25]. The basic idea of this technique is to ramp down the lattice adiabatically such that crystal (quasi) momentum is conserved in contrast to a sudden switch off. Adiabatic means slow compared to the vibrational frequencies in the lattice but fast enough such that the population of the energy bands does not change during ramp down. Each state with crystal momentum k is finally mapped onto a free particle state with momentum k when the lattice is completely switched off. A particle in the n^{th} energy band is mapped onto the n^{th} momentum interval of the free particle. In a time-of-flight absorption image particles from the n^{th} energy band appear in the n^{th} Brillouin zone. Applying adiabatic band mapping after a certain duration t of the perturbation gives access to the quasimomentum distribution $\langle n_k(t)\rangle$ which, multiplied by the perturbing frequency, yields the absorbed energy. This is limited as a probe if exciting within the lowest band because excitations are not clearly separated from the initial distribution. However, if we excite at higher frequencies to higher Bloch bands, measuring the absorbed energy wraps up to counting the particles appearing in higher Brillouin zones in the absorption image. Higher Brillouin zones are initially empty such that this gives an accurate measure of the absorbed energy and constitutes a promising alternative for experimentalists. We discuss this in detail in Section 4.4.2.

Chapter 2.

Theoretical methods

In this chapter we introduce the methods which are used throughout this work. In Section 2.1 we introduce linear response theory for quantum systems which is a general method used to compute observables of a problem consisting of an equilibrium Hamiltonian to which a small time-dependent perturbation is added. We apply linear response in many problems throughout this work. In Section 2.2 we discuss the local density approximation which treats the presence of an additional external trapping potential in cold atom experiments as a spatially varying chemical potential. We need this in Chapter 4 where we consider a realistic experimental situation. Finally, we introduce the time-adaptive density matrix renormalization group method in Section 2.3 which is a variational scheme particularly suited for the physics of one-dimensional lattice systems. We apply this in Chapter 3 in order to go beyond linear response.

2.1. Linear response theory

General aspects Consider a system described by a time-independent equilibrium Hamiltonian H_0. In order to probe the properties of such a system, one may act onto it with a small perturbation and study how the system responds to this perturbation [36]. The perturbation is described by an additional time-dependent Hamiltonian H_{pert}. Computing the full properties of the time dependent Hamiltonian $H = H_0 + H_{\text{pert}}$ would be an ambitious task. However, one may compute the expectation values of observables in linear response theory by assuming a small perturbation and doing a perturbative expansion. The general time and space dependent perturbation can be written as

$$H_{\text{pert}} = \int \mathrm{d}\vec{r}\, h(\vec{r},t) O(\vec{r}), \tag{2.1}$$

where $h(\vec{r},t)$ is some external field, which is considered to be small and will be switched on slowly, and $O(\vec{r})$ is the operator to which it couples. To simplify notation one chooses $\langle O(\vec{r})\rangle = 0$ in the absence of the perturbation. The aim is to calculate the expectation value of some physical observable $A(\vec{r})$ at point $\vec{r}$ and time t. The operator A is chosen such that its average in the unperturbed system vanishes. The average with respect to the time-dependent Hamiltonian may be computed by expanding the perturbation in powers of h. By definition the term of zero order vanishes as $\langle A(\vec{r})\rangle_0 = 0$. In first order (linear response) one finds

$$\langle A(\vec{r})\rangle_t = \int \mathrm{d}\vec{r}\,' \int_{-\infty}^{t} \mathrm{d}t' h(\vec{r}\,',t') \chi(\vec{r},\vec{r}\,',t,t'), \tag{2.2}$$

$$\text{with} \quad \chi(\vec{r},\vec{r}\,',t,t') = -i\theta(t-t')\langle \big[A(\vec{r},t), O(\vec{r}\,',t')\big]\rangle_0, \tag{2.3}$$

where $\chi(\vec{r},\vec{r}\,',t,t')$ is the complex susceptibility and $\langle\cdot\rangle_0$ denotes averages taken with respect to the unperturbed Hamiltonian H_0. Operators $O(t)$ are given in the Heisenberg

representation with respect to H_0. The problem is thus reduced to calculating equilibrium expectation values of the system described by H_0. Or, the other way around, one obtains information about equilibrium correlation functions by studying the response. The θ-function ensures causality as a measure at time t can only depend on the perturbation at earlier times. Assuming translationally invariant systems $\langle A(\vec{r})\rangle_t = \langle A(\vec{r'})\rangle_t$ and using that χ is an equilibrium quantity that only depends on the time difference of operators, thus $\chi(\vec{r},\vec{r}',t,t') = \chi(\vec{r}-\vec{r}',t-t')$, one can compute the Fourier transform

$$F(\vec{q},\omega) = \int \mathrm{d}\vec{r} \int_{-\infty}^{+\infty} \mathrm{d}t e^{-i(\vec{q}\vec{r}-\omega t)} F(\vec{r},t), \tag{2.4}$$

$$\langle A(\vec{q},\omega)\rangle = \chi(\vec{q},\omega)h(\vec{q},\omega). \tag{2.5}$$

In the case of χ, convergence for $t \to -\infty$ is ensured by replacing $\omega \to \omega + i\delta$. This corresponds to adding an infinitesimal positive imaginary part to the frequency as δ is an infinitesimal positive number.

The fluctuation dissipation theorem As the perturbation injects energy into the system, energy is no longer conserved in the presence of a time-dependent perturbation. The change of energy $dE(t)/dt = \langle dH(t)/dt\rangle$ brought into the system by the perturbation may be determined in linear response theory. In the case of a simple periodic perturbation of the form

$$H_{\mathrm{pert}} = Ohe^{i\omega t} + O^\dagger h^* e^{-i\omega t}, \tag{2.6}$$

and after averaging over one period $T = 2\pi/\omega$ of the perturbation, one can determine the average rate of dissipation $\overline{dE(t)}/dt$.

$$\frac{\overline{dE(t)}}{dt} = \frac{1}{T}\int_0^T \mathrm{d}t\ \frac{dE(t)}{dt} = -2\omega h h^* Im\chi_{OO^\dagger}(\omega), \tag{2.7}$$

$$\chi_{OO^\dagger}(\omega) = \int \mathrm{d}t\ e^{i(\omega+i\delta)t}\chi_{OO^\dagger}(t), \tag{2.8}$$

$$\chi_{OO^\dagger}(t) = -i\theta(t)\langle\Big[O(t),O^\dagger(0)\Big]\rangle_0, \tag{2.9}$$

which is known as the fluctuation dissipation theorem and where one uses $\chi(\omega)^* = \int_0^{+\infty}\mathrm{d}t\langle\big[O(t),O^\dagger(0)\big]\rangle e^{-i\omega t} = \chi(-\omega)$. The energy absorption rate $\overline{dE(t)}/dt$ is proportional to the energy ω and the absolute value squared of the field amplitude $|h|^2$. The linear term in h is zero. It is controlled by the imaginary part of the susceptibility which depends on an equilibrium correlation function. This result obviously is a powerful tool in two directions. On the one hand, by slightly perturbing the system one can probe the various correlations and physical properties of the unperturbed system. On the other hand, as soon as one is able to compute the correlations of the system in equilibrium, the fluctuation dissipation theorem provides a practical tool to compute the response of a system. Both ways are equally important but the latter way is what we take advantage of here to compute the response of the system to the periodic driving by superlattice modulation. Note that our perturbation chosen is of $\sin(\omega t)$-form such that Equation (2.7) becomes

$$\frac{\overline{dE(t)}}{dt} = -\frac{1}{2}\omega|h|^2 Im\chi_{OO^\dagger}(\omega). \tag{2.10}$$

The spectral representation In many cases the imaginary part of the complex susceptibility is more conveniently expressed in the so-called spectral representation. The spectral representation is a formal decomposition which avoids having to calculate the complex susceptibility in the time domain $\chi_{OO^\dagger}(t)$. We introduce a complete basis $|n\rangle$ which consists of the eigenstates of the unperturbed Hamiltonian H_0, $H_o|n\rangle = E_n|n\rangle$. One can rewrite the complex susceptibility 2.9. For finite temperature expectation values $\langle O\rangle = Tr\left[\exp(-\beta H_0)O\right]/Z$ and with the help of the closure relation $1 = \sum_m |m\rangle\langle m|$ one obtains

$$\chi_{OO^\dagger}(t) = -i\theta(t)\frac{1}{Z}\sum_{n,m} e^{i(E_n-E_m)t}|\langle m|O|n\rangle|^2(e^{-\beta E_n} - e^{-\beta E_m}), \tag{2.11}$$

where the definition of the Heisenberg operators $O(t) = \exp(iH_0t)O\exp(-iH_0t)$ and that $|n\rangle$ is an eigenstate of H_0 was used. The Fourier transform (2.8) gives

$$\chi_{OO^\dagger}(\omega) = \frac{1}{Z}\sum_{n,m}|\langle m|O|n\rangle|^2\frac{e^{-\beta E_n} - e^{-\beta E_m}}{\omega + E_n - E_m + i\delta}, \tag{2.12}$$

$$\mathrm{Im}\chi_{OO^\dagger}(\omega) = -\frac{\delta}{Z}\sum_{n,m}|\langle m|O|n\rangle|^2\left(e^{-\beta E_n} - e^{-\beta E_m}\right)\frac{1}{\delta^2 + (\omega + E_n - E_m)^2}, \tag{2.13}$$

$$= -\frac{\pi}{Z}\left(1 - e^{-\beta\omega}\right)\sum_{n,m}|\langle m|O|n\rangle|^2 e^{-\beta E_n}\delta\left(\omega + E_n - E_m\right), \tag{2.14}$$

where we used the definition of Dirac's delta function by Cauchy's distribution $(1/\pi)\cdot\delta/(\delta^2 + (\omega-\omega_0)^2) \to \delta(\omega-\omega_0)$, for $\delta \to 0$. A transition from an initial state $|n\rangle$ to a final state $|m\rangle$ is possible when the system absorbs the energy $\hbar\omega$ introduced by the perturbation. The probability of the transition is proportional to the square of the matrix element coupling the two states $|\langle m|O|n\rangle|^2$. The conservation of energy is ensured by $\delta\left(\omega + E_n - E_m\right)$. At zero temperature one analogously obtains

$$\mathrm{Im}\chi_{OO^\dagger}(\omega) = -\pi\sum_{n,m}|\langle m|O|n\rangle|^2\delta\left(\omega + E_n - E_m\right), \tag{2.15}$$

restricted to the positive frequency sector.

2.2. The local density approximation

In current experimental setups the presence of an additional external trapping potential for the atomic cloud has to be taken into account. It considerably effects the physics of the system. The full Hamiltonian (without an additional superlattice modulation) is given by

$$H = H_{BH/FH} + \sum_{j,\sigma} V(\vec{r}_j)n_{j,\sigma}, \tag{2.16}$$

where $V(\vec{r}_j)$ is the space dependent external trapping potential, the Bose-Hubbard and Fermi-Hubbard Hamiltonian $H_{BH/FH}$ are given by Equations (1.2) and (1.15) respectively, and the spin index σ drops out in the bosonic case. The consequences on the observed physics may be discussed within the local density approximation [34] which treats the external potential $V(\vec{r})$ as a spatially varying chemical potential. Parabolic confinement is usually a good approximation in experiment at the position of the atomic

cloud. However, one may consider a more general form of the trapping potential $V(\vec{r}) = V_t(|\vec{r}|/a)^\alpha$ of exponent α, where $\vec{r}$ is the position vector in d dimensions, a is the lattice spacing and V_t is the strength of the external confinement. In the parabolic case $\alpha = 2$. The space-dependent chemical potential becomes

$$\mu(r_j) = \mu_0 - V_t \left(\frac{|r_j|}{a} \right)^\alpha, \tag{2.17}$$

where r_j denotes the d-dimensional position vector labeling each lattice site and μ_0 is the chemical potential in the center of the trap. Within the local density approximation, any local observable $O(r_j)$ in the trap is related to its counterpart in the homogeneous system (without trap) $O_h(\mu)$ by

$$O(r_j) = O_h(\mu(r_j)). \tag{2.18}$$

This leads to the coexistence of different phases in the trap because the local density changes when moving through the trap. The local density approximation can be used with good accuracy in many cases [37]. However, results are poor for very deep and narrow traps where the potential varies rapidly from site to site and close to a phase transition due to proximity effects. There is no clear phase boundary between spatially separated different phases since particles from one phase may leak into the neighboring one at the boundary. The local density approximation neglects this and the density distribution has to be calculated numerically to incorporate this.
The total number of atoms in the trap may be obtained by summing the space-dependent local occupancy over the whole system and using the continuum limit. One obtains

$$N = \sum_j n_j \approx \frac{\Omega_{d-1}}{a^d} \int \mathrm{d}r \; r^{d-1} n_h(r), \tag{2.19}$$

$$= \left(\frac{D}{V_t} \right)^{d/\alpha} \frac{\Omega_{d-1}}{\alpha} \int_{-\infty}^{\bar{\mu}_0} \mathrm{d}\bar{\mu} (\bar{\mu}_0 - \bar{\mu})^{\frac{d}{\alpha}-1} n_h(\bar{\mu}), \tag{2.20}$$

where $n_h(r)$ is the density in the homogeneous system and Ω_{d-1} is the surface of a sphere in d dimensions, e.g. $\Omega_0 = 2$, $\Omega_1 = 2\pi$ and $\Omega_2 = 4\pi$. The dimensionless chemical potential is given by $\bar{\mu} = \mu/D$ where D is the half bandwidth. Note that $D = zJ$ in the Fermi-Hubbard model where J denotes the hopping parameter and z is the number of nearest neighbors. One defines the characteristic density

$$\rho = N \left(\frac{V_t}{D} \right)^{d/\alpha} = \frac{\Omega_{d-1}}{\alpha} \int_{-\infty}^{\bar{\mu}_0} \mathrm{d}\bar{\mu} (\bar{\mu}_0 - \bar{\mu})^{\frac{d}{\alpha}-1} n_h(\bar{\mu}). \tag{2.21}$$

This is a dimensionless combination which does not depend on the strength of the confining potential. It can be used to describe properties of experimental systems regardless of the particular realization of the trap. It can be experimentally controlled by either changing the total number of particles N or by reducing D through increasing the lattice depth.
Mean values of local observables are given by

$$\bar{O} = \frac{1}{N} \sum_j O_j = \frac{\Omega_{d-1}}{\rho\alpha} \int_{-\infty}^{\bar{\mu}_0} \mathrm{d}\bar{\mu} (\bar{\mu}_0 - \bar{\mu})^{\frac{d}{\alpha}-1} O_h(\bar{\mu}). \tag{2.22}$$

From this expression it becomes evident that observables only depend on the characteristic density ρ and on the chemical potential μ_0 in the center of the trap. Note that μ_0 itself only depends on ρ. Thus, all local quantities on the central site and all global quantities depend on ρ. As a consequence, the state diagram of the inhomogeneous system only depends on the effective density ρ and not on the particle number N and the trapping V_t separately. The effective density changes for a fixed particle number N when varying either the trapping potential V_t or the lattice depth which corresponds to a variation of D. In contrast, the density of the homogeneous system is determined by the number of particles N present in the system and stays unchanged if the lattice depth is varied for a given particle number N.

2.3. The time-dependent density matrix renormalization group method in terms of matrix product states

The time-dependent density matrix renormalization group method (t-DMRG) is currently the most powerful method in the study of statics and dynamics of one dimensional strongly correlated lattice systems. It was invented by S. R. White in 1992 [38]. The basic problem in quantum many-body systems is that the Hilbert space of a system of size L grows exponentially with size d^L where d is the local dimension. DMRG is an iterative variational method that reduces the degrees of freedom at each iteration to the most important ones. In the following we introduce the basic concepts choosing a formulation in terms of matrix product states [39].

Singular value decomposition The basic tool which is extensively used throughout DMRG-algorithms is the so-called singular value decomposition. It is a theorem from linear algebra which states that an arbitrary rectangular matrix M of dimensions $(m \times n)$ can be decomposed as

$$M = USV^\dagger, \tag{2.23}$$

where

- U is a unitary matrix, $U^\dagger U = \mathbb{I}$, of dimension $(m \times \min(m,n))$.
- S is a diagonal matrix of dimension $(\min(m,n) \times \min(m,n))$ with non-negative entries $S_{aa} := \sqrt{\lambda_a} \geq 0$ that are called singular values. The number of non-zero values $\sqrt{\lambda_a} > 0$ of M is the rank r of M.
- $V^\dagger$ is of dimension $(\min(m,n) \times n)$ with V unitary, $V^\dagger V = \mathbb{I}$.

Schmidt decomposition The Schmidt decomposition is a concept from quantum information theory. The Schmidt decomposition can be derived by using the singular value decomposition. Consider a one-dimensional system divided into two connected subsystems A and B. We derive the Schmidt decomposition of any state $|\Psi\rangle$ on the entire system AB. A general quantum state on AB can be written as

$$|\Psi\rangle = \sum_{i,j} \Psi_{i,j} |i\rangle_A |j\rangle_B, \tag{2.24}$$

where $\{|i\rangle_A\}$ is an orthonormal basis of A with dimension m and $\{|j\rangle_B\}$ is an orthonormal basis of B with dimension n and the coefficients $\Psi_{i,j}$ may be interpreted as entries of a matrix Ψ. Carrying out a singular value decomposition on the matrix Ψ gives

$$|\Psi\rangle = \sum_{i,j} \sum_{a=1}^{\min(m,n)} U_{i,a} S_{a,a} V^*_{j,a} |i\rangle_A |j\rangle_B \tag{2.25}$$

$$= \sum_{a=1}^{\min(m,n)} S_{a,a} \left(\sum_i U_{i,a} |i\rangle_A \right) \left(\sum_j V^*_{j,a} |j\rangle_B \right) \tag{2.26}$$

$$= \sum_{a=1}^{r} \sqrt{\lambda_a} |a\rangle_A |a\rangle_B, \tag{2.27}$$

where we restrict the sum to run only over the non-zero singular values $\sqrt{\lambda_a} > 0$ such that the upper bound is given by the rank $r \leq \min(m,n)$ of S. The sets $\{|a\rangle_A\}$ and $\{|a\rangle_B\}$ are orthonormal on A and B respectively due to the properties of U and V. The basic idea is to now employ the state $|\tilde{\Psi}\rangle = \sum_{a=1}^{D} \sqrt{\lambda_a} |a\rangle_A |a\rangle_B$ of fixed Schmidt rank $D < r$ which best approximates $|\Psi\rangle$ by minimizing the norm

$$\| |\Psi\rangle - |\tilde{\Psi}\rangle \|^2 = \langle \Psi | \Psi \rangle + \langle \tilde{\Psi} | \tilde{\Psi} \rangle - \langle \Psi | \tilde{\Psi} \rangle - \langle \tilde{\Psi} | \Psi \rangle = 1 - \sum_{a=1}^{D} \lambda_a. \tag{2.28}$$

We order $\lambda_1 \geq \lambda_2 \geq ...$ such that this is a good approximation if λ_a decay quickly for increasing a. Note that the above is exact for $D \geq r$.

Construction and compression of matrix product states Any quantum state on a lattice with L sites and local dimension d on each site j can be written as

$$|\Psi\rangle = \sum_{\sigma_1,...,\sigma_L} c_{\sigma_1,...,\sigma_L} |\sigma_1, ..., \sigma_L\rangle, \tag{2.29}$$

where $\{|\sigma_j\rangle\}$ is the local basis and $|\vec{\sigma}\rangle = |\sigma_1, ..., \sigma_L\rangle = |\sigma_1\rangle \otimes ... \otimes |\sigma_L\rangle$ is the tensor product. The coefficients $c_{\sigma_1,...,\sigma_L}$ may be interpreted as entries of a vector $\vec{c}$ that has d^L components.
The singular value decomposition enables us to find a more convenient notation of $|\Psi\rangle$, the so-called matrix product state. Quite generally, the matrix product state notation of $|\Psi\rangle$ is given by

$$|\Psi\rangle = \sum_{\sigma_1,...,\sigma_L} M^{\sigma_1} M^{\sigma_2} ... M^{\sigma_L} |\sigma_1, ..., \sigma_L\rangle, \tag{2.30}$$

where M^{σ_1} is a collection of row vectors, M^{σ_L} is a collection of column vectors and all other M^{σ_j} are collection of matrices. The matrix product results in a scalar due to the vectorial nature of the first and the last matrices. So far, no assumption about the normalization has been made.
Assuming hat $|\Psi\rangle$ is normalized, we can construct a matrix product state by repeatedly applying the singular value decomposition from the left or from the right resulting in a so-called left-canonical or right-canonical matrix product state. We exemplify this for a left-canonical matrix product state. We reshape the d^L components $c_{\sigma_1,...,\sigma_L}$ of

the state vector $\vec{c}$ into a matrix $\Psi_{\sigma_1,(\sigma_2...\sigma_L)}$ of dimension $(d \times d^{L-1})$ and carry out the singular value decomposition of this matrix,

$$\Psi_{\sigma_1,(\sigma_2...\sigma_L)} = \sum_{a_1=1}^{r_1} U_{\sigma_1,a_1} S_{a_1,a_1} (V^\dagger)_{a_1,(\sigma_2...\sigma_L)}, \tag{2.31}$$

where $r_1 = \min(d, d^{L-1})$. We reshape the product $S_{a_1,a_1}(V^\dagger)_{a_1,(\sigma_2...\sigma_L)}$ back into a vector $c_{a_1,\sigma_2,...,\sigma_L}$ and then again into a matrix $c_{a_1,\sigma_2,...,\sigma_L} = \Psi_{(a_1\sigma_2),(\sigma_3...\sigma_L)}$ of dimension $(r_1 d \times d^{L-1})$. We also reshape the matrix U into a collection of row vectors A^{σ_1} with entries $A^{\sigma_1}_{a_1} = U_{\sigma_1,a_1}$. This gives

$$c_{\sigma_1,...,\sigma_L} = \sum_{a_1=1}^{r_1} A^{\sigma_1}_{a_1} \Psi_{(a_1\sigma_2),(\sigma_3...\sigma_L)}. \tag{2.32}$$

We successively apply the singular value decomposition and reshape,

$$... = \sum_{a_1=1}^{r_1} \sum_{a_2=1}^{r_2} A^{\sigma_1}_{a_1} U_{(a_1\sigma_2),a_2} S_{a_2,a_2} (V^\dagger)_{a_2,(\sigma_3...\sigma_L)} \tag{2.33}$$

$$= \sum_{a_1=1}^{r_1} \sum_{a_2=1}^{r_2} A^{\sigma_1}_{a_1} A^{\sigma_2}_{a_1,a_2} \Psi_{(a_2\sigma_3),(\sigma_4...\sigma_L)} \tag{2.34}$$

$$= ... \tag{2.35}$$

$$= \sum_{a_1...a_{L-1}} A^{\sigma_1}_{a_1} A^{\sigma_2}_{a_1,a_2} A^{\sigma_3}_{a_2,a_3} ... A^{\sigma_{L-1}}_{a_{L-2},a_{L-1}} A^{\sigma_L}_{a_{L-1}} \tag{2.36}$$

$$= A^{\sigma_1} A^{\sigma_2} ... A^{\sigma_L}, \tag{2.37}$$

where A^{σ_1} is a collection of row vectors, A^{σ_L} is a collection of column vectors and all other A^{σ_j} are collection of matrices with entries $A^{\sigma_j}_{a_{j-1},a_j} = U_{(a_{j-1}\sigma_j),a_j}$ and of dimension (r_{j-1}, r_j). The maximum dimensions of the A-matrices going from the first to the last site are $(1 \times d), (d \times d^2), ..., (d^{L/2-1} \times d^{L/2}), (d^{L/2} \times d^{L/2-1}), ..., (d \times 1)$. The maximum dimension is reached if in each singular value decomposition, the number of non-zero singular values is equal to the upper bound given by the smaller of the dimensions of the matrix to be decomposed.
Finally, the quantum state reads

$$|\Psi\rangle = \sum_{\vec{\sigma}} A^{\sigma_1} A^{\sigma_2} ... A^{\sigma_L} |\vec{\sigma}\rangle, \tag{2.38}$$

with

$$\sum_{\sigma_j} A^{\sigma_j \dagger} A^{\sigma_j} = \mathbb{I}, \tag{2.39}$$

which defines the left-canonical matrix product state. Analogously we can start reshaping from the right

$$c_{\sigma_1,...,\sigma_L} = \Psi_{(\sigma_1...\sigma_{L-1}),\sigma_L} = \sum_{a_{L-1}} U_{(\sigma_1...\sigma_{L-1}),a_{L-1}} S_{a_{L-1},a_{L-1}} (V^\dagger)_{a_{L-1},\sigma_L} \tag{2.40}$$

$$= \sum_{a_{L-1}} \Psi_{(\sigma_1...\sigma_{L-2}),(\sigma_{L-1}a_{L-1})} B^{\sigma_L}_{a_{L-1}} = ... = \tag{2.41}$$

$$= \sum_{a_1,...,a_{L-1}} B^{\sigma_1}_{a_1} B^{\sigma_2}_{a_1,a_2} ... B^{\sigma_{L-1}}_{a_{L-2},a_{L-1}} B^{\sigma_L}_{a_{L-1}}, \tag{2.42}$$

where $B^{\sigma_L}_{a_{L-1}}$ is a collection of column vectors obtained from reshaping $(V^\dagger)_{a_{L-1},\sigma_L}$, $B^{\sigma_1}_{a_1}$ is a collection of row vectors and all other $B^{\sigma_j}_{a_{j-1},a_j}$ are collections of d matrices. It follows

$$|\Psi\rangle = \sum_{\vec{\sigma}} B^{\sigma_1} B^{\sigma_2} ... B^{\sigma_L} |\vec{\sigma}\rangle, \tag{2.43}$$

with

$$\sum_{\sigma_j} B^{\sigma_j} B^{\sigma_j \dagger} = \mathbb{I}, \tag{2.44}$$

which defines the right-canonical matrix product state. We can also mix the decomposition from the left and from the right resulting in a mixed canonical matrix product state

$$c_{\sigma_1,...,\sigma_L} = A^{\sigma_1} ... A^{\sigma_l} S B^{\sigma_{l+1}} ... B^{\sigma_L}, \tag{2.45}$$

where all A matrices up to site l are left-normalized and all B-matrices starting from site $l+1$ are right-normalized. The matrix S has the components $S_{a_l,a_l} = \sqrt{\lambda_{a_l}}$ and contains the singular values on the link $(l, l+1)$. This is equivalent to the Schmidt-decomposition of a system of length L decomposed into subsystem A running from site 1 to l and subsystem B running from site $l+1$ to L. The mixed canonical state becomes

$$|\Psi\rangle = \sum_{a_l} \sqrt{\lambda_{a_l}} |a_l\rangle_A \otimes |a_l\rangle_B, \tag{2.46}$$

where

$$|a_l\rangle_A = \sum_{\sigma_1..\sigma_l} (A^{\sigma_1} ... A^{\sigma_l})_{(1,a_l)} |\sigma_1, ..., \sigma_l\rangle, \tag{2.47}$$

$$|a_l\rangle_B = \sum_{\sigma_{l+1}...\sigma_L} (B^{\sigma_{l+1}} ... B^{\sigma_L})_{(a_l,1)} |\sigma_{l+1}, ..., \sigma_L\rangle. \tag{2.48}$$

The states $|a_l\rangle_A$ are orthonormal on A and the states $|a_l\rangle_B$ are orthonormal on B.
The matrices can in principle be exponentially large and their size has to be truncated to some D to make it numerically feasible. For exponentially decaying singular values $\sqrt{\lambda_a}$, $\lambda_1 \geq \lambda_2 \geq ...$ it is possible to cut the sum (2.46) at fixed rank D which best approximates $|\Psi\rangle$ as explained above when minimizing the norm (2.28). The truncation simply keeps the first D columns of A^{σ_l}, the first D rows of $B^{\sigma_{l+1}}$ and the first D rows and columns of S. The error accumulated at each truncation is given by (2.28). However, this does not take into account the error due to minimization.
The matrix product state representation together with the approximation by truncation can be used to iteratively and variationally determine the ground state of a Hamiltonian or to determine the time evolution of the system. No details of the ground state search are discussed here. We will in the following focus on how to determine the time evolution of a system.

Matrix product operators Analogously to matrix product states we can construct matrix product operators that act onto matrix product states,

$$\hat{O} = \sum_{\sigma_1...\sigma_L \sigma'_1...\sigma'_L} c_{(\sigma_1...\sigma_L),(\sigma'_1...\sigma'_L)} |\vec{\sigma}\rangle\langle\vec{\sigma}'| \tag{2.49}$$

$$= \sum_{\vec{\sigma},\vec{\sigma}'} W^{\sigma_1,\sigma'_1} ... W^{\sigma_L,\sigma'_L} |\vec{\sigma}\rangle\langle\vec{\sigma}'|, \tag{2.50}$$

where $W^{\sigma,\sigma'}$ are matrices just like the M^{σ} but have two physical indices for outgoing and ingoing states. They are indexed $W^{\sigma_1,\sigma_1'}_{b_1}$, $W^{\sigma_L,\sigma_L'}_{b_L}$ and $W^{\sigma_j,\sigma_j'}_{b_{j-1},b_j}$ for $j \neq 1, L$. A matrix product operator acts onto a matrix product state as follows

$$\hat{O}|\Psi\rangle = \sum_{\vec{\sigma},\vec{\sigma}'} W^{\sigma_1,\sigma_1'}...W^{\sigma_L,\sigma_L'}|\vec{\sigma}\rangle\langle\vec{\sigma}'| \left(\sum_{\vec{\sigma}''} M^{\sigma_1''}...M^{\sigma_L''}|\vec{\sigma}''\rangle\right) \tag{2.51}$$

$$= \sum_{\vec{\sigma},\vec{\sigma}'} W^{\sigma_1,\sigma_1'}...W^{\sigma_L,\sigma_L'}M^{\sigma_1'}...M^{\sigma_L'}|\vec{\sigma}\rangle \tag{2.52}$$

$$= \sum_{\vec{\sigma}} \left(\sum_{\vec{\sigma}_1'} W^{\sigma_1,\sigma_1'}A^{\sigma_1'}\right)\left(\sum_{\vec{\sigma}_2'} W^{\sigma_2,\sigma_2'}M^{\sigma_2'}\right)...|\vec{\sigma}\rangle \tag{2.53}$$

$$= \sum_{\vec{\sigma}} N^{\sigma_1}N^{\sigma_2}...N^{\sigma_L}|\vec{\sigma}\rangle, \tag{2.54}$$

where $N^{\sigma_j}_{(b_{j-1},a_{j-1}'),(b_j,a_j')} = \sum_{\sigma_j'} W^{\sigma_j,\sigma_j'}_{b_{j-1},b_j} M^{\sigma_j'}_{a_{j-1}',a_j'}$ is a matrix such that the resulting state is also a matrix product state but of grown dimension.

Time evolution We apply the time-evolution operator $\exp(-i\hat{H}t)$ in order to determine the time evolution of a state $|\Psi(t)\rangle$. If $\hat{H}$ is a Hamiltonian consisting of L sites and only nearest-neighbor interactions it can be written as

$$\hat{H} = \sum_j \hat{h}_j = \hat{H}_{\text{odd}} + \hat{H}_{\text{even}}, \tag{2.55}$$

where $\hat{h}_j$ contains the interaction between sites j and $j+1$. Bond Hamiltonians $\hat{h}_j$ do not commute in general $[\hat{h}_j, \hat{h}_{j+1}] \neq 0$. We group odd bonds $\hat{H}_{\text{odd}} = \sum_{j\text{odd}} \hat{h}_j$ and even bonds $\hat{H}_{\text{even}} = \sum_{j\text{even}} \hat{h}_j$ where odd bond Hamiltonians $\hat{h}_{j,\text{odd}}$ commute amongst each other and even bond Hamiltonians $\hat{h}_{j,\text{even}}$ likewise. We discretize time $t = N\tau$ with $N \to \infty$ and $\tau \to 0$ and apply the second order Trotter decomposition given by

$$e^{-i\hat{H}t} = e^{-i\hat{H}_{\text{odd}}\frac{\tau}{2}}e^{-i\hat{H}_{\text{even}}\tau}e^{-i\hat{H}_{\text{odd}}\frac{\tau}{2}} + (\tau^3). \tag{2.56}$$

The exponentials factorize into $\exp(-i\hat{H}_{\text{odd}}\tau/2) = \prod_{j,\text{odd}} \exp(-i\hat{h}_j\tau/2)$ and $\exp(-i\hat{H}_{\text{even}}\tau) = \prod_{j,\text{even}} \exp(-i\hat{h}_j\tau)$ (first order Trotter decomposition) such that each factor $\exp(-i\hat{h}_{j,\text{odd}}\tau/2)$ acts onto a single odd bond and each factor $\exp(-i\hat{h}_{j,\text{even}}\tau)$ acts onto a single even bond. As matrix product operators they can successively be applied to the matrix product state $|\Psi\rangle$. Each application gives a matrix product state of grown dimension which is truncated before the next time-evolution operator is applied. The error of the Trotter decomposition of nth order is given by τ^{n+1} such that the error of the above second-order decomposition after $N = t/\tau$ timesteps is given by $\tau^2 t$. It scales linearly with time.

Chapter 3.

Modulation spectroscopy of ultracold bosons in optical lattices

In this chapter we want to find out more about possible excitations in the bosonic Mott-insulator. We study possible excitations by periodically driving the system by a superlattice modulation which injects momentum π into the system as explained in Section 1.3. We consider the one-dimensional single-band Bose-Hubbard Hamiltonian that is now explicitly time-dependent, given by (1.2) and (1.20),

$$H = \sum_j \left\{ -J_j(t)(a_j^\dagger a_{j+1} + \text{h.c.}) + \frac{U}{2}(n_j - \bar{n})^2 \right\}, \tag{3.1}$$

where a_j and $a_j^\dagger$ represent the bosonic annihilation and creation operators at site j and $n_j = a_j^\dagger a_j$ is the local particle number operator and the time-dependent hopping $J_j(t) = -\left(J + h\sin(\omega t)(-1)^j\right)$ is a modulation around the equilibrium value at time zero, $J(t=0) = J$, with small amplitude h. The on-site interaction strength is given by U. Note the change in notation $n_j(n_j - 1) \to (n_j - \bar{n})^2$ in comparison to (1.2). This just corresponds to a shift in energy. We work at fixed integer filling $\bar{n}$ deep in the Mott insulating regime.
The observable we choose is the energy absorbed by the system which gives insight into possible excitations. We start by employing a perturbative approach in small J/U which corresponds to the strong coupling limit of the equilibrium Bose-Hubbard model. We study the influence of the perturbation onto the corresponding low-lying excitations, i.e. particle-hole excitations of energy U. We compute the energy absorption rate averaged over one period of the perturbation and normalized by the number of lattice site in linear response theory $(1/L) \cdot \overline{dE(t)}/dt$. We complement this by a numerical study of the time evolution. We compute the energy absorbed by a single lattice site j as a function of the duration t of the perturbation, $E_j(t)$, employing the adaptive time-dependent density matrix renormalization group method in Section 3.2 and relate this to the energy absorption rate.

3.1. An analytical approach: perturbative treatment in small J/U

We aim at developing an analytical expression of the energy absorption rate, expecting to find an intuitive notion of the nature of excitations in the system. We compute the energy absorption rate in linear response theory. We use the spectral representation given by Equations (2.10) and (2.15),

$$\overline{\frac{dE(t)}{dt}} = \frac{\pi}{2}\omega|h|^2 \sum_{n,m} |\langle m|O|n\rangle|^2 \delta\left(\omega + E_n - E_m\right). \tag{3.2}$$

		•					
	•	•	•	○	•	...	•
j	1			...			L
m	1	**2**	3		...		L
d	L-1	–	1	**2**	3	...	L-2

Table 3.1. – Schematic drawing of a 'doublon-hole' excitation on a lattice of length L with commensurate filling $\bar{n} = 1$. The doublon consisting of an excess particle • is created at site $m = 2$ and the hole ∘ is created at a distance $d = 2$ to the right at site $j = m + d = 4$. This corresponds to the state $|m = 2, d = 2\rangle$ defined by Equation (3.4)

In a many-body problem the difficulty lies in determining the eigenstates $|n\rangle$ and their eigenenergies E_n. In order to do so, we employ a perturbative approach in the strong coupling limit to first non-vanishing order in J/U. We decompose the Bose-Hubbard Hamiltonian (3.1) with periodic boundary conditions into $H = H_0 + V$ where the unperturbed Hamiltonian H_0 is the on-site interaction term and V is the kinetic energy term which we consider as a small perturbation. We determine the ground state and the lowest excited states employing degenerate perturbation theory [40] and investigate the effect of the perturbation $H_{\text{pert}} = h \sin(\omega t) O$, defined by Equation (1.21), onto these low-lying excitations.

The low-lying excitations in non-degenerate perturbation theory The eigenstates of the unperturbed Hamiltonian are Fock states with eigenenergies that are multiples of the on-site interaction strength U. The groundstate of H_0 is given by the Fock state

$$|0\rangle = |\bar{n}, \bar{n}, ..., \bar{n}\rangle, \tag{3.3}$$

since we work at commensurate filling and fixed particle number. The groundstate energy is given by $\langle 0|H_0|0\rangle = 0$. The excited states must also have the same particle number and may be constructed by removing bosons from one site and putting it onto a different site. The excited state of lowest energy U corresponds to the creation of one 'doublon-hole' excitation. We call the site with occupation $\bar{n} + 1$ a 'doublon' at position m and the site with occupation $\bar{n} - 1$ a 'hole' at position $m + d$ where d is the distance to the right from the doublon to the hole. A 'doublon-hole' excitation is schematically illustrated in Table 3.1. We choose the following notation

$$|m, d\rangle = \frac{1}{\sqrt{\bar{n}(\bar{n}+1)}} a_{m+d} a_m^\dagger |0\rangle, \tag{3.4}$$

with $m = 1, ..., L$ and $d = 1, ..., L - 1$. The states $|m, d\rangle$ are degenerate eigenstates of H_0 with eigenenergy $\epsilon_{m,d} = U$ as $\langle m, d|H_0|m', d'\rangle = U\delta_{m,m'}\delta_{d,d'}$. The degeneracy is $L(L - 1)$.
The second excited state of energy $2U$ consists of two doublon-hole excitations. The third excited states consist of either three doublon-hole excitations or a site of occupation $\bar{n} + 2$. We employ degenerate perturbation theory to determine the corrections to eigenenergies and eigenstates at first order in J/U. The basic concept of degenerate perturbation theory is to identify the degenerate unperturbed eigenstates and to diagonalize the perturbation in this basis which corresponds to computing the first-order energy shifts, that are given by $\Delta_n = \langle n|V|n\rangle$ for a state $|n\rangle$. Consequently, the lowest

order is given by the zero order states but first order in energy. For higher orders one can use the formulas of non-degenerate perturbation theory except that all contributions from the unperturbed states of the degenerate subspace have to be excluded [41]. Here, the ground state energy does not change as $\langle 0|V|0\rangle = 0$. But the ground state is modified in first order,

$$|\Psi_0^1\rangle = |0\rangle + \sum_{m,d} \frac{\langle m,d|V|0\rangle}{\epsilon_{m,d} - \epsilon_0} |m,d\rangle \tag{3.5}$$

$$= |0\rangle - \frac{J}{U}\sqrt{\bar{n}(\bar{n}+1)} \sum_m \left(|m,1\rangle + |m,L-1\rangle\right), \tag{3.6}$$

as $\langle m,d|V|0\rangle = -J\sqrt{\bar{n}(\bar{n}+1)}\,(\delta_{d,1} + \delta_{d,L-1})$. All other excited states do not contribute because their overlap with $V|0\rangle$ is zero.
The zero-order states $|K,k\rangle$ that diagonalize the kinetic part V of the Hamiltonian in the degenerate subspace $|m,d\rangle$ are given by

$$|K,k\rangle = \frac{\sqrt{2}}{L} \sum_{d=1}^{L-1} \sum_{m=1}^{L} e^{id\theta(K)} \sin(kd) e^{iKm} |m,d\rangle, \tag{3.7}$$

where $K = 2\pi q/L,\ q = 1,...,L,\ k = \pi p/L,\ p = 1,...,L-1$, lattice spacing $a \equiv 1$ and with $\theta(K) = (\bar{n}+1)\sin(K)/\left(\bar{n} + (\bar{n}+1)\cos(K)\right)$. As may be seen from the Fourier transform, K is the center of mass momentum of a doublon-hole pair and k is related to the relative momentum $k_{\mathrm{rel}} = 2k - K$.
The first order energy correction is given by $\langle K,k|V|K',k'\rangle$ such that the first-order eigenenergies become

$$E(K,k) = U - 2Jr(K)\cos(k)\delta_{K,K'}\delta_{k,k'}, \tag{3.8}$$

with $r(K) = \sqrt{(\bar{n}+1)^2 + \bar{n}^2 + 2\bar{n}(\bar{n}+1)\cos(K)}$. The degeneracy of the states $|m,d\rangle$ is

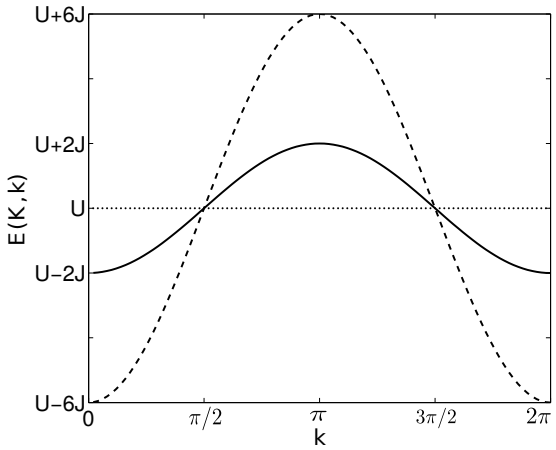

Figure 3.1. – The lowest-energy band $E(K,k)$ is centered around the on-site interaction strength U (dotted line). The dispersion is of cosine shape. We find a band width of $12J$ for $K = 0$ (dashed line) and of $4J$ for $K = \pi$ (solid line) corresponding to the possible energy range of excitations. See main text for a detailed discussion.

lifted except for a translational invariance by 2π in K-space. The energy band $E(K,k)$ for integer filling $\bar{n} = 1$ as a function of k for different center of mass momenta K

is displayed in Figure 3.1. It is centered around the on-site interaction strength U. The width depends on the value of K. The maximum width $12J$ is found for $K = 0$ corresponding to a lowest band of excitations of center of mass momentum 0. For $K = \pi$ the width is considerably reduced to $4J$ describing a lowest band of excitations with center of mass momentum π. The possible energy range of excitations thus strongly depends on the center of mass momentum K which is imposed by the perturbation as we will see in the following.
The first excited doublon-hole states are also modified resulting in a band of excited states,

$$|\Psi_1^1\rangle = |K,k\rangle - \frac{\langle 0|V|K,k\rangle}{U}|0\rangle + \sum_\alpha |\alpha\rangle, \tag{3.9}$$

$$= |K,k\rangle + \frac{J}{U}\sqrt{2\bar{n}(\bar{n}+1)}\eta_p \sin(k)|0\rangle + \sum_\alpha |\alpha\rangle, \tag{3.10}$$

where $\eta_p = (1-(-1)^p)$. We summarize all other eigenstates but $|0\rangle$ that $|K,k\rangle$ couples to via the kinetic energy V by $|\alpha\rangle$ as we do not need their explicit form in any of the following calculations.

3.1.1. Energy absorption

We now compute the energy absorption rate around $\omega \sim U$ keeping only the first perturbative term such that the following states and energies enter in equation (3.2),

$$E_0 = 0 \tag{3.11}$$

$$E_n = U - E(K,k) = U - 2Jr(K)\cos(k) \tag{3.12}$$

$$|0\rangle = |0\rangle \tag{3.13}$$

$$|n\rangle = |K,k\rangle \tag{3.14}$$

We compute the relevant matrix element,

$$\langle K,k|O|0\rangle = \frac{\sqrt{2}}{L}\sum_{d=1}^{L-1}\sum_{m=1}^{L} e^{-id\theta(K)}e^{-iKm}\sin(kd)\sum_{j=1}^{L}(-1)^j\left(\langle m,d|a_j^\dagger a_{j+1}|0\rangle + \text{h.c.}\right) \tag{3.15}$$

$$= \frac{\sqrt{2\bar{n}(\bar{n}+1)}}{L}\sum_{d,m,j} e^{-id\theta(K)}e^{-iKm}\sin(kd)(-1)^j\left(\delta_{j,m}\delta_{m+d,j+1} + \delta_{j+1,m}\delta_{m+d,j}\right) \tag{3.16}$$

$$= \frac{\sqrt{2\bar{n}(\bar{n}+1)}}{L}\sum_{d,m,j} e^{-id\theta(K)}e^{-iKm}\sin(kd)(-1)^j\left(\delta_{j,m}\delta_{d,+1} + \delta_{j,m-1}\delta_{d,L-1}\right) \tag{3.17}$$

$$= \frac{\sqrt{2\bar{n}(\bar{n}+1)}}{L}\sum_{d} e^{-id\theta(K)}\sin(kd)\left(\sum_{m=1}^{L}(-1)^m e^{-iKm}\right)\left(\delta_{d,+1} - \delta_{d,L-1}\right) \tag{3.18}$$

$$= \frac{\sqrt{2\bar{n}(\bar{n}+1)}}{L}L\delta_{K,\pi}\left(e^{-i\theta(K)}\sin(k) + e^{-i(L-1)\theta(K)}\sin(k(L-1))\right) \tag{3.19}$$

$$= \sqrt{2\bar{n}(\bar{n}+1)}\delta_{K,\pi}\Big(\sin(k) + \sin(k(L-1))\Big) \tag{3.20}$$

$$= \sqrt{2\bar{n}(\bar{n}+1)}\sin(k)\eta_p\delta_{K,\pi}, \tag{3.21}$$

where we used $\left(\sum_{m=1}^{L}(-1)^m \exp(-iKm)\right) = L\delta_{K,\pi}$, $\theta(\pi) = 0$ and $\sin(k) + \sin(k(L-1)) = \sin(k)\eta_p$. The full expression of the energy absorption rate normalized by the number of lattice sites becomes

$$\frac{1}{L}\overline{\frac{dE(t)}{dt}} = \frac{\pi}{L}\omega|h|^2\bar{n}(\bar{n}+1)\sum_{k,K}\sin^2(k)\eta_p^2\delta_{K,\pi}\delta\left(\omega - U + 2Jr(K)\cos(k)\right), \tag{3.22}$$

$$= \frac{\pi}{L}\omega|h|^2\bar{n}(\bar{n}+1)\sum_{p=1}^{L-1}\eta_p^2\sin^2\left(\frac{p\pi}{L}\right)\delta\Big(\omega - U + 2J\cos\left(\frac{p\pi}{L}\right)\Big), \tag{3.23}$$

where we used $r(\pi) = 1$. Note that we can replace the sum $\sum_{p=1}^{L-1}$ by $\sum_{p=0}^{L-1}$ as the $p = 0$-term is zero. From the formula we see that an excitation from the ground state $|0\rangle$ to the lowest-band of excited states $|K, k\rangle$ via the superlattice perturbation O is only possible for $K = \pi$. In lowest order the perturbation creates a doublon-hole pair with center of mass momentum $K = \pi$. In contrast, the relative momentum can take arbitrary values within the first Brillouin zone $(0, 2\pi]$, where 0 is excluded and 2π included. Momentum conservation of the atoms does not hold any longer due to the superlattice amplitude modulation which introduces a lattice momentum kick of π as may be seen from the Fourier transform of the perturbing operator (1.23). We have discussed the operator in Section (1.3) and find that we expect it to create particle-hole pairs with a center of mass momentum of π in accordance with the above result. To obtain the continuum limit we use

$$\frac{1}{L}\sum_{p=1}^{L}(1-(-1)^p)^2 f\left(\frac{p\pi}{L}\right) \to \frac{2}{\pi}\int_0^\pi \mathrm{d}k f(k), \tag{3.24}$$

$$\delta\left(g(k)\right) = \sum_{k_0}\frac{\delta(k-k_0)}{|g'(k_0)|}, \tag{3.25}$$

$$g(k) = \omega - U + 2J\cos(k), \tag{3.26}$$

where k_0 are the zeros of $g(k)$ within the range of integration. There is only one $k_0 = \arccos((U-\omega)/2J)$. We obtain

$$\frac{1}{L}\overline{\frac{dE(t)}{dt}} = \frac{\omega|h|^2\bar{n}(\bar{n}+1)}{J}\sqrt{1-\left(\frac{U-\omega}{2J}\right)^2}. \tag{3.27}$$

The energy absorption rate normalized by the number of lattice sites has a $\sqrt{1-((U-\omega)/2J)^2}$-dependence within $U - 2J \leq \omega \leq U + 2J$ and a maximum of the absorption peak that lies slightly to the right of U,

$$\omega_0 = U\left(1+\left(\frac{2J}{U}\right)^2\right). \tag{3.28}$$

The range of absorption $\omega \in [U-2J, U+2J]$ corresponds to the width $4J$ of the lowest energy band $E(K = \pi, k)$ (see Figure 3.1) and is a characteristic of the non-momentum conserving perturbation O. This can be seen in Figures 3.2a, 3.2c and 3.2e where we show the energy absorption rate (3.27) for interaction strengths $U/J = 20$, $U/J = 40$ and $U/J = 60$, respectively, in comparison to numerical results obtained in the following Section 3.2. In contrast, the bandwidth is maximal for $K = 0$, $E(K = 0, k) =$

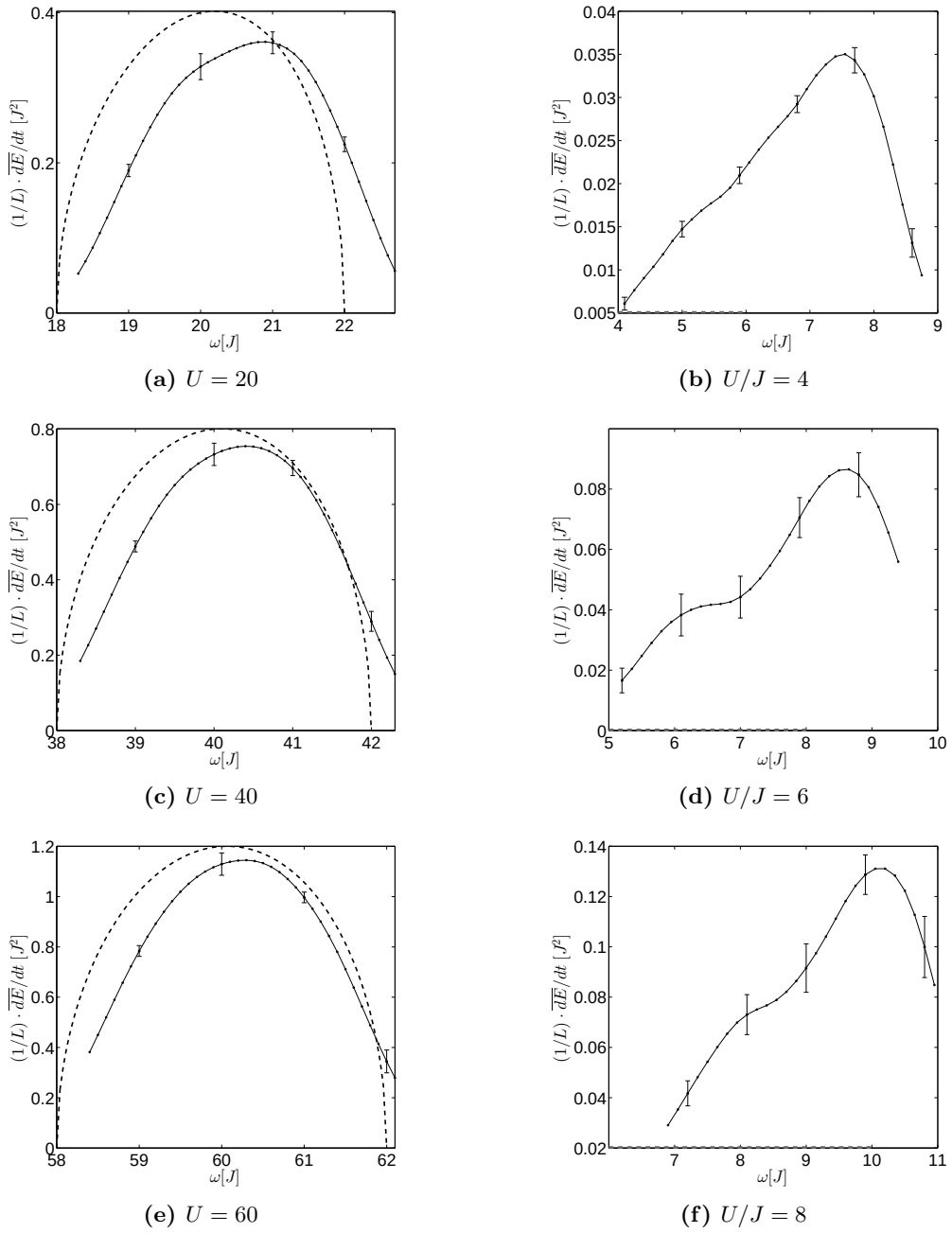

(a) $U = 20$ **(b)** $U/J = 4$

(c) $U = 40$ **(d)** $U/J = 6$

(e) $U = 60$ **(f)** $U/J = 8$

Figure 3.2. – The energy absorption rate $(1/L) \cdot \overline{dE(t)}/dt$ as a function of the perturbing frequency ω/J for $J = 1$ and different interactions U/J. In the strong coupling regime $U/J = 20, 40, 60$, displayed in (a), (c) and (e), respectively, we compare lowest-order perturbative results (dashed lines) to the numerical results (solid lines) obtained from a density-matrix renormalization group study in Section 3.2 for system length $L = 30$, Hilbert-space cut-off $D = 128$, time step of the Trotter decomposition $\Delta t = 0.01$, number of available states per site $\sigma = 3$ at the central site $j = 15$. The range of absorption is given by $\omega \in [U - 2J, U + 2J]$ with a maximum slightly to the right of U. See main text for a more detailed discussion. We also employ the density matrix renormalization group method to study the energy absorption rate at weak couplings $U/J = 8, 6, 4$, displayed in (f), (d) and (b), respectively. We choose parameters $L = 40$, $D = 128$, $\Delta t = 0.05$, $\sigma = 7$ and the central site $j = 20$. The dashed bottom lines indicate the range of absorption predicted by the perturbative approach at strong coupling. See Section 3.2.1 for a detailed discussion.

$4J(2\bar{n}+1)$. This corresponds to the range of absorption expected in lattice shaking experiments where the amplitude modulation is commensurate with the equilibrium lattice and thus momentum-conserving such that doublon-hole pairs with center of mass momentum zero are created [17].

3.2. A numerical approach: density matrix renormalization group study

We employ the adaptive time-dependent density matrix renormalization group method as introduced in Section 2.3 to determine the time evolution of the system for a finite system of length L with open boundary conditions. We use the code from [42]
The system is subjected to a periodic modulation of the lattice potential such that on average energy will be absorbed if the modulation frequency corresponds to the energy needed to create an excitation. We compute the energy on a single site j as a function of the duration t of the perturbation given by

$$E_j(t) = J(t)\langle a_j^\dagger a_{j+1} + \text{h.c.}\rangle + \frac{U}{2}\langle n_j^2\rangle - \frac{U}{2}, \tag{3.29}$$

where we used $\langle n_j\rangle = \bar{n} = 1$. We choose hopping $J = 1$ and $\hbar \equiv 1$ such that all energies are measured in units of J and time in units of $1/J$. We consider a small modulation $h = 0.1$.
We study different interaction regimes. We consider strong interactions $U/J = 60,\ 40,\ 20$ and smaller interactions $U/J = 8,\ 6,\ 4$ approaching the phase transition to the superfluid state at $(U/J)_c \sim 3.4$.
At strong interactions particle-hole excitations are formed which require an energy of the order of the on-site interaction energy U. Absorption at higher orders, at multiples of the on-site interaction U, is also expected. This would correspond to several particle-hole excitations or multiply occupied sites. However, we do not study these here. We thus expect an energy absorption at a modulation frequency $\omega \approx U$. One example of typical numerical results for the absorbed energy at strong interactions $U/J = 40$ and a perturbing resonant frequency $\omega/J = 40$ is shown in Figure 3.3 and compared to the off-resonant case $\omega/J = 38.2$. On resonance, a clear absorption of energy by the system is indeed visible which saturates at longer times. Energy absorption decreases when shifting away from resonance and overall absorption is very small for $\omega/J = 38.2$. Additionally, oscillations with a frequency corresponding to the perturbing frequency occur in both cases. However, this is not ideally displayed in Figure 3.3 because the time step chosen for saving the data is about two thirds of the oscillation period on resonance such that the oscillations corresponding to the perturbing frequency are not properly resolved.
We want to determine the energy absorption rate as a function of the modulation frequency and compare to analytical results from the preceding Section 3.1. We take the slope m in the linear regime of $E_j(t)$ as a measure for the energy absorption rate by a single site. The fit function is thus given by

$$E_j(t) = m \cdot t + c \cdot \sin(\omega t + \phi) + \text{offset}, \tag{3.30}$$

with fit parameters m, c, ϕ and offset. We identify the slope $m = (1/L)\cdot\overline{dE(t)}/dt$. The linear dependence is modulated by $c * \sin(\omega t + \phi)$ where ω is the perturbing frequency. The fitting range $t \in [t_{\min}, t_{\max}]$ (see Figure 3.3) is chosen within the linear regime of

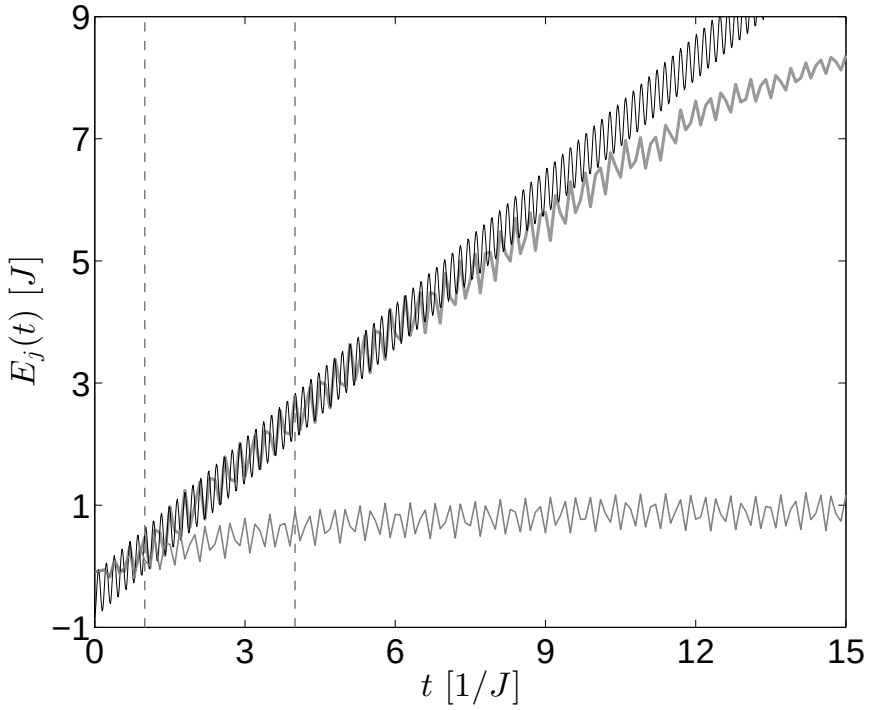

Figure 3.3. – The energy $E_j(t)$ at site $j = L/2$ as a function of the duration of the perturbation t for the following parameters: hopping $J = 1$, on-site interaction $U/J = 40$, time step of the Trotter decomposition $\Delta t = 0.01$, number of available states per site $\sigma = 3$, system length $L = 40$ and Hilbert-space cut-off $D = 128$. We probe the system at different frequencies around resonance $\omega \approx U$. We display two frequencies. The rising curve (solid gray line) shows the result for a perturbing frequency $\omega/J = 40$ on resonance where the range considered for the fitting procedure $t \in [1, 4]$ is indicated by vertical dashed lines. The fitted curve (black solid line) is a linear fit with an additional oscillation on top that has the frequency of the perturbation (Equation (3.30)). A clear absorption of energy by the system is visible. In contrast, the bottom curve shows the result for $\omega/J = 38.2$ which is away from resonance and little energy is absorbed. In both cases, an oscillatory behavior with the frequency corresponding to the modulation frequency occurs. However, this is not distinctively visible in this plot due to the relatively large time step chosen for saving the data.

$E_j(t)$ and such that $E_j(t)$ has numerically converged (see below) and boundary effects do not effect the bulk behavior within this time. See below for a detailed discussion of the convergence and boundary effects.

Numerical convergence We have shown results for central sites as we find that boundary effects are strong. We attribute this to the fact that excitations carry an extra momentum kick of π introduced by the dimerized modulation as explained in Section 1.3 such that scattering from the boundaries significantly contributes already at short times. We consider different system lengths in order to determine what minimum system length is needed to be able to clearly separate bulk behavior from boundary effects. For $L = 20$ boundary effects are strong such that no bulk region can be identified. However, for system lengths $L = 30$ or $L = 40$ we find good agreement of $E_j(t)$ on the central sites up to sufficiently large times such that we can study $E_j(t)$ for a single central site to understand the physics in the bulk.
For each interaction strength U/J and system length L we ensure that the observable $E_j(t)$ numerically converges within a certain total time. Note that the time range considered for fitting must be equal or smaller. By convergence we mean that the relative error on $E_j(t)$ is sufficiently small on variation of one of the parameters Hilbert-space cut-off D, time step Δt of the Trotter decomposition and number of available states per site σ, for different modulation frequencies across the range of absorption while all other parameters are kept fixed. We define the relative error on variation of one of the preceding parameters $param$, $e_{\mathrm{rel}}^{param}(t)$ (Equation (A.1) in Appendix A), and carry out a detailed error analysis for the cases $U/J = 20$ and $U/J = 4$ in Appendix A. We deduce suitable parameter values for our analysis. We also compute the relative error when varying the system length L and the site j to a neighboring one that is likewise odd or even in order to verify that we can separate bulk properties from boundary effects. As an example we give the relative errors for one particular case at strong coupling $U/J = 20$, $L = 30$ at site $j = 15$ at a frequency $\omega = 19$ at the upper bound of the fitting range $t_{\max}$. We choose a fitting range of $t = [1, t_{\max} = 4]$ and find that $E_j(t)$ converges satisfactorily for parameters $\Delta t = 0.01$, $D = 128$ and $\sigma = 3$. We vary one parameter while keeping all others fixed at the preceding values. When varying Δt between $\Delta t_a = 0.01$ and $\Delta t_b = 0.005$ we find $e_{\mathrm{rel}}^{\Delta t}(t_{\max}) = 0.01$. When varying D between $D_a = 128$ and $D_b = 196$ we find $e_{\mathrm{rel}}^{D}(t_{\max}) = 3.0 \cdot 10^{-5}$. When varying σ between $\sigma_a = 3$ and $\sigma_b = 5$ we find $e_{\mathrm{rel}}^{\sigma}(t_{\max}) = 0.04$. When varying L between $L_a = 30$ and $L_b = 50$ ($j = 25$) we find $e_{\mathrm{rel}}^{L}(t_{\max}) = 7.5 \cdot 10^{-3}$. Finally, when varying j between $j_a = 15$ and $j_b = 13$ we find $e_{\mathrm{rel}}^{j}(t_{\max}) = 0.02$. We conclude that for parameters $\Delta t = 0.01$, $D = 128$ and $\sigma = 3$, $E_j(t)$ converges satisfactorily up to times $t_{\max} = 4$. Additionally, we can separate bulk properties from boundary effects for $L = 30$ at the central site $j = 15$.

3.2.1. Energy absorption

The energy absorption rate as a function of modulation frequency is determined by fitting (3.30) for each interaction strength U/J at different frequencies ω around resonance. We choose a suitable time range considered for fitting in accordance with an observation of linear behavior, bulk behavior and numerical convergence of $E_j(t)$ (see above) within this time range. For instance, we choose fitting ranges $t \in [1, 4]$ for $U/J = 20$ and $t \in [1, 6]$ for $U/J = 4$.
The energy absorption rate is shown in Figure 3.2 for strong interactions $U/J =$

$20, 40, 60$ and for weak interactions $U/J = 8, 6, 4$ approaching the phase transition.
Let us discuss the results at strong coupling first which are shown in Figures 3.2a, 3.2c and 3.2e for $U/J = 20$, $U/J = 40$ and $U/J = 60$, respectively, in comparison to the analytical results from the preceding Section 3.1. We observe a peak roughly centered around the resonance frequency $\omega \approx U$. The maximum of the peak is slightly shifted above $\omega \approx U$ and this shift increases for decreasing interactions which is in agreement with the perturbative result for the maximum at $\omega_0 = U\left(1 + (2J/U)^2\right)$ (Equation (3.28)). We do not observe a sharp peak at $\omega = U$ because the lowest band of excitations has a certain width due to corrections in J which is given by $4J$ in the perturbative approach. At $U/J = 60$ we find good qualitative accordance with the perturbative result in both, shape and width of the peak, as shown in Figure 3.2e. We find deviations in the overall amplitude and the shape of the wings. The numerical results display a rather linear-like decay in the wings in contrast to a square root-like decay in the analytical results. For decreasing interaction ($U/J = 40,\ 20$), the numerical absorption peak shifts farther to the right as may be seen in Figure 3.2c and 3.2a. We attribute this to the fact that higher-order corrections will shift the center of the lowest energy band of excitations away from U. We also compute further corrections in first-order by considering first-order states as well as first-order energies. However, the additional first-order contributions vanish such that the deviations must stem from higher order corrections in J/U whose study remains of interest for future works in order to understand further corrections. Nevertheless, the qualitative agreement is sufficiently good and we conclude, that the interpretation in terms of the creation of doublon-hole pairs of center of mass momentum π from the perturbative approach in Section 3.1 constitutes a reasonable interpretation of the nature of excitations at strong interactions. In optical lattice experiments, the position of the spectral response due to lattice shaking is sometimes used to calibrate the lattice depth [21], i.e. to determine the on-site interaction strength U. As the width here, $4J$, is much smaller than the width of $12J$ in standard lattice shaking experiments [17] as discussed in Section 3.1.1, our setup can be used for a better calibration and is attractive for experimentalists as the implementation remains simple.
Let's now turn the discussion to the results at weak coupling shown in Figures 3.2f, 3.2d and 3.2b for interaction strengths $U/J = 8$, $U/J = 6$ and $U/J = 4$, respectively. We observe a broadening in the frequency range compared to the response at strong interactions. The maximum is shifted farther away from resonance and the left flank is flattened. This may be seen in Figures 3.2f, 3.2d and 3.2b for interaction strengths $U/J = 8$, $U/J = 6$ and $U/J = 4$ respectively. Note, that the frequency range probed is limited by our fitting procedure. At small perturbing frequencies we have to cut at frequencies $\omega/J = 6.9$, $\omega/J = 5.2$ and $\omega/J = 4.1$ for $U/J = 8, 6, 4$ respectively because the amplitude of the oscillations with the perturbing frequency ω become of the order of the overall rise in energy such that no linear slope can be reliably fit as may be seen in Figure 3.3. At large perturbing frequencies we have to cut at frequencies $\omega/J = 10.95$, $\omega/J = 9.4$ and $\omega/J = 8.75$ respectively. Compared to the analytical strong coupling result which predicts absorption within $\omega \in [U-2J, U+2J]$, the range is not only slightly broadened at weak coupling but also shifted to higher frequencies. In Figures 3.2f, 3.2d and 3.2b we indicate the absorption range up to the maximal frequency predicted by the perturbative approach $\omega_{\max} = U + 2J$ by horizontal dashed lines at the bottom. For $U/J = 8$ the range is shifted to the right by about $\Delta(\omega/J) \approx 1$. For decreasing interactions this shift increases such that at $U/J = 4$ we do not observe absorption below $\omega = U$ but the entire range of absorption lies shifted to the right of $\omega = U$

up to $\omega \approx U + 5J$. This somewhat corresponds to the expectation for the superfluid case. In the non-interacting limit $U = 0$, all particles occupy the zero momentum state and we expect excitations with energy $4J$, corresponding to the band width, given the constraint $\Delta k = \pi$. For increasing interactions more momenta get occupied such that the range of absorption smears out between zero and $4J$ which somewhat corresponds to the response we observe here, however the peak is shifted by the finite on-site interaction strength $U/J = 4$. Nevertheless, this interpretation has to be regarded with caution as we are above the superfluid to Mott-insulator transition where this picture is not valid. For interactions $U/J = 8$ and $U/J = 6$, the left flank is not only flattened but we observe a dip appearing slightly above $\omega = U/J$. We suspect these to be numerical artifacts because errors are large in this region and the dip disappears at $U/J = 4$ where errors are smaller. This may be investigated by repeating the analysis for different input parameters such that we obtain an energy $E_j(t)$ that is numerically stable up to longer times such that we can increase the range of fitting and thus reduce errors (see error analysis below). However, as the discussed results are quite recent this goes beyond the time frame of this work. Nevertheless, further studies in order to understand the nature of excitations at weak interactions remain of interest for our future works.

Error analysis An error analysis of the energy absorption rate determined numerically by fitting the slope $m = (1/L) \cdot \overline{dE(t)}/dt$ of (3.30) is not straightforward as different sources are contributing. First of all, there is a fitting error returned by *Matlab* which we use for our analysis. Secondly, we have a freedom of choice in the fitting range $t \in [t_{\min}, t_{\max}]$. Finally, the errors on the choice of numerical parameters (discussed above and in Appendix A) will lead to an error on m. We define the following three errors

- *Matlab* returns the 95% confidence bounds on m, the lower bound m_{low} and the upper bound m_{up}, that allow a deviation of 5% on m. The confidence bounds are calculated using the mean squared error and the Jacobian of the fitted values with respect to the coefficients [43]. We define the fit error $\Delta_{\text{fit}} = (\text{abs}(m - m_{\text{low}}) + \text{abs}(m - m_{\text{up}}))/2$.

- We vary the upper bound $t_{\max}$ of the fitting range by ± 1 and determine the corresponding slope $m_{\pm}$. We define the fitting range error $\Delta_{\text{range}} = (\text{abs}(m - m_{+}) + \text{abs}(m - m_{-}))/2$.

- We consider the largest relative error $e_{\text{rel}}^{param}(t_{\max})$ from the variation of parameters and determine the corresponding slope $\tilde{m}$ when varying this parameters. We define the resulting error on m as $\Delta_{\text{num}} = \text{abs}(m - \tilde{m})$.

This error analysis has to be carried out for each interaction strength U/J and each value of ω separately. We present error bars in Figure 3.2. Each error bar displays the largest of the three above errors. We exemplify this for the case $U/J = 20$. We find that the leading relative errors stem from the variation of σ or the variation of j (see Appendix A) depending on the value of ω. The resulting error Δ_{num} on m is of same order of magnitude as the errors Δ_{fit} and as Δ_{range} and we cannot determine one leading error. See Appendix A for a more detailed discussion. For increasing interactions Δ_{range} increases such that it is the dominating error for $U/J = 60$. At weak interactions, Δ_{fit} is the dominating error but Δ_{num} is of the same order of magnitude whereas Δ_{range} is one order of magnitude smaller. For $U/J = 6$ and $U/J = 8$ the error bars are larger

compared to $U/J = 4$ because we had to choose a shorter fitting range that only covers few oscillation periods and thus leads to a larger fitting error.

Chapter 4.

Thermometry of fermions in optical lattices by modulation spectroscopy

As motivated in the Introduction one of the key obstacles in fermionic lattice experiments is the lack of reliable methods to adequately measure the temperature of a Fermi gas confined to an optical lattice.
The situation is much better in the weakly interacting regime for harmonically trapped gases in the absence of an additional lattice potential. The temperature can directly be determined by a time-of-flight measurement. The integrated density profile of the cloud is imaged after suddenly turning off the potential and letting the gas expand. For sufficiently long expansion times, the measured density profile is equivalent to the momentum distribution in the trap and can be fit to certain functions to determine the temperature [44]. This gets more complicated for increasing interactions since expansion is no longer ballistic. Luckily, temperature can often still be determined from the 'tail' of the distribution. However, this fails at very low temperatures. In particular, in the presence of a lattice there is no controlled theory to connect observables to temperature. Different schemes have been suggested and experimentally tested. In the case of bosonic atoms, direct thermometry is possible by matching experimental time-of-flight images to theoretical quantum Monte Carlo simulations taking into account finite expansion time and finite imaging resolution [12]. However, this is computationally expensive and not possible in the fermionic case. For fermionic atoms, one usually determines the temperature in the lattice from measuring the temperature before switching the lattice on and after switching it off [9]. Adiabadicity during the loading process is assumed which means that the temperature changes when ramping the lattice but the entropy stays constant. The temperature after loading is then determined from the initial entropy. However, this is limited due to non-adiabatic heating processes such as light scattering and fails for in-lattice cooling. One possible approach to directly measure the temperature in fermionic experiments is by measuring the double occupancy in the lattice which is very sensitive to thermal fluctuations and may be connected to theoretical calculations [45]. But this is limited to temperatures that are large enough to significantly affect the double occupancy. For an overview over different possible schemes see Reference [46]. All these proposals have their limitations and most methods cannot be extended into the low temperature regime of interest.
Here, we present a scheme to directly measure the temperature of a Fermi gas trapped in an optical lattice by periodically driving the lattice as introduced in Section 1.3. Our scheme constitutes a promising alternative to other proposals. The experimental setup is particularly simple and it does not require the input of theoretical modeling. Furthermore, this scheme extends to very low temperatures below the Néel temperature where antiferromagnetic ordering sets in and which are still far from being met in experiment.

4.1. Non-interacting tight-binding fermions subjected to a periodic perturbation

The homogeneous system in one dimension The single-band tight-binding Hamiltonian for non-interacting fermions in an optical lattice in one dimension is given by Equation (1.15),

$$H_0 = -J\sum_{j,\sigma}(c^\dagger_{j,\sigma}c_{j+1,\sigma} + \text{h.c.}) - \mu\sum_{j,\sigma} n_{j,\sigma}. \tag{4.1}$$

The Hamiltonian is diagonalized by the Fourier transform

$$c_{j\sigma} = \frac{1}{\sqrt{L}}\sum_k e^{ikaj}c_{k,\sigma}, \tag{4.2}$$

where a is the lattice spacing and L is the number of lattice sites. We obtain

$$H_0 = \sum_{k,\sigma}(\epsilon_k - \mu)c^\dagger_{k,\sigma}c_{k,\sigma}, \tag{4.3}$$

with the dispersion given by

$$\epsilon_k = -2J\cos(ka). \tag{4.4}$$

The lattice momentum k is discretized $k = 2\pi m/(La)$ with $m = -L/2+1, ..., L/2$ such that there is L k-values within the first Brillouin zone $(-\pi/a, \pi/a]$. The notation used is such that $-\pi/a \notin (-\pi/a, \pi/a]$ and $\pi/a \in (-\pi/a, \pi/a]$. There is $2L$ available single-particle states since each lattice sites can be occupied with two particles of different spin $\sigma = \uparrow, \downarrow$.
We subject the above equilibrium system to a periodic superlattice modulation as introduced in Section 1.3 given by Equation (2.1), $H_{\text{pert}} = h\sin(\omega t)O$, which injects momentum π into the system . The Fourier transform of the perturbing operator given by Equation (1.22) gives

$$O = \sum_{k,\sigma}\left(e^{i(k+\pi)}c^\dagger_{k,\sigma}c_{k+\pi,\sigma} + \text{h.c.}\right), \tag{4.5}$$

where we set $a \equiv 1$. It is apparent that particles of same spin are transferred from a state of momentum k to a state of momentum $k+\pi$ as discussed in Section 1.3. This transfer is only possible if the state (k, σ) is initially occupied and the state $(k+\pi, \sigma)$ is initially unoccupied. Hence, the response of the system to the perturbation will strongly depend on the filling of the system.

4.1.1. Exact time dependence of the quasimomentum distribution

We want to compute the exact time-dependence of the occupation of a state of quasimomentum k,

$$\langle n_k(t)\rangle = \langle c^\dagger_k(t)c_k(t)\rangle. \tag{4.6}$$

The time evolution of the fermionic operators is given by Heisenberg's equation of motion,

$$-i\hbar\frac{d}{dt}c_k(t) = [H, c_k(t)], \tag{4.7}$$

where $H = H_0 + h\sin(\omega t)O$ is given by Equations (4.3) and (4.5) with $\mu = 0$ as the particle number is fixed during time evolution. We neglect the spin σ for now. As H only couples states of momentum k and $k+\pi$ we obtain two coupled equations that can be written in the following form

$$i\hbar\frac{d}{dt}\vec{c}(t) = M\vec{c}(t), \tag{4.8}$$

with $\vec{c}(t) = (c_k(t), c_{k+\pi}(t))^T$ and

$$M = \begin{pmatrix} \epsilon_k & 2ih\sin(\omega t)\sin(k) \\ -2ih\sin(\omega t)\sin(k) & \epsilon_{k+\pi} \end{pmatrix}. \tag{4.9}$$

Effectively, we are dealing with a driven two-state system. The standard procedure to solve such a two-level system is a transformation of operators $\tilde{\vec{c}}(t) = U\vec{c}(t)$ [35],

$$U = \begin{pmatrix} \exp(i\omega/2t) & 0 \\ 0 & \exp(-i\omega/2t) \end{pmatrix}, \tag{4.10}$$

where U is a unitary matrix, $U^\dagger U = \mathbb{I}$. This transformation corresponds to a change of reference frame from the laboratory frame to a rotating frame with angular velocity ω. We transform the system of coupled Equations (4.8),

$$i\hbar U\dot{\vec{c}}(t) = UMU^\dagger U\vec{c}(t), \tag{4.11}$$

and obtain

$$U\dot{\vec{c}}(t) = \dot{\tilde{\vec{c}}}(t) - \frac{i\omega}{2}\sigma_z\tilde{\vec{c}}(t), \tag{4.12}$$

where $\sigma_z = \left(\begin{smallmatrix} 1 & 0 \\ 0 & -1 \end{smallmatrix}\right)$ is the Pauli-matrix, and

$$UMU^\dagger = \begin{pmatrix} \epsilon_k & hi\sin(k)(\exp(2i\omega t)+1) \\ -hi\sin(k)(\exp(-2i\omega t)+1) & -\epsilon_k \end{pmatrix}. \tag{4.13}$$

Near resonance, $\omega = \pm 2\epsilon_k$, we can neglect rapidly oscillating terms $\exp(\pm 2i\omega t)$ because they average out. This is known as the rotating-wave approximation [47]. We obtain

$$UMU^\dagger \approx \begin{pmatrix} \epsilon_k & hi\sin(k) \\ -hi\sin(k) & -\epsilon_k \end{pmatrix}, \tag{4.14}$$

which is now time-independent. Combining (4.12) and (4.14) gives

$$i\hbar\dot{\tilde{\vec{c}}}(t) = \begin{pmatrix} \epsilon_k - \frac{\hbar\omega}{2} & hi\sin(k) \\ -hi\sin(k) & -\epsilon_k + \frac{\hbar\omega}{2} \end{pmatrix}\tilde{\vec{c}}(t), \tag{4.15}$$

where the time-dependence is entirely comprised in the coefficients $\tilde{\vec{c}}(t)$. This system of equations can be solved by the simple ansatz

$$\tilde{\vec{c}}_k(t) = A\sin\left(\frac{\Omega}{2}t\right) + B\cos\left(\frac{\Omega}{2}t\right), \tag{4.16}$$

$$\tilde{\vec{c}}_{k+\pi}(t) = C\sin\left(\frac{\Omega}{2}t\right) + D\cos\left(\frac{\Omega}{2}t\right). \tag{4.17}$$

From the second derivative we obtain

$$(\hbar\Omega)^2 = 4\left(\left(\epsilon_k - \frac{\hbar\omega}{2}\right)^2 + (h\sin(k))^2\right). \tag{4.18}$$

By matching the first and second derivatives of the ansatz with the system of Equations (4.15) at time $t = 0$ we obtain

$$A = -2\frac{i}{\hbar\Omega}\left(\left(\epsilon_k - \frac{\hbar\omega}{2}\right)\tilde{c}_k(0) - h\sin(k)\tilde{c}_{k+\pi}(0)\right), \tag{4.19}$$

$$B = \tilde{c}_k(0), \tag{4.20}$$

$$C = -2\frac{i}{\hbar\Omega}\left(-h\sin(k)\tilde{c}_k(0) - \left(\epsilon_k - \frac{\hbar\omega}{2}\right)\tilde{c}_{k+\pi}(0)\right), \tag{4.21}$$

$$D = \tilde{c}_{k+\pi}(0). \tag{4.22}$$

Note that $\langle n_k(t)\rangle = \langle c_k^\dagger(t)c_k(t)\rangle = \langle \tilde{c}_k^\dagger(t)\tilde{c}_k(t)\rangle$ such that we can now compute $\langle n_k(t)\rangle$. We obtain

$$\langle n_k(t)\rangle = \left(4\frac{(\epsilon_k - \frac{\hbar\omega}{2})^2}{(\hbar\Omega)^2}\sin^2\left(\frac{\Omega}{2}t\right) + \cos^2\left(\frac{\Omega}{2}t\right)\right)\langle c_k^\dagger(0)c_k(0)\rangle \tag{4.23}$$

$$+ 4\frac{(h\tilde{t}\sin(k))^2}{(\hbar\Omega)^2}\sin^2\left(\frac{\Omega}{2}t\right)\langle c_{k+\pi}^\dagger(0)c_{k+\pi}(0)\rangle, \tag{4.24}$$

$$\langle n_{k+\pi}(t)\rangle = 4\frac{(h\tilde{t}\sin(k))^2}{(\hbar\Omega)^2}\sin^2\left(\frac{\Omega}{2}t\right)\langle c_k^\dagger(0)c_k(0)\rangle \tag{4.25}$$

$$+ \left(4\frac{(\epsilon_k - \frac{\hbar\omega}{2})^2}{(\hbar\Omega)^2}\sin^2\left(\frac{\Omega}{2}t\right) + \cos^2\left(\frac{\Omega}{2}t\right)\right)\langle c_{k+\pi}^\dagger(0)c_{k+\pi}(0)\rangle. \tag{4.26}$$

At zero temperature all single-particle levels up the Fermi level $\epsilon_F = \mu = -2t\cos(k_F a)$ are occupied, where k_F is the Fermi momentum. The ground state wave function is the Fermi sea

$$|GS\rangle = \prod_{|k|\leq k_F} c_k^\dagger|0\rangle, \tag{4.27}$$

where $|0\rangle$ is the vacuum. We denote zero temperature expectation values by $\langle\cdot\rangle_0$. They are taken with respect to the ground state such that Equation (4.23) yields

$$\langle n_k(t)\rangle_0 = \left(4\frac{(\epsilon_k - \frac{\hbar\omega}{2})^2}{(\hbar\Omega)^2}\sin^2\left(\frac{\Omega}{2}t\right) + \cos^2\left(\frac{\Omega}{2}t\right)\right)\Theta(k_F - |k|) \tag{4.28}$$

$$+ 4\frac{(h\tilde{t}\sin(k))^2}{(\hbar\Omega)^2}\sin^2\left(\frac{\Omega}{2}t\right)\Theta(k_F - |k+\pi|), \tag{4.29}$$

$$\langle n_{k+\pi}(t)\rangle_0 = 4\frac{(h\tilde{t}\sin(k))^2}{(\hbar\Omega)^2}\sin^2\left(\frac{\Omega}{2}t\right)\Theta(k_F - |k|) \tag{4.30}$$

$$+ \left(4\frac{(\epsilon_k - \frac{\hbar\omega}{2})^2}{(\hbar\Omega)^2}\sin^2\left(\frac{\Omega}{2}t\right) + \cos^2\left(\frac{\Omega}{2}t\right)\right)\Theta(k_F - |k+\pi|), \tag{4.31}$$

with the unit step function $\Theta(x) = \begin{cases} 0, & x < 0 \\ 1, & x \geq 0 \end{cases}$. Depending on the initial filling of the Fermi sea we may observe Rabi oscillations with frequency Ω between state k and

state $k+\pi$. If neither state k nor state $k+\pi$ is initially occupied, both occupations are constant 0 and no oscillations occur since no excitations are possible. In the case of both states being initially occupied, also no excitations are possible and both occupations are constant 1. If state k is initially occupied and state $k+\pi$ unoccupied the occupation of state k oscillates between 1 and 0 with Rabi frequency Ω and the occupation of state $k+\pi$ oscillates between 0 and 1 with the same frequency Ω. This is shown in Figure 4.1. At finite temperatures particles are thermally excited around the Fermi surface such

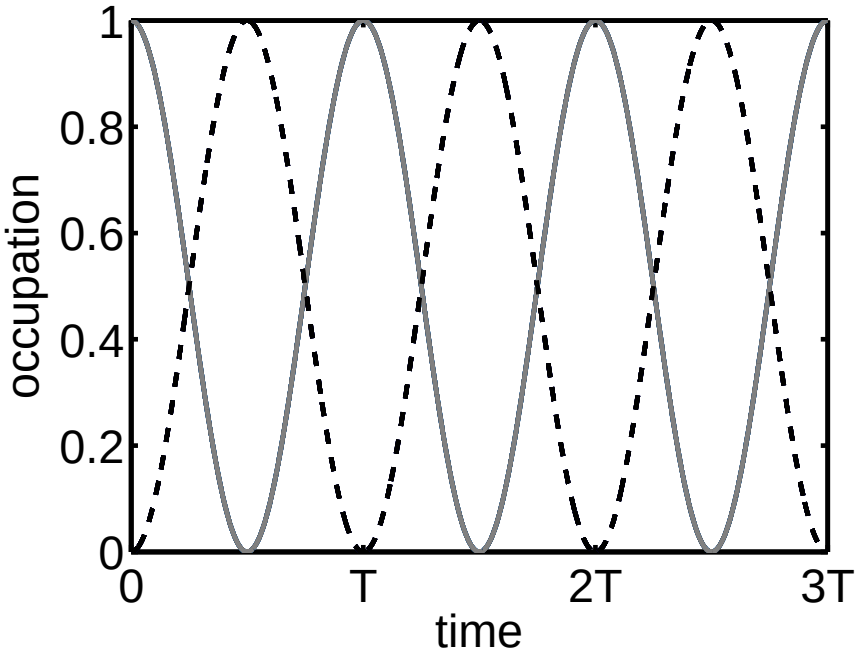

Figure 4.1. – The exact time-dependence of the occupation as a function of time in units of the oscillation period $T = 2\pi/\Omega$ at zero temperature. We investigate the occupation of momentum state $k = \pi/4$. We choose half-filling and hopping parameters $t = 1$ and $h = 0.1t$. We excite on resonance where the rotating wave approximation is valid $\omega = 2\epsilon_k = -4t\cos(k)$. Momentum $k = \pi/4$ is initially occupied and its occupation $\langle n_k(t)\rangle$ (solid line) oscillates between 1 and 0 at zero temperature. The momentum state $k+\pi$ is initially unoccupied. Its occupation $\langle n_{k+\pi}(t)\rangle$ (dashed line) oscillates between 0 and 1.

that the filling softens around k_F. This softening is governed by the Fermi function

$$f(\epsilon_k - \mu) = \frac{1}{1 + e^{\beta(\epsilon_k - \mu)}}, \tag{4.32}$$

where $\beta = (k_B T)^{-1}$ is the inverse temperature. At zero temperature the Fermi function equals 1 for $\epsilon < \mu$ and sharply drops to zero at $\epsilon = \mu$. At finite temperatures this feature softens such that the so-called Fermi tails appears which widens with increasing temperatures. To obtain the finite temperature occupation we have to replace the zero temperature occupation $\langle c_k^\dagger(0)c_k(0)\rangle_0$ in Equation (4.23) by the finite temperature

occupation $\langle c_k^\dagger(0)c_k(0)\rangle_T = f(\epsilon_k - \mu)$ which is given by the Fermi function. We obtain

$$\langle n_k(t)\rangle_T = \left(4\frac{(\epsilon_k - \frac{\hbar\omega}{2})^2}{(\hbar\Omega)^2}\sin^2\left(\frac{\Omega}{2}t\right) + \cos^2\left(\frac{\Omega}{2}t\right)\right) f(\epsilon_k - \mu) \tag{4.33}$$

$$+ 4\frac{(h\tilde{t}\sin(k))^2}{(\hbar\Omega)^2}\sin^2\left(\frac{\Omega}{2}t\right) f(-\epsilon_k - \mu), \tag{4.34}$$

$$\langle n_{k+\pi}(t)\rangle_T = 4\frac{(h\tilde{t}\sin(k))^2}{(\hbar\Omega)^2}\sin^2\left(\frac{\Omega}{2}t\right) f(\epsilon_k - \mu) \tag{4.35}$$

$$+ \left(4\frac{(\epsilon_k - \frac{\hbar\omega}{2})^2}{(\hbar\Omega)^2}\sin^2\left(\frac{\Omega}{2}t\right) + \cos^2\left(\frac{\Omega}{2}t\right)\right) f(-\epsilon_k - \mu). \tag{4.36}$$

The maximum occupation is no longer given by 1 but by the Fermi function $f(\epsilon_k - \mu) \leq 1$. This serves as a direct temperature measurement of the atoms trapped in the lattice for intermediate fillings $\epsilon_{\min} = \epsilon_{k=0} < \mu < \epsilon_{k=\pi} = \epsilon_{\max}$ where the Fermi function yields a clear Fermi tail around the chemical potential μ. Measuring the occupation of the resonant k-value for different perturbing frequencies ranging from $\hbar\omega = 2\epsilon_{k=0}$ to $\hbar\omega = 2\epsilon_{k=\pi}$ will give direct access to the temperature-dependent part in the Fermi function. The amplitude of the $\langle n_k(t)\rangle_T$-oscillation as a function of the corresponding resonance frequency $\epsilon_k = \hbar\omega/2$ yields a temperature-dependent curve which may be fit to the Fermi function with a minimum of fitting parameters, temperature T and chemical potential μ. The temperature may be extracted from the fit. The simplicity of this proposal is thanks to the high k-selectivity of our perturbation. As clear Rabi-oscillations are little likely to be observed in experiment due to the influence of the external trapping potential which couples several momenta we do not go into more detail here. Details concerning the fitting procedure will be discussed in Section 4.1.2 in the linear response treatment since experimental data usually directly relates to this. At zero temperature we compare to numerical results from exact diagonalization [48] of free spinless fermions with an additional external potential corresponding to an optical lattice with time-dependent periodic superlattice driving. The Hamiltonian is given by

$$H = \frac{\hbar^2}{2m}\frac{d^2}{dx^2} + V(x,t), \tag{4.37}$$

$$V(x,t) = V_0\cos^2(k_L x) + \tilde{h}V_0\sin(\omega t)\cos(k_L x), \tag{4.38}$$

where $\hbar = 1.054571726 \cdot 10^{-34}$Js is the reduced Planck constant, $m = 40u$, $u = 1.660538 \cdot 10^{-27}$kg, is the mass of potassium 40 atoms, $k_L = 2\pi/\lambda$ is the laser wave number with wavelength $\lambda = 532$nm, $V_0 = 11.7E_r$ is the strength of the optical lattice potential with recoil energy $E_r = (\hbar k_L)^2/2m$ and $\tilde{h}$ is the small amplitude of the perturbation. We choose $\tilde{h} = 0.001$ and verify that the perturbation is sufficiently small by mapping (4.38) to tight-binding. We determine the energy bands of (4.38) by numeric band structure calculations [48]. At $t = 0$ this corresponds to the equilibrium lattice described by H_0 (4.3) and we fit the dispersion (4.4) to extract the hopping J. At $t = \pi/\omega$ the above potential corresponds to the dimerized tight-binding Hamiltonian $H_0 + hO$ given by Equations (4.3) and (4.5) at $t = \pi/\omega$ with eigenenergies $E_k = \pm\sqrt{2J^2 + 2h^2 + 2(J^2 - h^2)\cos(2k)}$. We fit E_k to the band structure of (4.38) at $t = \pi/\omega$ in order to extract h and find the ratio $h/J \approx 0.035$ which is sufficiently small. We verify the k-selectivity of our perturbation. In Figure 4.2 the occupation as a function of time $\langle n_k(t)\rangle$ for all k in the first Brillouin zone at half-filling is shown. We have 80 lattice site and 80 k-values in the first Brillouin zone accordingly. The

frequency of the perturbation is chosen in such a way that we excite k-value number 25 which is initially occupied. We observe Rabi oscillations for this k-value to k-value number 55 which is initially unoccupied. This corresponds to $\Delta k \approx \pi$ since there are 80 k-values in the first Brillouin zone that are folded into half the Brillouin zone $[0, \pi]$. However, we also observe the excitation of the neighboring momenta but with a weaker amplitude. We attribute this to an error due to the discretization of the continuous model, to finite size effects as well as to the finite duration of the perturbation which leads to a finite width in energy [49]. However, a direct comparison of the analytical

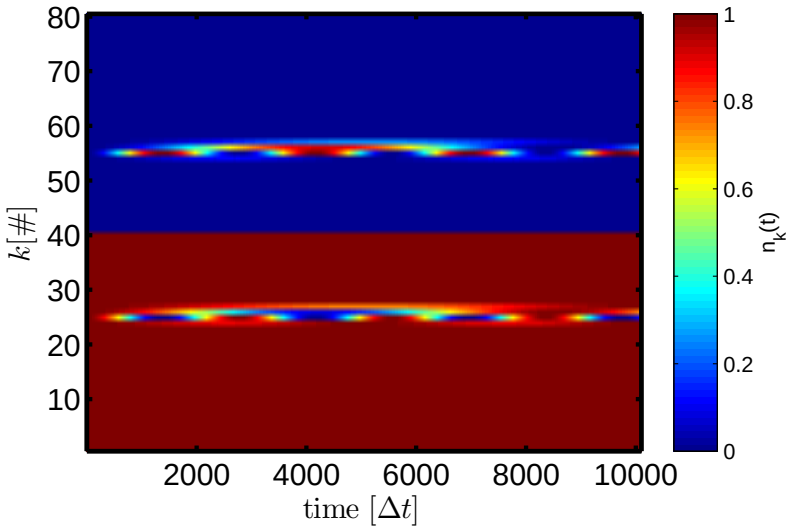

Figure 4.2. – The occupation $\langle n_k(t) \rangle$ (colourmap) from exact diagonalization for all 80 k-values in the first Brillouin zone (y-axes) as a function of time (x-axis) in units of $\Delta t = \hbar \delta t / J$ where $\delta t = 0.0453$ and J is the hopping parameter. Rabi oscillations between states of momentum k and $k + \pi$ are clearly visible on resonance (see main text).

formula $\langle n_k(t) \rangle$ to the numerical results remains difficult due to the bad accuracy of k in the exact diagonalization but high k-sensitivity of the dynamics of $\langle n_k(t) \rangle$.

4.1.2. Energy absorption in linear response theory

For weak perturbations, corresponding to $h << J$ the energy absorption rate $\overline{dE(t)/dt}$ can be computed within linear response theory as introduced in Section 2.1. The energy absorption rate by Equation (2.10). It depends on the intensity $|h|^2$ of the driving field and is proportional to the imaginary part complex susceptibility $Im\chi_{OO^\dagger}$. It is constant in time such that the energy of the system $E(t)$ is increasing linearly in time. Linear response is a common method used in lattice shaking experiments as a linear rise in energy $E(t)$ is usually observed for sufficiently small perturbations. The measurement of $E(t)$ yields a linear slope after a short transient phase and saturates at long times. Measuring the slope m in the linear regime of $E(t)$ directly yields the imaginary part of the complex susceptibility through

$$Im\chi_{OO^\dagger}(\omega) = \frac{-2m}{|h|^2 \omega}. \tag{4.39}$$

Note that the observation of a linear rise in energy is not obvious at first sight. A sinusoidal perturbation resonantly coupling two discrete levels should yield oscillations

between these two levels. However, integration over a group of states yields a linear rise in energy for sufficiently large times [49] which explains the linear slope usually observed in experiment. A system subjected to a periodic modulation of the lattice

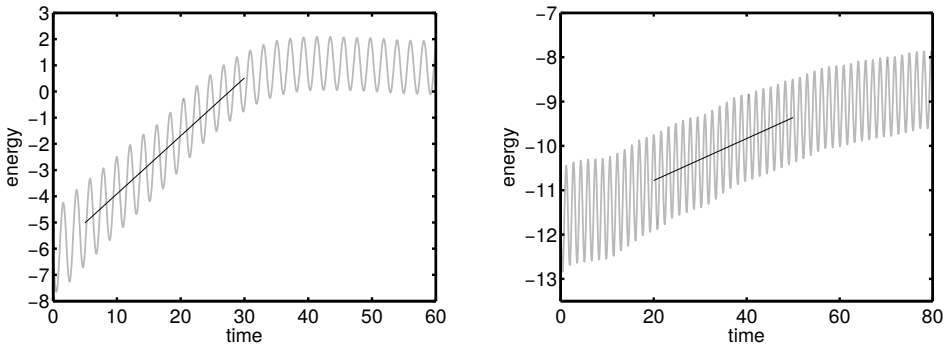

(a) with nearest-neighbor interaction **(b)** with trap

Figure 4.3. – A density matrix renormalization group study of the energy in the system as a function of time for spinless tight-binding fermions in the case of an additional nearest-neighbor interaction in (a) and in the case of an additional external parabolic trapping potential in (b). The Hilbert-space cut-off M and the time step of the Trotter decomposition Δt are chosen according to numerical convergence within the total time considered. All energies are given in units of the hopping $J = 1$ ($\hbar = 1$) such that the time is measured in $1/J$ and we choose the following parameters: in (a) $M = 256$, $\Delta t = 0.1$, nearest-neighbor interaction strength $V = 1$, $\omega = 3$, filling $n = 2/3$ and in (b) $M = 196$, $\Delta t = 0.01$, $V_t = 0.025$, $\omega = 4$, filling $n = 1/2$. In both cases we observe a linear rise (as indicated by the linear solid line) in energy $E(t)$ as expected in experiment (see main text).

potential will on average absorb energy if the modulation frequency approximately corresponds to the energy needed to create an excitation. However, a comparison with density matrix renormalization group calculations [42] of $E(t)$ for one-dimensional spinless non-interacting tight-binding fermions suggests that we would not observe a linear rise in energy. In the case of our particular perturbation no linear slope but distinct oscillations occur due to the high k-selectivity of our perturbation which only couples few momenta. We cover the exact time-dependence for this case in Section 4.1.1 above. However, density matrix renormalization group calculations for spinless fermions show that a linear rise of $E(t)$ is recovered in the case of either an additional nearest-neighbor interaction or an additional external trapping potential which we have in most experiments. This is expected since the nearest-neighbor interaction-term or an additional trapping potential in the Hamiltonian couple different momenta. The nearest-neighbor interaction term in the Hamiltonian is given by

$$H_{\mathrm{nn}} = V \sum_{j}^{L-1} n_j n_{j+1}. \tag{4.40}$$

An additional parabolic trapping potential is given by

$$H_{\mathrm{trap}} = V_t \sum_{j} j^2 n_j, \tag{4.41}$$

where $V_t = (m/2)\omega_t^2 a^2$ with the atom mass m, the trapping frequency ω_t and the lattice spacing a. In Figure 4.3 the energy (in units of the hopping $J = 1$, $\hbar = 1$) as a function of time (in units of $1/J$) for both cases is shown. In both cases the

absorbed energy shows an oscillatory behavior corresponding to the frequency of the perturbing frequency and an energy absorption on average indicated by the linear rise. In 4.3a nearest-neighbor interaction was added and the linear rise in energy is clearly visible up to times $t = 30/J$. The energy then saturates to a constant value around which oscillations persist. In 4.3b an external trapping potential was added. The linear rise is not as strong as for the nearest-neighbor interaction but still distinct for times $t \in (20/J, 60/J)$. As a trapping potential is always present in experiment a linear dependence of $E(t)$ is to be expected and we continue with a linear response treatment.

The zero temperature response At zero temperature all single-particle levels up the Fermi level $\epsilon_F = \mu = -2J\cos(k_F a)$ are occupied, where k_F is the Fermi momentum. We now consider two spin states $\uparrow$ and $\downarrow$ such that the ground state wave function is

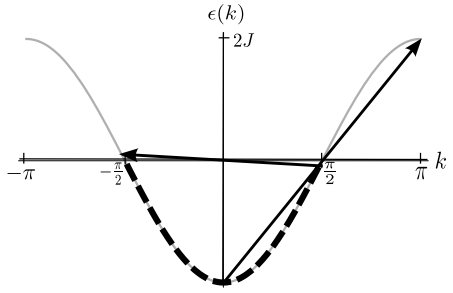

(a) the half-filled band

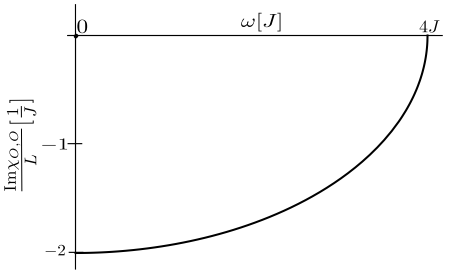

(b) the zero temperature response of the half-filled band

Figure 4.4. – Possible excitations in the half-filled band $k_F = \pi/2$. In Figure (a) the half-filled band in the reduced zone scheme is shown. Excitation energies of $\omega \in (0, 4J]$ are possible. The minimal absorbed energy of ω slightly above 0 corresponds to exciting a particle of momentum slightly below $k = \pi/2$ into an unoccupied state of momentum slightly below $k = 3\pi/2$ in the extended or slightly below $k = -\pi/2$ in the reduced zone scheme as indicated by the shorter arrow. The maximal absorbed energy $\omega = 4J$ corresponds to exciting a particle of momentum $k = 0$ with energy $\epsilon_{k=0} = -2J$ into an unoccupied state of momentum $k = \pi$ with energy $\epsilon_{k=\pi} = 2J$ as indicated by the longer arrow. In Figure (b) the corresponding response function for $J = 1$ is shown. Note that the response drops to zero at $\omega = 4J$ because the pref actor becomes zero.

the Fermi sea

$$|GS\rangle = \prod_{|k|\leq k_F,\sigma} c^\dagger_{k,\sigma}|0\rangle, \tag{4.42}$$

where $|0\rangle$ is the vacuum. We calculate the zero temperature response given by the imaginary part of the complex susceptibility which governs the energy absorption rate (2.10). The complex susceptibility is given by Equation (2.9). We thus need to calculate the equilibrium correlation function $\langle[O(t), O]\rangle_0$, where $\langle\cdot\rangle_0$ denotes the expectation value with respect to the ground state (4.42). The operator $O(t)$ is given in the Heisenberg picture $O(t) = \exp(iH_0t)O\exp(-iH_0t)$ where O is given by Equation (4.5) and H_0 is given by Equation (4.3) such that $[O(t), O] = O(t)O - \text{h.c.}$. We set $a \equiv 1$ and

$\hbar \equiv 1$ and obtain

$$O(t)O = \sum_{k,k',\sigma,\sigma'} \Big\{ e^{i(k+k')} c^\dagger_{k,\sigma}(t) c_{k+\pi,\sigma}(t) c^\dagger_{k',\sigma'} c_{k'+\pi,\sigma'} \tag{4.43}$$

$$+ \quad e^{i(k-k')} c^\dagger_{k,\sigma}(t) c_{k+\pi,\sigma}(t) c^\dagger_{k'+\pi,\sigma'} c_{k',\sigma'} \tag{4.44}$$

$$+ \quad e^{-i(k+k')} c^\dagger_{k+\pi,\sigma}(t) c_{k,\sigma}(t) c^\dagger_{k'+\pi,\sigma'} c_{k',\sigma'} \tag{4.45}$$

$$+ \quad e^{-i(k-k')} c^\dagger_{k+\pi,\sigma}(t) c_{k,\sigma}(t) c^\dagger_{k',\sigma'} c_{k'+\pi,\sigma'} \Big\}. \tag{4.46}$$

We need $\sigma = \sigma'$ to obtain non-zero expectation values in the correlation function. However, k' may be equal to k or $k+\pi$. Considering both these cases leads to

$$O(t)O = \sum_{k,\sigma} \left(1 - e^{2ik}\right) e^{i(\epsilon_k - \epsilon_{k+\pi})t} c^\dagger_{k,\sigma} c_{k,\sigma} \tag{4.47}$$

$$+ \left(1 - e^{-2ik}\right) e^{-i(\epsilon_k - \epsilon_{k+\pi})t} c^\dagger_{k+\pi,\sigma} c_{k+\pi,\sigma} \tag{4.48}$$

$$- \left\{ \left(1 - e^{2ik}\right) e^{i(\epsilon_k - \epsilon_{k+\pi})t} + \left(1 - e^{-2ik}\right) e^{-i(\epsilon_k - \epsilon_{k+\pi})t} \right\} c^\dagger_{k+\pi,\sigma} c^\dagger_{k,\sigma} c_{k,\sigma} c_{k+\pi,\sigma}, \tag{4.49}$$

where we used the Heisenberg equation of motion $c_{k,\sigma}(t) = \exp(-i(\epsilon_k - \mu)t) c_{k,\sigma}$.
It follows

$$[O(t), O] = O(t)O - \text{h.c} \tag{4.50}$$

$$= 4 \sum_{k,\sigma} \sin^2(k) \left(e^{i(\epsilon_k - \epsilon_{k+\pi})t} - e^{-i(\epsilon_k - \epsilon_{k+\pi})t} \right) c^\dagger_{k,\sigma} c_{k,\sigma} \tag{4.51}$$

$$= 4 \sum_{k,\sigma} \sin^2(k) \left(e^{-i\Delta\epsilon_k t} - e^{i\Delta\epsilon_k t} \right) c^\dagger_{k,\sigma} c_{k,\sigma}, \tag{4.52}$$

where $\Delta\epsilon_k := \epsilon_{k+\pi} - \epsilon_k = -2\epsilon_k$. The energy difference $\Delta\epsilon_k$ is the energy injected into the system when exciting a particle from an occupied state of momentum k to an unoccupied state of momentum $k+\pi$. Thus

$$\langle [O(t), O] \rangle_0 = \langle GS | \, [O(t), O] \, | GS \rangle \tag{4.53}$$

$$= 4 \sum_{k,\sigma} \sin^2(k) \left(e^{-i\Delta\epsilon_k t} - e^{i\Delta\epsilon_k t} \right) \langle GS | c^\dagger_{k,\sigma} c_{k,\sigma} | GS \rangle \tag{4.54}$$

$$= 4 \sum_{\sigma} \sum_{k=-k_F}^{k_F} \sin^2(k) \left(e^{-i\Delta\epsilon_k t} - e^{i\Delta\epsilon_k t} \right) \tag{4.55}$$

$$= 8 \sum_{k=-k_F}^{k_F} \sin^2(k) \left(e^{-i\Delta\epsilon_k t} - e^{i\Delta\epsilon_k t} \right). \tag{4.56}$$

The sum in the final result runs over all $|k| \leq k_F$ since the ground state $|GS\rangle$ is the Fermi sea given by Equation (4.42). The response is given by

$$\operatorname{Im} \chi_{O,O} = -8\delta \sum_{k=-k_F}^{k_F} \sin^2(k) \left(\frac{1}{\delta^2 + (\omega - \Delta\epsilon_k)^2} - \frac{1}{\delta^2 + (\omega + \Delta\epsilon_k)^2} \right) \tag{4.57}$$

$$= -8\pi \sum_{k=-k_F}^{k_F} \sin^2(k) \Big(\delta(\omega - \Delta\epsilon_k) - \delta(\omega + \Delta\epsilon_k) \Big). \tag{4.58}$$

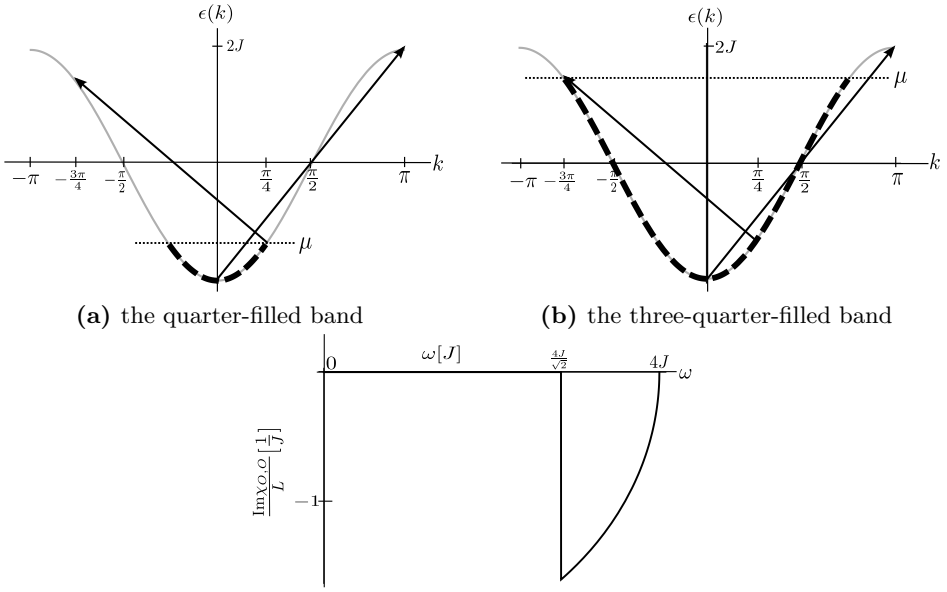

(a) the quarter-filled band

(b) the three-quarter-filled band

(c) the zero temperature response of the quarter- and three-quarter-filled band

Figure 4.5. – Possible excitations in the quarter-filled band $k_F = \pi/4$, Figure (a), and the three-quarter-filled band $k_F = 3\pi/4$, Figure (b), and the corresponding zero temperature response for $J = 1$, Figure (c), which is the same in both cases (see main text). In Figures (a) and (b) the quarter filled band and the three quarter filled band in the reduced zone scheme are shown. The filling is indicated by the chemical potential μ (dotted line). The minimal possible absorption energy corresponds to exciting a particle of momentum $k = \pi/4$ into an unoccupied state of momentum $k = 5\pi/4$ in the extended or $k = -3\pi/4$ in the reduced zone scheme as indicated by the shorter arrows. This corresponds the energy cut-off at $\omega = 4t|\cos(k_F)| = 4t/\sqrt{2}$ in Figure (c). The maximal possible absorption energy corresponds to exciting a particle of momentum $k = 0$ into an unoccupied state of momentum $k = \pi$ as indicated by the longer arrows.

To obtain the continuum limit for $\omega > 0$ we use

$$\sum_k \to \frac{1}{\Delta k} \int \mathrm{d}k = \frac{L}{2\pi} \int_{-k_F}^{k_F} \mathrm{d}k, \tag{4.59}$$

$$\int_{-k_F}^{k_F} \mathrm{d}k f(k) \delta\left(g(k)\right) = \sum_{i=1}^{n} \frac{f(k_i)}{|g'(k_i)|}, \tag{4.60}$$

$$g(k_i) = 0, k_i \in (-k_F, k_F], \tag{4.61}$$

such that the response normalized to the number of lattice sites L becomes

$$\frac{\mathrm{Im}\,\chi_{O,O}}{L} = -\frac{2}{J}\sqrt{1 - \left(\frac{\omega}{4J}\right)^2} \cdot \Theta\left(\omega - 4J|\cos(k_F)|\right), \tag{4.62}$$

where $\omega_{\min} = 4J|\cos(k_F)| > 0$ is the minimal energy transfer possible according to the filling. The maximum possible energy transfer is $\omega_{\max} = 4J$ which is the band width and corresponds to exciting a particle from the momentum state $k = 0$ with energy $\epsilon_{k=0} = -2J$ into the momentum state $k = \pi$ with energy $\epsilon_{k=\pi} = 2J$. This transfer is possible for all fillings except if the band is completely empty or completely occupied. The energy range of absorption increases for increasing Fermi momenta k_F and $k_F < \pi/2$ since $\omega_{\min} = 4J|\cos(k_F)|$ decreases from $4J$ to 0 when k_F is increased from zero filling $k_F = 0$ to half-filling $k_F = \pi/2$. Note that $\omega_{\min} = 0$ is not possible though since at $k_F = \pi/2$ both states $k_F = \pm\pi/2$ are occupied which prevents the transfer. In addition, no transfer may be caused by a static perturbation $\omega = 0$. Increasing k_F even further above $\pi/2$ the energy range of absorption decreases again for increasing Fermi momenta since $\omega_{\min}$ increases from slightly above 0 to $4J$ when k_F is increased from half-filling $k_F = \pi/2$ to a completely filled band $k_F = \pi$.
The energy range of absorption is maximal $\omega \in (0, 4J]$ at $k_F = \pi/2$ since all states up to $k = \pi/2$ are filled such that $\omega_{\min}$ slightly above 0 and empty states are available to transfer particles from k to $k + \pi$ for all $k < k_F$. This situation is shown in Figure 4.4. For $k_F < \pi/2$ not enough states below $k = \pi/2$ are occupied to obtain an energy transfer of $\omega < 4J|\cos(k_F)|$. For $k_F > \pi/2$ the energy range of absorption decreases again because the empty states above $k = \pi/2$ which are needed for the excitation get successively occupied. The response is symmetric around $k_F = \pi/2$ such that $k_F < \pi/2$ and $2\pi - k_F > \pi/2$ show the same response. This situation is displayed in Figure 4.5. Note that the response is suppressed at $\omega = 4J$ for all k_F because the prefactor $\sim \sin^2(k)$ equals zero at $k = 0$. The strongest response occurs at $\omega_{\min}$ where the prefactor takes its maximum value. In the continuum limit this is reflected in the $\sqrt{1 - \left(\frac{\omega}{4J}\right)^2}$-dependence.

The finite temperature response At finite temperature particles are thermally excited around the Fermi surface such that the filling softens around μ. This softening is governed by the Fermi function

$$f(\epsilon_k - \mu) = \frac{1}{1 + e^{\beta(\epsilon_k - \mu)}}, \tag{4.63}$$

where $\beta = k_B T$ is the inverse temperature. At zero temperature the Fermi function equals 1 for $\epsilon < \mu$ and sharply drops to zero at $\epsilon = \mu$. At finite temperatures this feature softens such that the so-called Fermi tails appears which widens with increasing temperatures. We expect the sharp cut-off at the filling in the zero temperature

response to soften and show a Fermi tail.
To obtain the finite temperature response we have to replace $\langle GS|c^\dagger_{k,\sigma}c_{k,\sigma}|GS\rangle$ by $\langle c^\dagger_{k,\sigma}c_{k,\sigma}\rangle_T$ in the equilibrium correlation function given by Equation (4.55). The finite temperature expectation value of the number operator $n_{k,\sigma} = c^\dagger_{k,\sigma}c_{k,\sigma}$ is given by the Fermi function,

$$\langle c^\dagger_{k,\sigma}c_{k,\sigma}\rangle_T = f(\epsilon_k - \mu). \tag{4.64}$$

We obtain

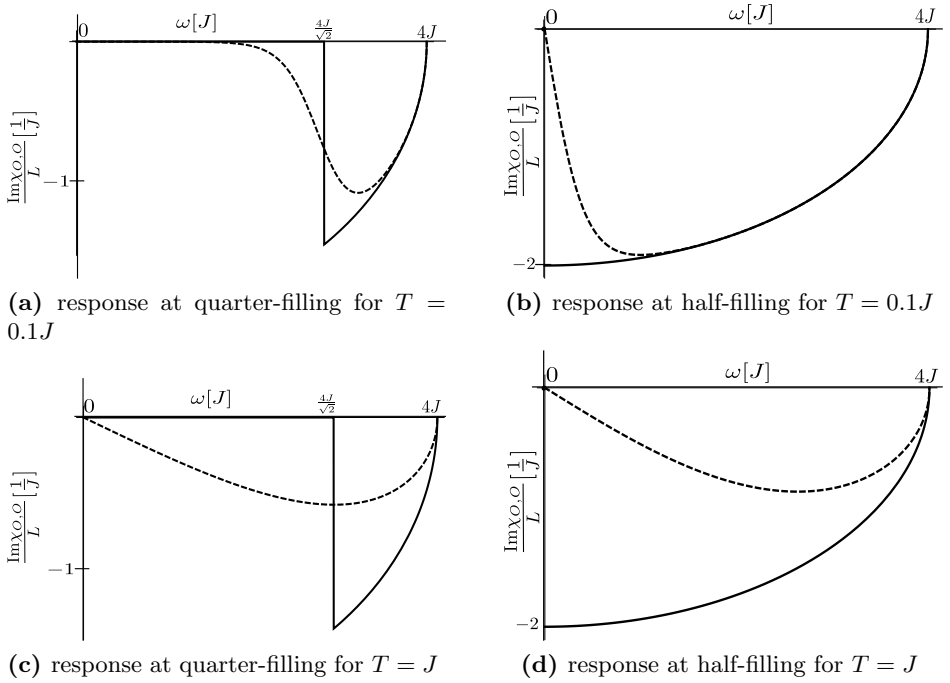

(a) response at quarter-filling for $T = 0.1J$

(b) response at half-filling for $T = 0.1J$

(c) response at quarter-filling for $T = J$

(d) response at half-filling for $T = J$

Figure 4.6. – We compare the finite temperature response (dashed line) to the zero temperature response (solid line) for $J = 1$ and two different temperatures at quarter-filling (equivalent to three-quarter-filling) and half-filling. In Figure (a) the response for quarter-filling and in Figure (b) the response for half-filling are shown for a small temperature of $T = 0.1J$. The Fermi tail is clearly visible in the finite temperature response, in particular in the case of quarter-filling. In Figure (c) the response for quarter-filling and in Figure (d) the response for half-filling are shown for a larger temperature of the order of the hopping parameter $T = J$. In contrast to the low temperature case the occupancy is smeared out over the entire band such that the temperature dependence is less distinct and excitations at all energies are possible.

$$\langle [O(t), O]\rangle_T = 8\sum_k \sin^2(k) f(\epsilon_k - \mu)\left(e^{-i\Delta\epsilon_k t} - e^{i\Delta\epsilon_k t}\right). \tag{4.65}$$

Note that the sum now runs over all k in the first Brillouin zone in contrast to the zero temperature case since the Fermi momentum k_F is no longer defined. Cutting the sum at k_F is now replaced by the Fermi factor which smoothly cuts of the response and

introduces a temperature dependence. The response is given by

$$\frac{\mathrm{Im}\,\chi_{O,O}}{L} = -\frac{8\delta}{L}\sum_k \sin^2(k) f(\epsilon_k - \mu)\left(\frac{1}{\delta^2 + (\omega - \Delta\epsilon_k)^2} - \frac{1}{\delta^2 + (\omega + \Delta\epsilon_k)^2}\right) \tag{4.66}$$

$$= -\frac{8\pi}{L}\sum_k \sin^2(k) f(\epsilon_k - \mu)\left(\delta(\omega - \Delta\epsilon_k) - \delta(\omega + \Delta\epsilon_k)\right) \tag{4.67}$$

$$= \frac{2}{J}\sqrt{1 - \left(\frac{\omega}{4J}\right)^2}\left(f\left(\frac{\omega}{2} - \mu\right) - f\left(-\frac{\omega}{2} - \mu\right)\right). \tag{4.68}$$

At zero temperature the filling is given by μ such that the response is cut off at the corresponding minimal excitation energy. Here, in the finite temperature case, the filling is softened around the Fermi surface leading to a Fermi tail in the response. The Fermi tail is clearly visible for intermediate fillings away from zero, half or complete filling. The finite temperature response in comparison to the zero temperature response for different temperatures is shown in Figure 4.6. The softening is of the order of magnitude of $k_B T$ such that is gets completely washed out for temperatures approaching the order of magnitude of J. Particles are smeared out over the entire band such that the range of excitations covers the maximal range $\omega \in (0, 4J]$ even for smaller fillings, but with a reduced amplitude.

The response of the trapped system The study of the one-dimensional homogeneous system is very instructive since it becomes clear what excitations are possible depending on the filling at zero temperature and how the cut-off softens due to thermal excitations at finite temperatures. However, since we aim at measuring the energy absorption and extracting the temperature from it, we need to study a setup that is more realistic in experiment, i.e. adding an external trapping potential and considering three dimensions for the equilibrium system.
In three dimensions the single-band tight binding Hamiltonian is analogous to the one-dimensional case give by Equation (4.1) where the sum over j now sums over all three-dimensional lattice vectors $\vec{r}_j$. The dispersion is now given by

$$\epsilon_{\vec{k}} = \epsilon_{k_x} + \epsilon_{k_y} + \epsilon_{k_z} \tag{4.69}$$

$$= -2J\cos(k_x) - 2J\cos(k_y) - 2J\cos(k_z). \tag{4.70}$$

We consider an isotropic harmonic trapping potential

$$V(\vec{r}) = V_t\left(\frac{|\vec{r}|}{a}\right)^2, \tag{4.71}$$

with strength $V_t = (m/2)\omega_t^2$, where ω_t is called the trapping frequency.
The total response in the trap is determined within the local density approximation as introduced in Section 2.2. The space dependence of the external trapping potential is incorporated into the chemical potential. The total response is then obtained by summing the response of the homogeneous system over the chemical potential which varies when moving through the trap. We choose to normalize the strength of the trapping potential by half the bandwidth such that the characteristic density ρ given by Equation (2.21) becomes

$$\rho_{1D} = N\sqrt{\frac{V_t}{2J}}, \tag{4.72}$$

$$\rho_{3D} = N\left(\frac{V_t}{6J}\right)^{3/2} \tag{4.73}$$

in one and three dimensions respectively.
The mean response, which is the total response in the trap normalized to the total number of particles becomes

$$\overline{\operatorname{Im}\chi_{O,O}}_{1D} = \frac{1}{N_{1D}}\sqrt{\frac{2J}{V_t}}\int_{-\infty}^{\bar{\mu}_0} \mathrm{d}\bar{\mu}\frac{1}{\sqrt{\bar{\mu}_0-\bar{\mu}}}\frac{\operatorname{Im}\chi_{O,O}(\bar{\mu}\cdot 2J)}{L}, \tag{4.74}$$

$$\overline{\operatorname{Im}\chi_{O,O}}_{3D} = \frac{2\pi}{N_{3D}}\left(\frac{6J}{V_t}\right)^{3/2}\int_{-\infty}^{\bar{\mu}_0} \mathrm{d}\bar{\mu}\sqrt{\bar{\mu}_0-\bar{\mu}}\frac{\operatorname{Im}\chi_{O,O}(\bar{\mu}\cdot 6J)}{L}, \tag{4.75}$$

in one and three dimensions with $\bar{\mu} = \mu/2J$ and $\bar{\mu} = \mu/6J$ respectively. In both cases

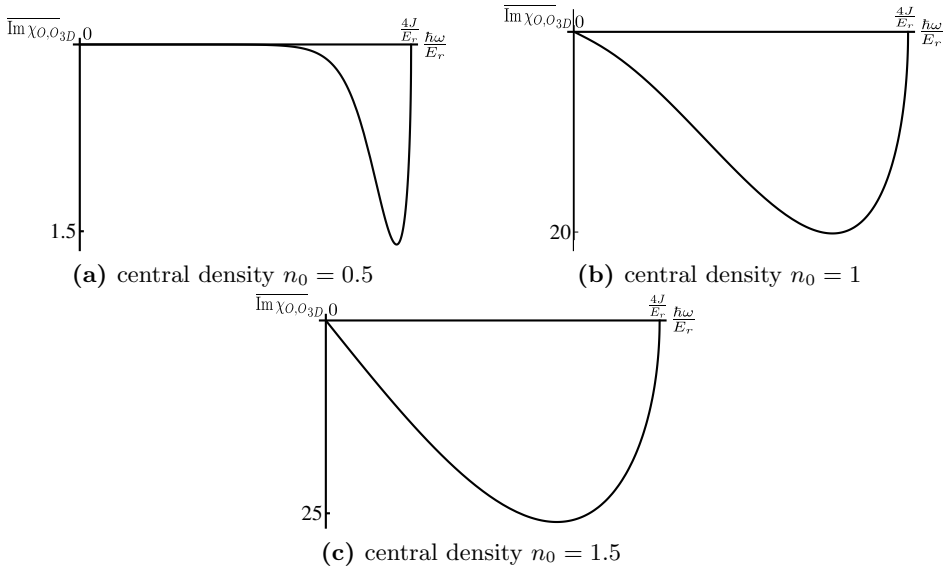

(a) central density $n_0 = 0.5$ **(b)** central density $n_0 = 1$

(c) central density $n_0 = 1.5$

Figure 4.7. – The total response $\overline{\operatorname{Im}\chi_{O,O}}_{3D}$ of the three-dimensional system perturbed along one direction taking into account an external trapping potential for a temperature $T = 0.1J$, different central densities n_0 and parameters specified in 4.84-4.87. The Fermi tail is clearly visible in the case of a central density $n_0 = 0.5$ in Figure (a) and gets less distinct at a central density of $n_0 = 1$ in Figure (b). In contrast to the homogeneous system, where densities of $n = 0.5$ and $n = 1.5$ lead to the same absorption, this is no longer the case in the inhomogeneous system. At a central density of $n_0 = 1.5$ in Figure (c) absorption now occurs over the entire energy absorption range since all densities below $n_0 = 1.5$ contribute.

$\operatorname{Im}\chi_{O,O}/L(\bar{\mu})$ is the response of the one-dimensional homogeneous system normalized to the number of lattice sites L. Note that the response of the one-dimensional homogeneous system governs the total response in three dimensions since our periodic perturbation is only applied along one direction. However, the total particle number N given by Equation (2.20) depends on the one-dimensional and three-dimensional density respectively such that the same central chemical potential μ_0 corresponds to different particle numbers N_{1D} and N_{3D}. The particle numbers are given by

$$N_{1D} = \sqrt{\frac{2J}{V_t}}\int_{-\infty}^{\bar{\mu}_0} \mathrm{d}\bar{\mu}\frac{1}{\sqrt{\bar{\mu}_0-\bar{\mu}}}\, n_{1D}(\bar{\mu}\cdot 2J), \tag{4.76}$$

$$N_{3D} = 2\pi\sqrt{\frac{6J}{V_t}}^3\int_{-\infty}^{\bar{\mu}_0} \mathrm{d}\bar{\mu}\sqrt{\bar{\mu}_0-\bar{\mu}}\, n_{3D}(\bar{\mu}\cdot 6J), \tag{4.77}$$

with the densities of the homogeneous system

$$n_{1D} = n_{1D,\uparrow} + n_{1D,\downarrow} = \frac{1}{L}\sum_{j,\sigma}\langle c^{\dagger}_{j,\sigma} c_{j,\sigma}\rangle \tag{4.78}$$

$$= \frac{2}{L}\sum_{k} f(\epsilon_k - \mu) \tag{4.79}$$

$$= \frac{2}{\pi}\int_{-\pi}^{\pi} f(\epsilon_k - \mu)\mathrm{d}k, \tag{4.80}$$

$$n_{3D} = \frac{2}{L^3}\sum_{\vec{k}} f(\epsilon_{\vec{k}} - \mu) \tag{4.81}$$

$$= \frac{2}{\pi^3}\int_{-\pi}^{\pi}\int_{-\pi}^{\pi}\int_{-\pi}^{\pi} \mathrm{d}k_x \mathrm{d}k_y \mathrm{d}k_z f(\epsilon_{\vec{k}} - \mu). \tag{4.82}$$

In the three dimensional case the result may easily be generalized to an anisotropic confinement by replacing V_t by the mean value $\bar{V}_t = (V_{t,x}V_{t,y}V_{t,z})^{1/3}$. For central densities $n_0 < 1$ the response shows similar behavior as in the homogeneous case. The Fermi tail is clearly visible for central densities of $n_0 \sim 0.5$ and gets less distinct for $n_0 \to 1$ which is shown in Figure 4.7. However, for larger central densities $n_0 > 1$ the response no longer resembles the homogeneous case since all densities below $n_0 > 1$ contribute and are summed up. Absorption occurs over the entire range and the temperature dependence is less distinct.
In experiment the total particle number N is known and may be controlled. For a certain particle number we want to extract the temperature and the central chemical potential from the measured full response given by Equation (4.75). We theoretically test this procedure by first interpolating the central chemical potential μ_0 as a function of total particle number N using Equation (4.77) for central densities between $n \sim 0$ and $n \sim 1$. For a certain particle number, we calculate eight data points for the full three-dimensional response given by Equation (4.75) between $\omega = 0$ and $\omega = 4J$ (corresponding to the minimum and maximum possible energy transfer as explained in Section (4.1.2)) since this a realistic amount of data for experiment. We then fit the same Equation (4.75) for the full response but including an overall constant prefactor as the measured intensity in experiment may deviate from theory. Fit parameters are the constant prefactor, the temperature T and the central chemical potential μ_0. We use educated guesses as starting values for the fit parameters and consider a temperature range between $T = 0.1J$ and $T = J$. We test the procedure for experimentally realistic parameters for a gas of potassium 40 atoms in a three-dimensional optical lattice with harmonic confinement. The parameters are the following,

$$J = \hbar 10^3\mathrm{Hz}, \tag{4.83}$$

$$\omega_t = 2\pi \cdot 70\mathrm{Hz}, \tag{4.84}$$

$$m = 40u\,(^{40}\mathrm{K}), \tag{4.85}$$

$$\lambda = 1064\mathrm{nm} \tag{4.86}$$

$$a = \frac{\lambda}{2}, \tag{4.87}$$

where u is the atomic mass unit. We normalize by the recoil energy $E_r = (\hbar k)^2/2m = h^2/2m\lambda^2$ where h is Planck's constant and $\hbar = h/2\pi$. Note that the trapping frequency $\omega_t < 4J/\hbar = \omega_{\max}$.

Discussion Note one important aspect that we have neglected so far. Collective excitations of the trapped atomic cloud may be triggered by our perturbation. There are different kinds of in-trap modes for harmonically trapped clouds in three dimensions [50]. One distinguishes between surface excitations and compressional modes. The most important surface mode is the so-called dipole mode. The entire cloud oscillates in the trap at the trapping frequency ω_t. The motion of the center of mass is that of a free particle moving in a harmonic oscillator potential. Another surface mode is the quadrupole mode. Also of importance is the so-called monopole mode or breathing mode which is a compressional mode. For a non-interacting Fermi gas the quadrupole mode and the breathing mode are given by $2\omega_t$. As the collective frequencies lie within the bandwidth $4J$ which is the range of the perturbing frequency ω, in-trap modes will be excited at certain frequencies. We need to be aware that the above results are not valid at these frequencies and the measurements have to be excluded.

The fitting procedure works perfectly for all considered temperatures up to central densities of $n_{0,3D} = 1$. For the highest temperature of the order of the hopping strength $T = J$ we obtain the exact values for the fitting parameters down to central densities $n_{0,3D} \sim 0.1$. The lower bound increases for decreasing temperatures. However, fitting works down to central densities of $n_{0,3D} \sim 0.4$ for the lowest temperature $T = 0.1J$. In Figure 4.8 the data points are compared to the response given by Equation (4.75) for a prefactor, a temperature and a central chemical potential obtained from the fit.

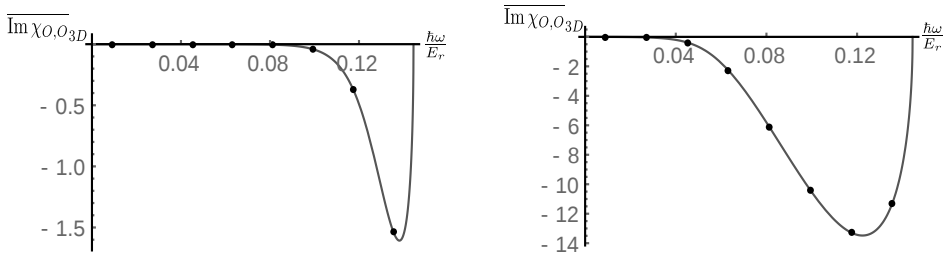

(a) central density $n_0 = 0.5$ **(b)** central density $n_0 = 0.8$

Figure 4.8. – The total response $\overline{\mathrm{Im}\,\chi_{O,O_{3D}}}$ of the three-dimensional case for 8 data points and the fit of the full function to these data points for $T = 0.1J$. The fit function is the full response given by (4.75) including a constant prefactor. Fit parameters are the prefactor, the temperature T and the central chemical potential μ_0

The quantity of interest is the entropy per particle $s = S/N$ rather than the absolute temperature T. In condensed matter systems, temperature is imposed by a reservoir of fixed temperature. In contrast, cold atom systems are isolated quantum systems such that the absolute temperature is very sensitive to small parameter changes. But slow parameter changes are assumed to be adiabatic such that the entropy may be considered constant. The entropy is a measure of the number of accessible quantum states and constitutes a good quantity to characterize quantum phase transitions in cold atom systems. Hence, the term cooling refers to lowering the entropy per particle s and not to lowering absolute temperature T.
In experiment cooling is typically achieved without a lattice. A standard procedure is to then ramp up the lattice adiabatically (at constant entropy) into the strong coupling regime until approximately one particle per site over most of the trap. The Néel temperature T_N for entering the antiferromagnetic state has a maximum at intermediate couplings U/J and is of the order of the antiferromagnetic coupling strength $k_B T_N \sim 4J^2/U$ in the strong coupling regime where the system at half-filling is de-

scribed by a Heisenberg chain. The entropy per particle s_N corresponding to T_N is exponentially small at weak coupling such that the antiferromagnetic state is difficult to reach in the weak-coupling regime by directly cooling to such low entropy. However, s_N reaches a finite value at large U/J which is given by the entropy per particle of the quantum Heisenberg model at its critical point $s_H = k_B \ln 2$. Only spin degrees of freedom remain present below this value and magnetic ordering becomes possible. Quantum fluctuations further reduce this number to about $s_N = 0.5 k_B \ln 2$ in the cubic lattice [51]. This corresponds to a temperature $k_B T/T_F = s_N/\pi^2 \approx 0.035 k_B$ for non-interacting particles in an external trapping potential [52] which is much higher than T_N at weak coupling. Antiferromagnetic ordering can not be achieved at this entropy in the weak coupling limit. However, cooling non-interacting particles to this temperature and then following the equal entropy line in the T-U-phase diagram towards higher interactions by adiabatically ramping up the lattice is a prospective way. Temperature is further reduced and the antiferromagnetic phase is reached at intermediate fillings [51]. When further following the equal entropy to even stronger interactions, the temperature increases again. This Mott insulating regime at intermediate filling is where antiferromagnetic ordering is most likely to be observed.
We want to get a rough idea of how the temperatures considered here in the above measurement scheme compare to this low-temperature regime of interest in the Fermi-Hubbard phase diagram. In the Mott insulating regime at intermediate filling the entropy is high in the liquid wings but small and approximately constant across the central Mott plateau [53]. The central density is also constant. We therefore neglect the trapping potential to get a first rough estimate of s corresponding to the temperatures considered above. We compute s for a cubic lattice at half-filling. We consider $L = 100$ lattice sites in each direction which is a reasonable number in experiment. The highest temperature considered $T = J$ corresponds to $S/N \approx 0.8 k_B$ which is perfectly attainable in current experiments. Our temperature measurement works down to temperatures of $T = 0.1J$ that correspond to $S/N \approx 0.09 k_B$ which is way below what has been achieved in experiment so far. Furthermore, this is also well below $s_N = 0.5 k_B \ln 2$, the entropy expected for the Néel transition.

In the next Section we repeat the same analysis for a slightly different equilibrium system which is the dimerized fermionic non-interacting tight-binding mode. However, a detailed analysis of the possible experimental implementation of the above discussion with a focus on the measurement procedure follows in Section 4.4.

4.2. Non-interacting tight-binding fermions with dimerized hopping subjected to a periodic perturbation

We repeat all steps from Section 4.1.2, computing the response function to an external superlattice modulation defined by Equation (1.20) for a slightly different equilibrium system. We now consider the dimerized fermionic non-interacting tight-binding model given by Equation (4.89) as our equilibrium Hamiltonian. In the dimerized case the hopping amplitude alternates between neighboring sites. In this case the modulation wraps up to modulating the dimerized lattice around a mean value as indicated in Figure 4.9. The bottom offset is constant as in the non-dimerized case.

The homogeneous system in one dimension The single-band tight binding Hamiltonian for non-interacting fermions in a dimerized optical lattice in one dimension is

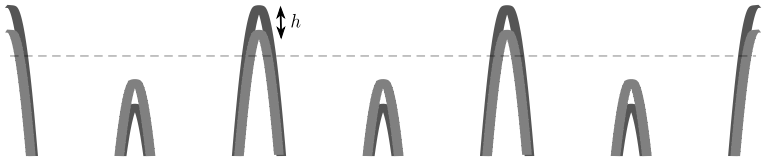

Figure 4.9. – Periodic modulation of the dimerized lattice. The lattice is modulated between the two configurations, dark solid line and light solid line around a mean value (dashed line).

given by

$$H = -\sum_{j,\sigma}^{L}(J_1 + (-1)^j J_2)(c^\dagger_{j,\sigma}c_{j+1,\sigma} + \text{h.c.}) - \mu\sum_{j,\sigma}^{L} c^\dagger_{j,\sigma}c_{j,\sigma} \tag{4.88}$$

$$= -J\sum_{j\,\text{odd},\sigma}(c^\dagger_{j,\sigma}c_{j+1,\sigma} + \text{h.c.}) - J'\sum_{j\,\text{even},\sigma}(c^\dagger_{j,\sigma}c_{j+1,\sigma} + \text{h.c.}) - \mu\sum_{j,\sigma} c^\dagger_{j,\sigma}c_{j,\sigma}, \tag{4.89}$$

where $J = J_1 - J_2$ and $J' = J_1 + J_2$. We define all hopping parameters to be positive and $J_1 > J_2$ such that $J' > J$. The size of the unit cell is doubled with respect to the non-dimerized lattice in Section 4.1 such that the lattice spacing is now given by $2a$. There is two sites per unit cell that may be assigned to two sub-lattices with creation and annihilation operator $a^{(\dagger)}_{j,\sigma}$ and $b^{(\dagger)}_{j,\sigma}$ that connect to the original lattice via

$$a_{j\sigma} = c_{2j+1,\sigma}, \tag{4.90}$$

$$b_{j\sigma} = c_{2j,\sigma}, \qquad j = 1,\ \ldots\ , \frac{L}{2}. \tag{4.91}$$

The Hamiltonian becomes

$$H = -J\sum_{j,\sigma}^{L/2}(a^\dagger_{j,\sigma}b_{j,\sigma} + \text{h.c.}) - J'\sum_{j,\sigma}^{L/2}(a^\dagger_{j+1,\sigma}b_{j,\sigma} + \text{h.c.}) - \mu\sum_{j,\sigma}^{L/2}(a^\dagger_{j,\sigma}a_{j,\sigma} + b^\dagger_{j,\sigma}b_{j,\sigma}). \tag{4.92}$$

The Fourier transform

$$a_{j,\sigma} = \sqrt{\frac{2}{L}}\sum_k e^{ik2aj}a_{k,\sigma}, \tag{4.93}$$

$$b_{j,\sigma} = \sqrt{\frac{2}{L}}\sum_k e^{ik2aj}b_{k,\sigma}, \tag{4.94}$$

leads to

$$H = -\sum_{k,\sigma}\Big((J + J'e^{-2ik})a^\dagger_{k,\sigma}b_{k,\sigma} + \text{h.c.}\Big) - \mu\sum_{k,\sigma}(a^\dagger_{k,\sigma}a_{k,\sigma} + b^\dagger_{k,\sigma}b_{k,\sigma}), \tag{4.95}$$

where we set $a \equiv 1$. The first Brillouin zone has half the size $(-\frac{\pi}{2}, \frac{\pi}{2}]$ compared to the case without dimerization (see Section 4.1). The lattice momentum has the same discretization $k = 2\pi l/L$ but $l = -L/4 + 1, ..., L/4$ such that there is only half the number of k-values $L/2$. However, the total number of available states $2L$ is the same since there is now two sites per unit cell and two possible spin configurations per site. We diagonalize the Hamiltonian by the following transformation

$$\alpha_{k,\sigma} = u_k a_{k,\sigma} - v_k b_{k,\sigma}, \tag{4.96}$$

$$\beta_{k,\sigma} = u_k a_{k,\sigma} + v_k b_{k,\sigma}, \tag{4.97}$$

where

$$u_k = \frac{1}{\sqrt{2}} \exp\left(-i\frac{\varphi(k)-k}{2}\right), \tag{4.98}$$

$$v_k = \frac{1}{\sqrt{2}} \exp\left(-i\frac{\varphi(k)-k}{2}\right), \tag{4.99}$$

with

$$\varphi(k) = \begin{cases} \arctan\left(-\frac{(J'-J)\sin(k)}{(J'+J)\cos(k)}\right), & k \in (-\frac{\pi}{2}, \frac{\pi}{2}) \\ -\frac{\pi}{2}, \quad k = \frac{\pi}{2} \end{cases} . \tag{4.100}$$

We obtain

$$H = \sum_{k,\sigma} E_k(\alpha^\dagger_{k,\sigma}\alpha_{k,\sigma} - \beta^\dagger_{k,\sigma}\beta_{k,\sigma}) - \mu \sum_{k,\sigma}(\alpha^\dagger_{k,\sigma}\alpha_{k,\sigma} + \beta^\dagger_{k,\sigma}\beta_{k,\sigma}) \tag{4.101}$$

with

$$E_k = \sqrt{J'^2 + J^2 + 2JJ'\cos(2k)}. \tag{4.102}$$

The sub-lattice structure leads to the emergence of two energy bands which is shown in Figure 4.10. A positive energy band $+E_k$ corresponding to quasiparticles α and a negative energy band $-E_k$ corresponding to quasiparticles β. An energy gap Δ opens between the two bands due to the dimerization. The energy gap and the total band width W are given by

$$\Delta = 2(J' - J), \tag{4.103}$$

$$W = 2(J' + J). \tag{4.104}$$

In the case $J' = J$ the gap closes and the total bandwidth $W = 4J$. We recover the non-dimerized case treated in Section 4.1. Applying the same transformation to the

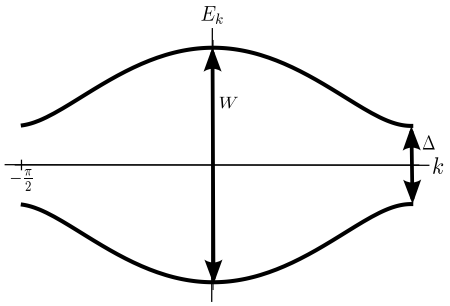

Figure 4.10. – The band structure of the dimerized lattice. The dimerization leads to the emergence of two energy bands of $\pm E_k$ with total bandwidth W and a gap Δ opening at the Brillouin zone border $k = \pm\pi/2$.

perturbing operator given by Equation (1.22) leads to

$$O = \sum_{j,\sigma}(-1)^j(c^\dagger_{j,\sigma}c_{j+1,\sigma} + \text{h.c.}), \tag{4.105}$$

$$= \sum_{k,\sigma}(e^{-2ik} - 1)a^\dagger_{k,\sigma}b_{k,\sigma} + \text{h.c.}, \tag{4.106}$$

$$= \sum_{k,\sigma} C_0(k)(\alpha^\dagger_{k,\sigma}\alpha_{k,\sigma} - \beta^\dagger_{k,\sigma}\beta_{k,\sigma}) + C(k)(\beta^\dagger_{k,\sigma}\alpha_{k,\sigma} - \text{h.c.}), \tag{4.107}$$

with

$$C_0(k) = 2\sin(k)\sin(\varphi(k)), \tag{4.108}$$
$$C(k) = 2i\sin(k)\cos(\varphi(k)). \tag{4.109}$$

The perturbing operator O now transfers particles from occupied α-states of momentum k in the lower band to unoccupied β-states of same momentum k in the upper band. This may seem as a contradiction to the non-dimerized case where we found that the perturbation introduces momentum π. This was due to the fact, that the perturbation has a periodicity which is twice the periodicity of the equilibrium system. In contrast, in the dimerized case the equilibrium system and the perturbation have the same periodicity such that lattice momentum is conserved and we do not expect a momentum transfer. A momentum difference of π in the dimerized system corresponds to equal momentum since the periodicity of the reciprocal lattice is $2\pi/2a \equiv \pi$.
In the following we compute the response of the dimerized system to the periodic perturbation completely analogous to the non-dimerized case treated in Section 4.1. We mainly give the results and interpret these. For details in the calculations refer to the non-dimerized case in Section 4.1.

4.2.1. Energy absorption in linear response theory

The zero temperature response At zero temperature all single-particle levels up to the Fermi level are occupied. Note that the same Fermi momentum k_F can either correspond to a negative Fermi energy $E_F < 0$ if only states in the lower band are occupied or to a positive Fermi energy $E_F > 0$ if also states in the upper band are occupied. The ground state wave function is the Fermi sea

$$|GS\rangle = \prod_{|k|\leq k_F,\sigma} \beta^\dagger_{k,\sigma}\alpha^\dagger_{k,\sigma}|0\rangle, \tag{4.110}$$

where $|0\rangle$ is the vacuum and we need to keep in mind whether the Fermi surface lies at negative or positive energies. We calculate the zero temperature response given by Equation (2.10). We need to calculate the correlation function $\langle[O(t), O]\rangle_0$, where $\langle\cdot\rangle_0$ denotes the expectation value with respect to the ground state $|GS\rangle$. We start by calculating the response for less than or equal to half-filling. The product $O(t)O$ is given by

$$O(t)O = \sum_{k,k',\sigma,\sigma'} |C_0(k)|^2\beta^\dagger_{k,\sigma}\beta_{k,\sigma}\beta^\dagger_{k',\sigma'}\beta_{k',\sigma'} \tag{4.111}$$
$$+|C_0(k)|^2\alpha^\dagger_{k,\sigma}\alpha_{k,\sigma}\alpha^\dagger_{k',\sigma'}\alpha_{k',\sigma'} \tag{4.112}$$
$$+|C(k)|^2\beta^\dagger_{k,\sigma}\alpha_{k,\sigma}\alpha^\dagger_{k',\sigma'}\beta_{k',\sigma'}e^{-2iE_kt} \tag{4.113}$$
$$+|C(k)|^2\alpha^\dagger_{k,\sigma}\beta_{k,\sigma}\beta^\dagger_{k',\sigma'}\alpha_{k',\sigma'}e^{2iE_kt}, \tag{4.114}$$

where we used $\alpha_{k,\sigma}(t) = \exp(-i(E_k - \mu)t)\alpha_{k,\sigma}$ and $\beta_{k,\sigma}(t) = \exp(-i(-E_k - \mu)t)\beta_{k,\sigma}$. Note that the expectation values in the correlation function will only be non-zero for $k = k'$ and $\sigma = \sigma'$ such that the sum over k' and σ' may be omitted. The terms (4.112) and (4.114) may also be dropped in the correlation function due to the fact that the

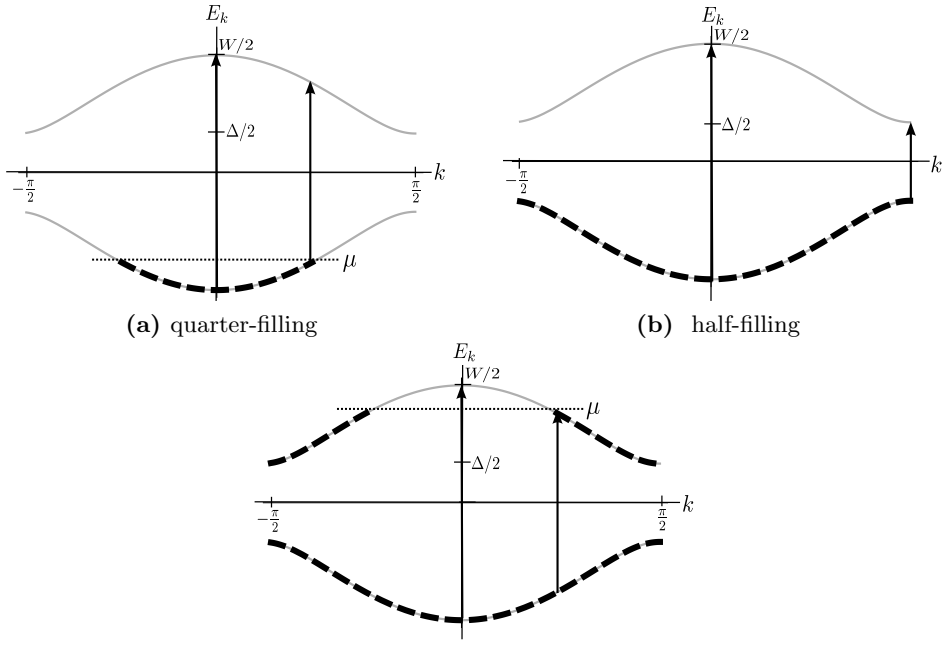

(a) quarter-filling **(b)** half-filling

(c) three-quarter-filling

Figure 4.11. – The ω-range of possible excitations in the dimerized system depends on the filling as $\omega \in [2|E_F|, W]$. The minimal possible absorption energy (orange arrow) and the maximal possible absorption energy (green arrow) is shown for three different fillings. We show quarter-filling in Figure (a), half-filling in Figure (2) and three-quarter-filling in Figure (c). The range of absorption is maximal $\omega \in [\Delta, W]$ for half-filling and decreases for less or greater than half-filling. Unoccupied momentum states that do not contribute for less than half-filling are occupied in both bands for more than half-filling and thus do not contribute either (compare Figure (a) and Figure (c)).

ground state is the α-vacuum in the case of less than or equal to half-filling. We obtain

$$\langle [O(t), O] \rangle_0 = \langle GS | [O(t), O] | GS \rangle \tag{4.115}$$

$$= 2 \sum_{k=-k_F}^{k_F} |C(k)|^2 \left(e^{-2iE_k t} - e^{2iE_k t} \right), \tag{4.116}$$

$$|C(k)|^2 = 4 \sin^2(k) \cos^2(\varphi(k)) \tag{4.117}$$

$$= \frac{(J + J')^2 \sin^2(2k)}{(J^2 + J'^2) + 2JJ' \cos(2k)}, \tag{4.118}$$

where k_F now is the momentum corresponding to the Fermi energy $E_F < 0$ which is negative for less than or equal to half-filling.
The response is given by

$$\overline{\operatorname{Im} \chi_{O,O}(\omega)} = -2\delta \sum_{k}^{k_F} |C(k)|^2 \left(\frac{1}{\delta^2 + (\omega - 2E_k)^2} - \frac{1}{\delta^2 + (\omega + 2E_k)^2} \right) \tag{4.119}$$

$$= -2\pi \sum_{k}^{k_F} |C(k)|^2 \left(\delta(\omega - 2E_k) - \delta(\omega + 2E_k) \right). \tag{4.120}$$

Energy absorption and thus excitations in the system occur at $\omega = 2E_k$. This corresponds to exciting a particle of momentum k and energy $-E_k$ from the β-band to a state in the α-band of momentum $k+\pi$ in the extended zone scheme or momentum k in the reduced zone scheme with energy $+E_k$. The minimal energy that can be absorbed by the system is the gap Δ which corresponds to exciting a particle of momentum $\pi/2$ from the β-band to an empty state in the α-band. This is only possible at half-filling when the β-band is completely occupied and the α-band is completely empty. The maximal energy that can be absorbed by the system is the total bandwidth W which corresponds to exciting a particle of momentum 0 from the β-band to an empty state in the α-band. This transfer is possible for all fillings except zero filling. The minimal possible energy of absorption decreases with increasing filling up to half-filling. The possible particle excitations and thus the minimal and maximal possible absorbed energy is visualized in Figure 4.11.
For more than half-filling all terms in the product $O(t)O$ given by Equations (4.111) to (4.114) need to be taken into account since the ground state (4.110) is no longer the α-vacuum. However, in the sum $O(t)O - OO(t)$ they cancel in such a way that the response for more than half-filling with a positive Fermi energy $E_F > 0$ corresponding to a momentum k_F is exactly the same as for less than half-filling with Fermi energy $E_F < 0$ and same momentum k_F. It it obvious that the response must be identical since those k-values that are unoccupied for less than half-filling now populate both energy states $-E_k$ and $+E_k$ for more than half-filling such that no particle transfer and energy absorption is possible for these k-values in both cases. The response is thus given by Equation (4.120) for all fillings and k_F is the momentum corresponding to either a negative $E_F < 0$ or a positive $E_F > 0$ Fermi energy.
The continuum limit for all fillings for $\omega > 0$ is given by

$$\frac{\overline{\operatorname{Im} \chi_{O,O}(\omega)}}{L} = -2 \frac{|C(\bar{k})|^2}{|g'(\bar{k})|}, \qquad \omega \in [2|E_F|, W], \tag{4.121}$$

where

$$g(k) = \omega - 2E_k, \tag{4.122}$$

$$\bar{k} = \frac{1}{2}\arccos\left(\frac{\omega^2 - 4J^2 - 4J'^2}{8JJ'}\right). \tag{4.123}$$

Note that $2|E_F|$ refers to the absolute value of the Fermi level such that the range of absorption is the same for equal $\pm E_F$ as explained above. The ω-range of absorption increases with increasing k_F since $2|E_F|$ decreases. Inserting $\bar{k}$ given by Equation (4.123) into Equation (4.121), the prefactor and the numerator become

$$|C(\omega, J, J')|^2 = \omega^2\left(-\frac{(J+J')^2}{16J^2J'^2}\right) + \frac{(J+J')^2(J^2+J'^2)}{2J^2J'^2} + \frac{1}{\omega^2}\left(-\frac{(J+J')^2(J^2-J'^2)^2}{J^2J'^2}\right), \tag{4.124}$$

$$|g'(\omega, J, J')| = \frac{4JJ'\sqrt{1 - \frac{(\omega^2 - 4(J^2+J'^2))^2}{64J^2J'^2}}}{\frac{\omega}{2}}. \tag{4.125}$$

The full response function may then be rewritten

$$\frac{\overline{\operatorname{Im}\chi_{O,O}(\omega)}}{L} = -\frac{(J+J')^2}{8JJ'\omega}\sqrt{-\frac{\omega^4 - 8(J^2+J'^2)\omega^2 + 16(J^2-J'^2)^2}{J^2J'^2}}. \tag{4.126}$$

The response for different fillings is shown in Figure 4.12 in comparison to the finite temperature response (see following paragraph). The dependence on the filling is clearly visible. The response sharply drops to zero at $2|E_F|$ which is the minimal absorption energy. For half-filling, where absorption is possible over the entire range $\omega \in [\Delta, W]$, the response steeply drops to zero when approaching $\omega = \Delta$ corresponding to $k = \pi/2$ and at $\omega = W$ corresponding to $k = 0$ because the prefactor $|C(k)|^2$ given by Equation (4.118) equals zero at these k-values. Furthermore, the response is asymmetric, dropping to zero faster in the vicinity of $\omega = \Delta$. The expansion of $|C(k)|^2$ in the vicinity of the critical points $k = 0$ and $k = \pi/2$ explains this asymmetry. In the vicinity of $k = 0$, $|C(k)|^2 = 4k^2 + \mathcal{O}(k^3)$, whereas in the vicinity of $k = \pi/2$, $|C(k)|^2 = 4(J+J')^2/(J-J')^2(k-\pi/2)^2 + \mathcal{O}\left((k-\pi/2)^3\right)$. This translates into an asymmetry in the prefactor $|C(\omega)|^2$ as a function of ω given by Equation (4.124). Expanding the prefactor in the vicinity of the critical points $\omega = \Delta$ and $\omega = W$ shows linear behavior in leading order. However, the slope is different such that the prefactor at $\omega = \Delta$ drops to zero with a steeper slope which reflects the asymmetry in the response. The response itself given by Equation (4.126) shows $\sqrt{\omega}$-dependence in leading order in the vicinity of the critical points, with a steeper slope approaching $\omega = \Delta$.

The finite temperature response At finite temperature the filling is softened around the zero-temperature cut-off $\mu = E_F$ due to thermal fluctuations. The temperature dependence is governed by the Fermi function given by Equation (4.63).
The finite temperature correlation function is given by

$$\langle[O(t), O]\rangle_T = \sum_{k,\sigma}|C_0(k)|^2\left(\langle\beta^\dagger_{k,\sigma}\beta_{k,\sigma}\beta^\dagger_{k,\sigma}\beta_{k,\sigma}\rangle_T + \langle\alpha^\dagger_{k,\sigma}\alpha_{k,\sigma}\alpha^\dagger_{k,\sigma}\alpha_{k,\sigma}\rangle_T\right) \tag{4.127}$$

$$+|C(k)|^2\left(\langle\beta^\dagger_{k,\sigma}\alpha_{k,\sigma}\alpha^\dagger_{k,\sigma}\beta_{k,\sigma}\rangle_T e^{-2iE_kt} + \langle\alpha^\dagger_{k,\sigma}\beta_{k,\sigma}\beta^\dagger_{k,\sigma}\alpha_{k,\sigma}\rangle_T e^{2iE_kt}\right) \tag{4.128}$$

$$-\text{h.c.}. \tag{4.129}$$

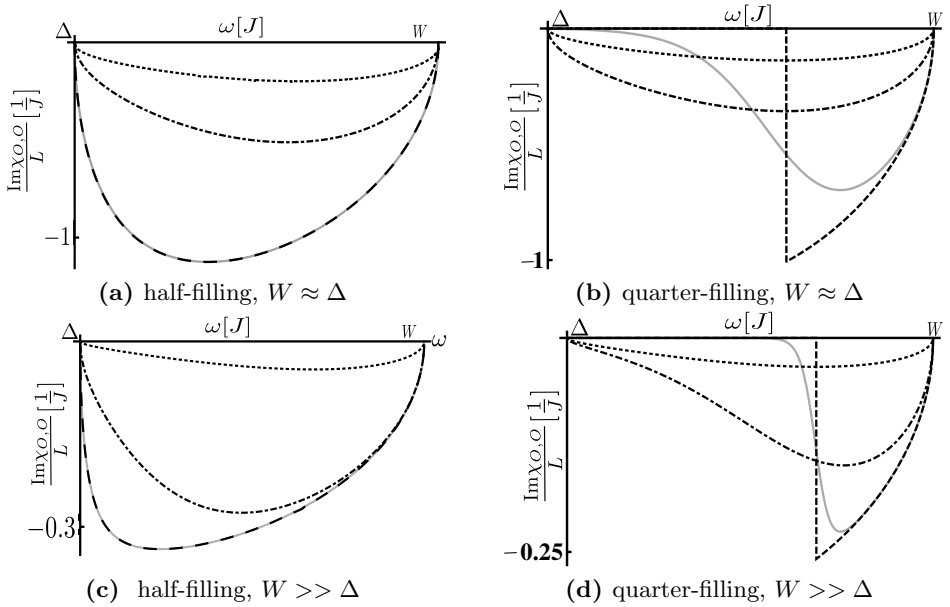

Figure 4.12. – The zero temperature response in comparison to the finite temperature response for different temperatures for two different sets of parameters. In Figures (a) and (b), $J = 1$ and $J' = 2$ such that the gap $\Delta = 2$ is of the order of the total band width $W = 6$. In contrast, in Figure (c) and (d), $J = 5$ and $J' = 6$ such that $\Delta = 2 << W = 22$. In all figures the zero temperature response (long dashed line) is compared to different temperatures: $T = \Delta/10$ (solid gray line), $T = \Delta$ (dot-dashed line) and $T = W$ (dotted line). The Fermi tail is visible the most clearly in Figure (d). Here, $\Delta << W$. At a small temperature of $T = \Delta/10 << W/2$ (solid line) thermal excitations only lead to a smearing out of the particles over a small fraction of the band around quarter filling. Thermal excitations to the second band are suppressed. At larger temperatures (dot-dashed and dotted line) particles get smeared out over the entire band and also excited to the second band. In the case of $\Delta \sim W$, in Figure (b), particles already smear out a lot more around quarter filling for $T = \Delta/10$ since the band is not as broad.

The first two terms cancel with its hermitian conjugate. We need to consider the following finite temperature expectation values

$$\langle \beta^\dagger_{k,\sigma}\alpha_{k,\sigma}\alpha^\dagger_{k,\sigma}\beta_{k,\sigma}\rangle_T = \langle \beta^\dagger_{k,\sigma}\beta_{k,\sigma}\rangle_T^{H_\beta}\langle \alpha_{k,\sigma}\alpha^\dagger_{k,\sigma}\rangle_T^{H_\alpha}, \tag{4.130}$$

$$= f(-E_k-\mu)\left(1-f(E_k-\mu)\right), \tag{4.131}$$

$$\langle \alpha^\dagger_{k,\sigma}\beta_{k,\sigma}\beta^\dagger_{k,\sigma}\alpha_{k,\sigma}\rangle_T = \langle \beta_{k,\sigma}\beta^\dagger_{k,\sigma}\rangle_T^{H_\beta}\langle \alpha^\dagger_{k,\sigma}\alpha_{k,\sigma}\rangle_T^{H_\alpha}, \tag{4.132}$$

$$= \left(1-f(-E_k-\mu)\right) f(E_k-\mu). \tag{4.133}$$

where $\langle\cdot\rangle_T^{H_{\alpha/\beta}}$ denotes the finite temperature expectation value with respect to $H_\alpha = \sum_{k,\sigma}(E_k-\mu)\alpha^\dagger_{k,\sigma}\alpha_{k,\sigma}$ and $H_\beta = \sum_{k,\sigma}(-E_k-\mu)\beta^\dagger_{k,\sigma}\beta_{k,\sigma}$ respectively. The full Hamiltonian given by Equation (4.89) decouples into $H = H_\alpha + H_\beta$. Thus, the decomposition of the expectation value is possible and $\langle \alpha^\dagger_{k,\sigma}\alpha_{k,\sigma}\rangle_T^{H_\alpha} = f(E_k-\mu)$ and $\langle \beta^\dagger_{k,\sigma}\beta_{k,\sigma}\rangle_T^{H_\beta} = f(-E_k-\mu)$. We obtain

$$\langle [O(t),O]\rangle_T = \sum_{k,\sigma}|C(k)|^2\Big\{ f(-E_k-\mu)\left(1-f(E_k-\mu)\right)\left(e^{-2iE_kt}-e^{2iE_kt}\right) \tag{4.134}$$

$$+\left(1-f(-E_k-\mu)\right)f(E_k-\mu)\left(e^{2iE_kt}-e^{-2iE_kt}\right)\Big\} \tag{4.135}$$

$$= 2\sum_k |C(k)|^2 F(k,T,\mu)\left(e^{-2iE_kt}-e^{2iE_kt}\right), \tag{4.136}$$

with the temperature-dependent function

$$F(k,T,\mu) = \left(\frac{e^{\beta E_k}-e^{-\beta E_k}}{e^{-\beta\mu}(e^{\beta\mu}+e^{\beta E_k})(e^{\beta\mu}+e^{-\beta E_k})}\right), \tag{4.137}$$

where $\beta = k_BT$ is the inverse temperature.
Thus, the response function is given by

$$\overline{\mathrm{Im}\,\chi_{O,O}(\omega)} = -2\delta\sum_k |C(k)|^2F(k,T,\mu)\left(\frac{1}{\delta^2+(\omega-2E_k)^2}-\frac{1}{\delta^2+(\omega+2E_k)^2}\right) \tag{4.138}$$

$$= -2\pi\sum_k |C(k)|^2F(k,T,\mu)\Big(\delta(\omega-2E_k))-\delta(\omega+2E_k)\Big). \tag{4.139}$$

In the continuum limit, for $\omega > 0$, we obtain

$$\frac{\overline{\mathrm{Im}\,\chi_{O,O}(\omega,T,\mu)}}{L} = -2\frac{|C(\bar{k})|^2F(\bar{k},T,\mu)}{|g'(\bar{k})|} \tag{4.140}$$

$$= -2\frac{|C(\omega)|^2F(\omega,T,\mu)}{|g'(\omega)|}, \tag{4.141}$$

where $\bar{k}$, $|C(\omega)|^2$ and $|g'(\omega)|$ are given by Equations (4.123), (4.124) and (4.125) respectively and with

$$F(\omega,T,\mu) = \left(\frac{e^{\beta\frac{\omega}{2}}-e^{-\beta\frac{\omega}{2}}}{e^{-\beta\mu}(e^{\beta\mu}+e^{\beta\frac{\omega}{2}})(e^{\beta\mu}+e^{-\beta\frac{\omega}{2}})}\right). \tag{4.142}$$

This function is a combination of Fermi functions which leads to a temperature-dependence in the response. The response for different parameters, fillings and temperatures is shown in Figure 4.12. The Fermi tail is clearly visible away from half-filling

and for small temperatures $T << W/2$ as may be seen in Figure 4.12b and 4.12d. Away from half-filling, for increasing temperatures, the particles smear out over all momenta such that absorption occurs over the entire possible absorption range with a decrease in amplitude. At half-filling (Figure 4.12a and Figure 4.12c) the suppression of the response at $\omega = \Delta$ makes it harder to distinguish the Fermi tail. At small temperatures, the zero temperature response and the finite temperature response coincide and the temperature-dependence does not show. At increasing temperatures the response decreases since particles get thermally excited into the second band. Note that the temperature dependence is more distinct for $W >> \Delta$ (Figure 4.12d) in comparison to $W \approx \Delta$ (Figure 4.12b) where already small temperatures lead to a smearing out over all momenta and thermal excitations into the second band.

The response of the trapped system We determine the one- and three-dimensional in-trap response analogous to the non-dimerized case in Section 4.1.2 within the local density approximation. Remember, that the perturbation is only applied along one direction.
We normalize the trapping strength by the hopping parameter J such that the characteristic densities are given by

$$\rho_{1D} = N\sqrt{\frac{V_t}{J}}, \tag{4.143}$$

$$\rho_{3D} = N\sqrt{\frac{V_t}{J}}^3, \tag{4.144}$$

with $V_t \to \bar{V}_t = (V_{t,x}V_{t,y}V_{t,z})^{1/3}$ in the case of anisotropic confinement in three dimensions.
For the density of the homogeneous system, the total in-trap particle number and the full in-trap response (normalized to the number of particles) in one dimension we obtain

$$n_{1D} = \frac{1}{\pi}\int_{-\pi/2}^{\pi/2}\Big(f(E_k-\mu)+f(-E_k-\mu)\Big)\mathrm{d}k, \tag{4.145}$$

$$N_{1D} = \sqrt{\frac{J}{V_t}}\int_{-\infty}^{\bar{\mu}_0}\mathrm{d}\bar{\mu}\frac{1}{\sqrt{\bar{\mu}_0-\bar{\mu}}}\,n_{1D}(\bar{\mu}\cdot J), \tag{4.146}$$

$$\overline{\mathrm{Im}\,\chi_{O,O}}_{1D} = \frac{1}{N_{1D}}\sqrt{\frac{J}{V_t}}\int_{-\infty}^{\bar{\mu}_0}\mathrm{d}\bar{\mu}\frac{1}{\sqrt{\bar{\mu}_0-\bar{\mu}}}\frac{\mathrm{Im}\,\chi_{O,O}(\bar{\mu}\cdot J)}{L}. \tag{4.147}$$

In three dimensions we obtain

$$\begin{aligned} n_{3D} = \frac{1}{\pi^3}\int_{-\pi/2}^{\pi/2}\int_{-\pi/2}^{\pi/2}\int_{-\pi/2}^{\pi/2}\mathrm{d}k_x\mathrm{d}k_y\mathrm{d}k_z\Big(&f(E_{k_x}+E_{k_y}+E_{k_z}-\mu)+f(E_{k_x}+E_{k_y}-E_{k_z}-\mu),\\ &+f(E_{k_x}-E_{k_y}+E_{k_z}-\mu)+f(E_{k_x}-E_{k_y}-E_{k_z}-\mu)\\ &+f(-E_{k_x}+E_{k_y}+E_{k_z}-\mu)+f(-E_{k_x}+E_{k_y}-E_{k_z}-\mu)\\ &+f(-E_{k_x}-E_{k_y}+E_{k_z}-\mu)+f(-E_{k_x}-E_{k_y}-E_{k_z}-\mu)\Big), \end{aligned} \tag{4.148}$$

$$N_{3D} = 2\pi\left(\frac{J}{V_t}\right)^{3/2}\int_{-\infty}^{\bar{\mu}_0}\mathrm{d}\bar{\mu}\sqrt{\bar{\mu}_0-\bar{\mu}}\,n_{3D}(\bar{\mu}\cdot J), \tag{4.149}$$

$$\overline{\mathrm{Im}\,\chi_{O,O}}_{3D} = \frac{2\pi}{N_{3D}}\left(\frac{J}{V_t}\right)^{3/2}\int_{-\infty}^{\bar{\mu}_0}\mathrm{d}\bar{\mu}\sqrt{\bar{\mu}_0-\bar{\mu}}\frac{\mathrm{Im}\,\chi_{O,O}(\bar{\mu}\cdot J)}{L},. \tag{4.150}$$

In both cases the response of the homogeneous system $\mathrm{Im}\,\chi_{O,O}(\bar{\mu}\cdot t)/L$ is given by Equation (4.141).
We employ the same fitting procedure as in the non-dimerized case (see Section 4.1.2) in the three-dimensional case for temperatures varying from $T = 0.1J$ to $T = J$ and central densities $n_0 < 1$ where the temperature dependence is clearly visible. We use the same parameters as in the non-dimerized case with the additional parameter $J' = 1.1J$ such that the gap is much smaller than the total band width. We also have to be aware of collective in-trap modes that may be excited at certain perturbing frequencies as explained in detail in Section 4.1.2. The fitting procedure works well

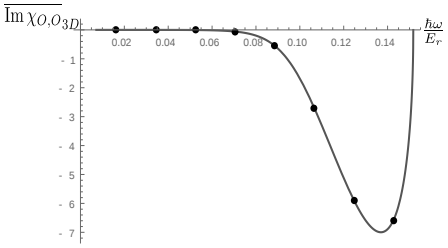

(a) central density $n_0 = 0.65$

Figure 4.13. – The total in trap response $\overline{\mathrm{Im}\,\chi_{O,O}}_{3D}$ of the three-dimensional system for 8 data points and the fit of the full function to these data points for $T = 0.1J$. The fit function is the full response given by (4.150) including a constant prefactor. Fit parameters are the prefactor, the temperature T and the central chemical potential μ_0

for all considered temperatures up to central densities of $n_{0,3D} = 1$. For the highest temperature of the order of the hopping strength $T = J$ we obtain the exact values for the fitting parameters down to central densities $n_{0,3D} \sim 0.1$. The lower bound increases for decreasing temperatures. However, fitting works down to central densities of $n_{0,3D} \sim 0.4$ for the lowest temperature $T = 0.1J$. In Figure 4.13 the data points are compared to the response given by Equation (4.150) for a prefactor, a temperature and a central chemical potential obtained from the fit.
Note one major advantage of the dimerized equilibrium lattice compared to the non-dimerized case from the preceding section. We excite to the second band which is crucial in order to reliably determine the absorbed energy from measurements of the quasimomentum occupation $\langle n_k(t)\rangle$ by adiabatic band mapping. We will discuss this in more detail in Section 4.4.2.

4.3. Beyond tight-binding

We extend our study of the non-dimerized equilibrium lattice beyond tight-binding. We include higher bands into the theory that may be excited by perturbing at higher frequencies. Our motivation to do so is twofold. In the first place, the measurement process is considerably simplified in comparison to the one-band model. We comment on the measurement process and its advantages in detail in Section 4.4.2. Secondly, we avoid exciting in-trap modes which lie in the order of magnitude of the lowest band as explained in Section 4.1.2. We compute and discuss the response of the system to perturbations at higher frequencies for a certain lattice setup in the following Section 4.4 on the experimental realization. Here, we merely introduce the underlying theoretical formulas.
We start by writing the Hamiltonian in second quantized form in the Bloch basis. A

particle in a periodic potential $V_0(x)$ is described by the Schrödinger equation

$$H_1\phi_{nk}(x) = E_n(k)\phi_{nk}(x), \tag{4.151}$$

$$H_1 = \frac{\hat{p}^2}{2m} + V_0(x), \tag{4.152}$$

where the eigenfunctions $\phi_{nk}(x)$ are called the Bloch wave functions of fixed quasimomentum k. The Bloch function is delocalized over the entire lattice. It can be written as the product of a plane wave with a periodic function

$$\phi_{nk}(x) = e^{ikx} \cdot u_{nk}(x), \tag{4.153}$$

where $u_{nk}(x)$ has the same periodicity as the lattice potential. The eigenenergies $E_n(k)$ are the eigenvalues corresponding to the Bloch function $\phi_{nk}(x)$ and n denotes the band index. We denote the lowest band $n = 1$. We represent the orthonormal Bloch basis by $|n, k\rangle$.
The Hamiltonian in second quantized form can then be written as

$$H = \sum_{nkn'k'} \langle n'k'|H_1|nk\rangle c^\dagger_{n'k'}c_{nk} \tag{4.154}$$

$$= \sum_{nk} E_n(k)c^\dagger_{nk}c_{nk}. \tag{4.155}$$

It is diagonal in quasimomentum space. We deal with a time time-dependent optical lattice $V(x,t) = V_0(x) + h\sin(\omega t)\tilde{V}(x)$ as introduced in Section 1.3 such that the time-dependent part of the Hamiltonian becomes

$$h\sin(\omega t)O, \tag{4.156}$$

$$O = \sum_{nkn'k'} \langle n'k'|\tilde{V}(x)|nk\rangle c^\dagger_{n'k'}c_{nk}. \tag{4.157}$$

We define the transition matrix element

$$M_{nk\to n'k'} = \langle n'k'|\tilde{V}(x)|nk\rangle \tag{4.158}$$

$$= \int_{x_{min}}^{x_{max}} \mathrm{d}x\phi^*_{n'k'}(x)\tilde{V}(x)\phi_{nk}(x), \tag{4.159}$$

where the integral is taken over the entire length of the lattice with L lattice sites and lattice spacing a such that $x_{\min} = -(L/2+1)a$ and $x_{\max} = La/2$. The absolute value squared $|M_{nk\to n'k'}|^2$ of the transition matrix element gives the probability that a particle in Bloch state $|nk\rangle$ is transferred to the Bloch state $|n'k'\rangle$ by the perturbation $\tilde{V}(x)$. The full time-dependent Hamiltonian in the Bloch basis is thus given by

$$H = \sum_{nk} E_n(k)c^\dagger_{nk}c_{nk} + h\sin(\omega t)\sum_{nkn'k'} M_{nk\to n'k'}c^\dagger_{n'k'}c_{nk}. \tag{4.160}$$

We determine $E_n(k)$ and $\phi_{nk}(x)$ by numeric band structure calculations and deduce the transfer matrix elements in Bloch basis for a certain optical lattice setup in the following Section 4.4 on the experimental realization.
We compute the response function in the Bloch basis representation. We use the spectral representation given by Equation (2.14),

$$\mathrm{Im}\chi_{OO^\dagger}(\omega) = -\frac{\pi}{Z}\sum_{n,m} |\langle m|O|n\rangle|^2 e^{-\beta(E_n-\mu N)}\delta\left(\omega - (E_m - E_n)\right)\left(1 - e^{-\beta\omega}\right). \tag{4.161}$$

Here, the many body states $|n\rangle$ are given by $|n\rangle = \prod_{\{k\}} c_k^\dagger |0\rangle$ where $|0\rangle$ is the vacuum and $c_k^\dagger$ creates a particle in Bloch state k. The product runs over all possible configurations of different k denoted by $\{k\}$. We insert the perturbing operator O in Bloch basis given by Equation (4.157). For the lowest band we obtain

$$\mathrm{Im}\chi_{OO^\dagger}(\omega) = -4\delta \sum_{k,k'} |M_{k\to k'}|^2 \Big(f\big(E(k)-\mu\big) - f\big(E(k')-\mu\big)\Big) \cdot \tag{4.162}$$

$$\cdot \frac{1}{\delta^2 + \big(\omega - (E(k') - E(k))\big)^2} \cdot \tag{4.163}$$

The above calculation is carried out in Appendix C. Note that a direct comparison of the response in Bloch basis within the lowest band and $k' = \pi$ to the response in tight-binding from Section 4.1.2 is possible. If this is not clear to the reader we refer to Appendix D where we show equivalence of the transfer matrix elements in Bloch and in Wannier basis. We carry out the direct comparison for a certain lattice setup in Section 4.4.3 to show that tight-binding is a good approximation. For excitations to higher bands we obtain

$$\mathrm{Im}\chi_{OO^\dagger}(\omega) = -\delta \sum_{k} |M_{n=1,k\to n'\neq 1,k'}|^2 \Big(f\big(E_1(k)-\mu\big) - f\big(E_{n'}(k')-\mu\big)\Big) \cdot \tag{4.164}$$

$$\cdot \frac{1}{\delta^2 + \big(\omega - (E_{n'}(k') - E_1(k))\big)^2} \cdot \tag{4.165}$$

4.4. The experimental approach

In this section we discuss the precise experimental situation in more detail. In Section 4.4.1 we introduce a particular optical lattice setup and we comment on the measurement process in 4.4.2. In Section 4.4.3 we show that the tight-binding approximation is valid for this particular setup. In Section 4.4.4 we extend our study of the system's response to an external perturbation at higher frequencies such that excitations to higher bands occur. In this case we deduce a simple Hamiltonian of similar form to the single-band tight-binding Hamiltonian.

4.4.1. The experimental setup

Here, we exemplify a realization of the non-dimerized equilibrium lattice superimposed with a superlattice perturbation. We use the parameters from Reference [21]. An optical lattice is created by superimposing a green laser of wavelength $\lambda_g = 532\mathrm{nm}$ with its own retro-reflection. The wells of the emergent standing wave are separated by a distance $\lambda_g/2 = \pi/k_g$ where $k_g = 2\pi/\lambda_g$ is the wave number of the green laser wave. The green lattice is what we will call the equilibrium lattice. Note the relation to tight-binding from Section 4.1 where we set the lattice spacing $a \equiv 1$ which leads to a first Brillouin zone of size 2π. Here, we have $a = \pi/k_g$ such that the first Brillouin zone is of size $2k_g$. A momentum transfer of $\Delta k = \pi$ in the tight-binding picture is thus equivalent to a momentum transfer of $\Delta k = k_g$ in the optical lattice picture. In the following we will use both notations for Δk equivalently. The lattice is loaded with a degenerate gas of fermionic ^{40}K atoms. An infra-red laser of wavelength $\lambda_r = 1064\mathrm{nm}$ and wave number $k_r = 2\pi/\lambda_r$ and its retro-reflection are added to create a bichromatic superlattice. The frequencies of the two lasers differ by a factor of two, up to a small detuning $\delta\nu$. The detuning may be adjusted in such a way that the superlattice has a constant bottom

offset. The red laser is modulated by an electro-optic modulator which leads to a time-dependent modulation of the superlattice. The modulation can be chosen in such a way, that the superlattice oscillates around the equilibrium configuration of the green lattice as shown in Figure 4.14. We choose a time-dependence of the form $\sin(\omega t)$ with a

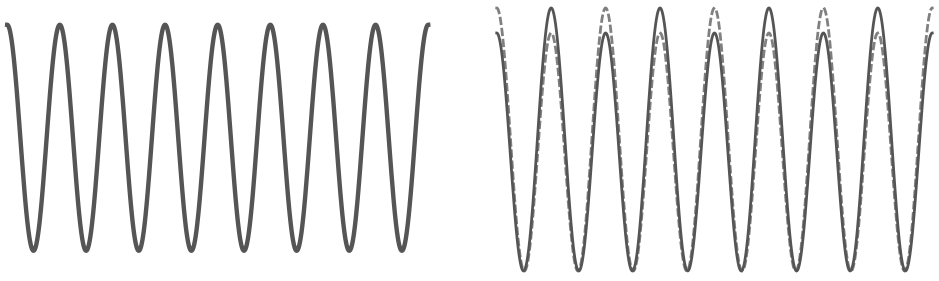

(a) green equilibrium lattice **(b)** superlattice modulation

Figure 4.14. – The superlattice modulation (b) oscillates around the equilibrium lattice (a) between the configurations indicated by solid and dashed lines. The amplitude of the modulation h is small with respect to the equilibrium lattice and the oscillation frequency is given by ω.

small amplitude h such that the superlattice modulation is a small perturbation to the green equilibrium lattice. The modulation frequency $\omega \sim 10^3$Hz is much smaller than the laser frequency $\omega_g \sim 10^{15}$Hz such that the perturbation does not excite electronic levels of the atoms. The full time-dependent optical lattice potential is given by

$$V(x) = V_0(x) + h\sin(\omega t)\tilde{V}(x), \tag{4.166}$$

$$V_0(x) = V_g\cos^2(k_g x) - \frac{V_g}{2}, \tag{4.167}$$

$$\tilde{V}(x) = \cos(k_g x), \tag{4.168}$$

where the lattice depth of the green lattice is chosen to be $V_g = 40E_r^{\mathrm{red}}$. It is given in units of the recoil energy of the red laser $E_r^{\mathrm{red}} = \hbar^2 k_r^2/2m = \hbar^2 k_g^2/8m = E_r^{\mathrm{green}}/4$ with the mass of ^{40}K atoms, $m = 39.96u$, $u = 1.660539 \cdot 10^{-27}$kg.

4.4.2. The measurement

As explained in Section 4.1.2 we expect to observe a linear rise in the energy absorbed by the system $E(t)$ as a function of the duration t of the perturbation. We employ linear response theory in Section 4.1 to compute the response function $Im\chi_{OO^\dagger}(\omega)$ within the lowest Bloch band. We establish the following relation to the slope m of $E(t)$ (Equation (4.39)),

$$Im\chi_{OO^\dagger}(\omega) = \frac{-2m}{|h|^2\omega}. \tag{4.169}$$

We have to carry out the measurement for different values of ω within the range of absorption $\omega \in (0, 4J]$, where J is the hopping amplitude (see Section 4.1 for details) to map out the full response function within the lowest Bloch band. In standard lattice shaking experiments with bosonic atoms the energy absorbed by the system is usually estimated from the broadening of the central peak of the momentum distribution measured in a time-of-flight absorption image after sudden switch off [14], see Section 1.3. More recently, single-site atom resolved detection has been employed to estimate

the absorbed energy by an increase in fluctuations [16]. In fermionic lattice shaking experiments the energy absorption may be quantified by the observation of the double occupancy induced by a periodic modulation [54]. Here, we take advantage of the k-selectivity of our perturbation. Each modulation frequency ω ideally only addresses a single momentum $|k|$ and $|k+\pi|$ on resonance. Assuming the case where momentum k is initially occupied and $k+\pi$ unoccupied. The absorbed energy is then given by

$$E(t) = \hbar\omega\langle n_{k+\pi}(t)\rangle, \tag{4.170}$$

where $\langle n_{k+\pi}(t)\rangle$ is the occupation of the momentum state $k+\pi$. Note that $\langle n_k(t)\rangle + \langle n_{k+\pi}(t)\rangle = 1$. This is experimentally appealing because the quasimomentum distribution may be measured fairly easily by adiabatic band mapping, see Section 1.3. Applying adiabatic band mapping after a certain duration t of the perturbation directly gives access to the quasimomentum distribution $\langle n_k(t)\rangle$ and thus to the energy absorbed by the system.
There is a little drawback concerning the above scheme. When exciting within the lowest band, excitations will not be clearly separated from the initial distribution in the absorption image such that it will be difficult to reveal the time-dependence of $\langle n_k(t)\rangle$ within a single band. However, this is why the dimerized equilibrium lattice discussed in Section 4.2 is an appealing setup since we do not encounter this problem. In the dimerized case, the size of the Brillouin zone is divided in half due to the doubling of the unit cell. Its length is reduced to π such that a momentum kick of π transfers particles to the next Brillouin zone and to the second band accordingly. Absorption imaging here gives access to the number of particles in the second band as they appear in the second Brillouin zone. In particular, as the perturbing frequency ω is fixed and ideally only addresses a certain momentum k, we directly image the corresponding occupation after a certain duration t of the perturbation, $\langle n_k(t)\rangle$. Consequently, measuring the absorbed energy wraps up to counting all particles in the second Brillouin zone which is initially unoccupied such that excitations are clearly separated from the initial distribution in the first Brillouin zone. We want to recover this simple measurement scheme for the non-dimerized equilibrium lattice. We succeed in doing so by considering its higher bands in Section 4.4.4. We deduce a tight-binding approach leading to a measurement equivalent to the dimerized situation. Excitations to higher bands have other advantages. Excitation frequencies are higher such that we avoid exciting in-trap modes which lie within order of magnitude of the lowest band (see Section 4.1.2).
Note that this measurement scheme also applies to the exact time dependence discussed in Section 4.1.1.

4.4.3. Verification of tight-binding

We verify that the tight-binding approximation is a good approximation in the case of this particular lattice setup of the form $V(x) = V_0(x) + h\sin(\omega t)\tilde{V}(x)$. In order to do so, we first compute the transfer matrix elements in Bloch basis (see Section 4.3) showing that the perturbation $\tilde{V}$ indeed couples, to a good approximation, only momentum states k and $k+k_g$ of the green equilibrium lattice. Remember that $k = k_g$ in the optical lattice picture corresponds to $k = \pi$ in the tight-binding picture. Note that this k-selectivity of the transfer matrix elements is not clear a priori. We then compute the corresponding response in Bloch basis and compare to the theory result in tight-binding.
We start by computing the transfer matrix elements for all Bloch states of the lowest

band, $M_{n=1,k\to n=1,k'} \equiv M_{k\to k'}$, given by Equation (4.158). The Bloch functions $\phi_{nk}(x)$ and the eigenenergies $E_n(k)$ are determined by numeric band structure calculations, see Appendix B, for the equilibrium lattice potential $V_0(x) = V_g \cos^2(k_g x) - V_g/2$ with the parameters introduced in 4.4.1. We find the following order of magnitude

$$M_{k\to k'} = \begin{cases} \mathcal{O}\left(10^{-12} - 10^{-8}\right), k' \neq k + k_g \\ \mathcal{O}\left(10^{-5} - 10^{-4}\right), k' = k + k_g, k \neq \{0, k_g\} \\ \mathcal{O}(10^{-23}), k' = k + k_g, k = \{0, k_g\} \end{cases} . \tag{4.171}$$

We conclude that all transfer matrix elements with $k' \neq k + k_g$ are strongly suppressed in comparison to transfers with $\Delta k = k_g$ which promotes the tight-binding approximation made. Exceptions are the $\Delta k = k_g$-matrix elements for $k = \{0, k_g\}$ which are even more strongly suppressed. This corresponds to the prohibited transfer of the bandwidth $\omega = 4J$ observed in tight-binding.
However, we still need to verify that the matrix elements for $k' \neq k + k_g$ do not contribute in the sum of the response function. We will do so in the following. We employ two different comparisons in order to show that tight-binding is a good approximation. To begin with, we compare the above result considering all Δk to the response which only includes transfer matrix elements with $\Delta k = k_g$. We verify that the matrix elements $M_{k\to k'\neq k+k_g}$ hardly contribute to the response as was already hinted at by their suppressed order of magnitude. The comparison gives good results for different fillings (n very small up to $n = 1$) and temperatures $T \in (0.01W, W)$ where $W = E(k = k_g) - E(k = 0) = 9 \cdot 10^{-31}$Joule is the bandwidth for parameters from Section 4.4.1. One example is shown in Figure 4.15a. We choose filling $n = 0.5$ and $T = 0.01W$.

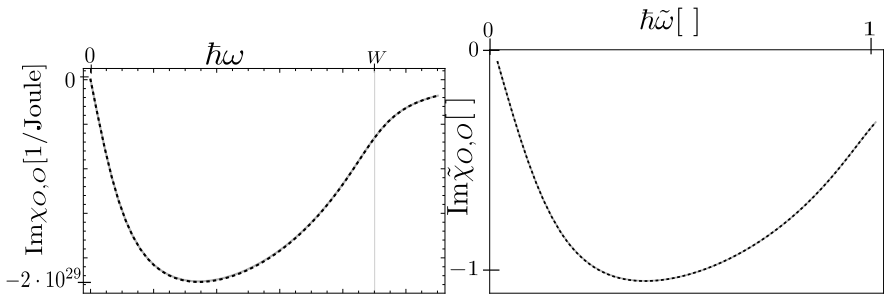

(a) The response in Bloch basis **(b)** The response in Bloch basis compared to tight-binding

Figure 4.15. – In (a) we compare the finite size response in the Bloch basis considering only transfers with $\Delta k = k_g$ (solid line) to the response in Bloch basis considering all matrix elements with Δk arbitrary (dotted line). We compute the response for $L = 100$ lattice sites at half-filling $n = 0.5$ and at a temperature $T = 0.01W$. We use the optical lattice parameters from Section 4.4.1 and eigenenergies and Bloch functions from the corresponding band structure calculation in Appendix B such that the bandwidth is given by $W = E(k = k_g) - E(k = 0) = 9 \cdot 10^{-31}$Joule. In (b) we compare the finite size response in the Bloch basis considering only transfers with $\Delta k = k_g$ (solid line) to the tight-binding response (dotted line). We choose $L = 100$ and filling $n = 0.5$. We normalize all energy units by the bandwidth $W = 4J = 4$ in the tight-binding case and $W = E(k = k_g) - E(k = 0)$ in the Bloch case for parameters from Section 4.4.1 and rescale the response by its value at $\hbar\tilde{\omega} = \hbar\omega/W = 0.5$. We use the rescaled temperature $\tilde{T} = 0.025$. In both cases, (a) and (b), we observe very good agreement which verifies the tight-binding approximation (see main text).

Secondly, we compare the response for $k' = k + k_g$ to the tight-binding result given by

Equation (4.66). In order to do so we first normalize each energy unit by the bandwidth W which is $4J$ in the case of tight-binding and given by $E_{n=1}(k = k_g) - E_{n=1}(k = 0)$ in the Bloch basis case such that the response functions only depend on dimensionless parameters. We then rescale by the response at $\hbar\tilde{\omega} = \hbar\omega/W = 0.5$ and compare for different fillings and temperatures. The comparison shows excellent agreement for different fillings and temperatures as above. One example for $n = 0.5$ and $\tilde{T} = T/W = 0.025$ is shown in Figure 4.15b.

4.4.4. Higher band excitations

We now take higher bands of the non-dimerized equilibrium lattice into consideration. The measurement of a change in the quasimomentum occupancy $\langle n_k(t)\rangle$ within the lowest band requires a very high resolution of the absorption imaging as commented on in Section 4.4.2. This is challenging in experiment. In the dimerized lattice we do not encounter this problem as explained in Section 4.4.2 and measuring the absorbed energy wraps up to counting all particles in the second Brillouin zone. We also want to benefit from this simple measurement scheme for the non-dimerized equilibrium tight-binding lattice. We show that we obtain an analogous situation for excitations to the third band where measuring the absorbed energy wraps up to counting all particles in the third Brillouin zone.
A schematic representation of the band structure obtained in Appendix B is shown in Figure 4.16. We choose a higher perturbing frequency ω exciting to the third band but remaining well below the atomic resonance frequency. The third band is roughly parallel to the first (lowest) band. Excitations with $\Delta k = k_g$ thus correspond to a certain ω for each k as sketched in Figure 4.16 and we recover an equivalent measurement scheme to the dimerized equilibrium lattice. Note, that the second band is not as suitable for this kind of measurement as $E_1(k)$ and $E_2(k + k_g)$ may be roughly parallel. If this is the case our perturbation would no longer be k-selective. All k would get excited by approximately equal ω such that the response function would not be resolved in energy.

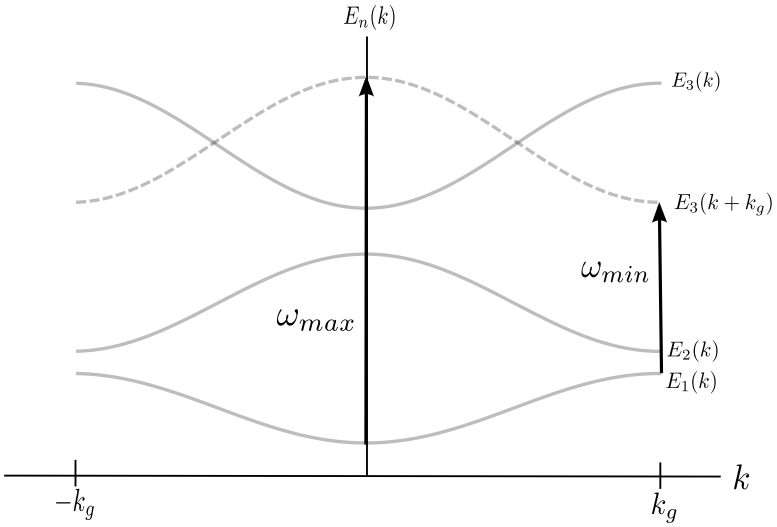

Figure 4.16. – The band structure of the lattice potential $V_0(x) = V_g \cos^2(k_g x) - V_g/2$. Excitations to the third band are k-selective and enable a simple measurement scheme of the occupation $\langle n_k(t)\rangle$ (see main text).

Note an important advantage with respect to the prior case dealing with excitations within the lowest Bloch band only. Excitation energies to the third band are higher such that we avoid exciting collective in-trap modes (see Section 4.1.2) that would render the treatment invalid at certain frequencies. These frequencies lie within the band width of the lowest band and below our range of absorption for excitations to the third band. Hence, we can map out the response function over the entire range of absorption.
However, it remains to verify that our perturbation, to a good approximation, only excites particles to the third band with a momentum kick of $\Delta k = k_g$ such that the response is resolved in energy. We do this by computing the transfer matrix elements from the first to the third band $M_{n=1,k\to n'=3,k'}$ given by Equation 4.158. This computation is analogous to Section 4.4.3 where we compute the transfer matrix elements within the lowest Bloch band. We use the Bloch functions and eigenenergies for the optical lattice from Section 4.4.1 obtained by numeric band structure calculations in Appendix B. We find that the result agrees with our expectation of k-selectivity. All matrix elements with $k' \neq k + k_g$ are strongly suppressed compared to those with $k' = k + k_g$. Just as for the lowest band $k = 0$ and $k = k_g$ are an exception. These transfers are suppressed for arbitrary Δk.

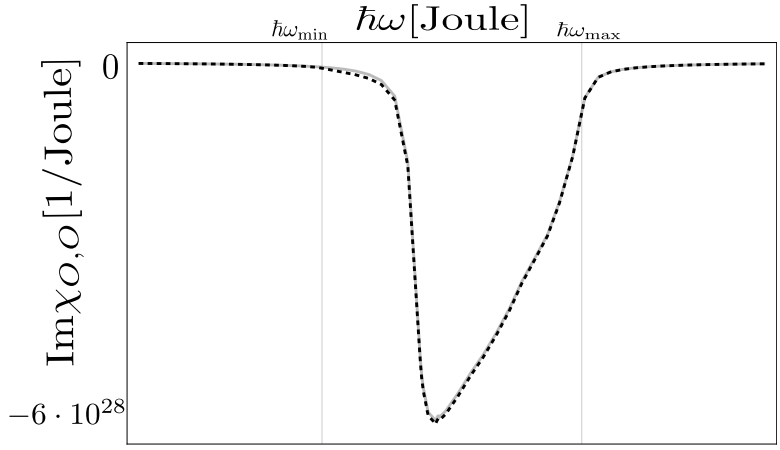

Figure 4.17. – We compare the finite size response for excitations from the lowest band $n = 1$ to the third band $n = 3$ in the Bloch basis considering only transfers with $\Delta k = k_g$ (solid line) to the response in Bloch basis considering all matrix elements with Δk arbitrary (dotted line). We use the results of the band structure calculation in Appendix B and use the following parameters $L = 100$, half-filling $n = 0.5$, $T = 0.01W$, bandwidth of the lowest band $W = E_1(k = k_g) - E_1(k = 0) = 9.0{\cdot}10^{-31}$Joule. The possible range of absorption lies in between $\hbar\omega_{\min} = E_3(0) - E_1(k_g) = 9.0 \cdot 10^{-29}$Joule and $\hbar\omega_{\max} = E_3(k_g) - E_1(0) = 1.3 \cdot 10^{-28}$Joule. Absorption is not observed over the entire range as the lowest band is only half-filled. Note that this in in contrast to the response within the lowest band where half-filling leads to excitations over the entire possible range of absorption (see main text).

We compute the corresponding response function in Bloch basis given by Equation (4.164) where we set $n' = 3$. We consider two different cases. On the one hand, the response including all matrix elements for arbitrary Δk. On the other hand, the response only including matrix elements with $\Delta k = k_g$. We show that only matrix elements for $\Delta k = k_g$ significantly contribute to the response such that we can write down a simple k-selective Hamiltonian for this scheme similar to the tight-binding case restricted to the lowest band. The response for all Δk and $\Delta k = k_g$ in comparison is shown in Figure 4.17 for the case $n = 0.5$ and $T = 0.01W$ with bandwidth

$W = E(k = k_g) - E(k = 0) = 9.0 \cdot 10^{-31}$Joule. Both curves sufficiently coincide such that a 'tight-binding'-like treatment is also valid for higher bands. We checked that both functions coincide for different fillings (between empty and completely filled) and different temperatures within $T = 0.01W$ and $T = W$.
Note an important difference to the response of the prior case within the lowest Bloch band shown in Figure 4.15. The dependence on the filling is different. Here, the range of absorption lies within $\hbar\omega_{\min} = E_3(0) - E_1(k_g) = 9.0 \cdot 10^{-29}$Joule and $\hbar\omega_{\max} = E_3(k_g) - E_1(0) = 1.3 \cdot 10^{-28}$Joule as is clear from Figure 4.16. The response will only be finite over the full range if the lowest band is completely filled in contrast to the prior case where the full range was covered at half-filling. The response at half-filling is shown in Figure 4.17 and obviously does not cover the maximal possible range of absorption.
We can now write down a 'tight-binding'-like Hamiltonian for a perturbation exciting to the third band,

$$H = \sum_{n=1,3;k} E_n(k) c^\dagger_{nk} c_{nk} + h \sin(\omega t) \sum_k M_{n=1,k\to n=3,k+k_g} c^\dagger_{n=3,k+k_g} c_{n=1,k}, \qquad (4.172)$$

assuming that the third band is initially unoccupied.
Note different behavior of the prefactor in the response in comparison to tight-binding restricted to the lowest band. In tight-binding, the prefactor of the response is found to be of the form $\sim \sin^2(k)$ and numeric band structure calculations yield the same shape for $|M_{n=1,k\to n=1,k+k_g}|^2$ as shown in Figure 4.18. Here, the prefactor is proportional to $|M_{n=1,k\to n=3,k+k_g}|^2$ which is no longer $\sin^2(k)$-shape but also suppresses transfers at $k = 0$ and $k = k + k_g$ as shown in Figure 4.18. We emphasize the analogy between

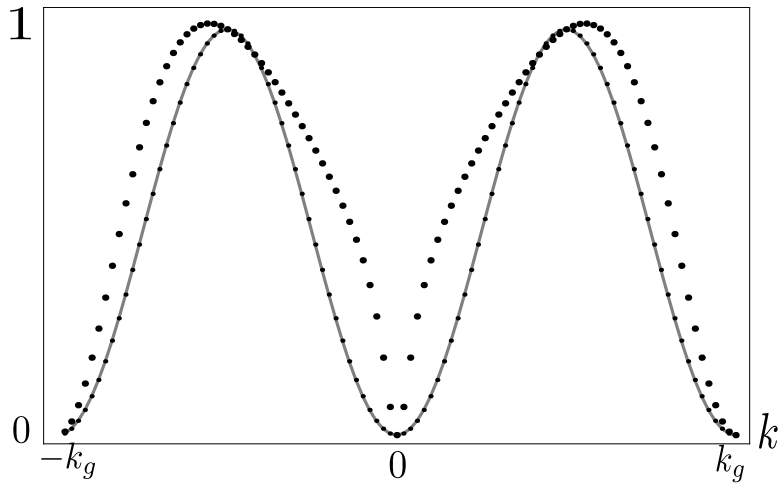

Figure 4.18. – The prefactor of the response for the different considered cases in comparison. The prefactor for the tight-binding case restricted to the lowest band (solid line) is given by $\sin^2(k)$. The prefactor for the response in Bloch basis restricted to the lowest band (dotted line of small point size) is given by $|M_{n=1,k\to n=1,k+k_g}|^2$. We normalize by $|M_{n=1,k=k_g/2\to n=1,k+k_g}|^2$. It perfectly coincides with the $\sin^2(k)$-dependence found in tight-binding. The prefactor for the response in Bloch basis exciting to the third band (dotted line of large point size) is given by $|M_{n=1,k\to n=3,k+k_g}|^2$. We normalize by $|M_{n=1,k=k_g/2\to n=3,k+k_g}|^2$. It does not coincide with the $\sin^2(k)$-dependence but also suppresses excitations at $k = 0$ and $k = k_g$.

this measurement scheme including higher bands and the simple tight-binding case restricted to the lowest band in Section 4.1.2. The response shows a clear signature

of the temperature-dependent Fermi tail due to the k-selectivity of the perturbation. We expect that the same fitting procedure as in the tight-binding case in Section 4.1.2 can be applied in order to extract the temperature from the fit with a minimum of fitting parameters. Note, that we profit from a considerably simpler measurement scheme here compared to tight-binding as measuring the absorbed energy basically wraps up to counting the number of particles in the third Brillouin zone in a time-of-flight absorption image after adiabatically turning off the lattice potential. Repeating this measurement for different energies within the range of absorption $\hbar\omega \in (E_3(0) - E_1(k_g), E_3(k_g) - E_1(0))$ maps out the full response function. We can directly extract the temperature without the input of theoretical modeling.

Discussion We conclude, that the simplicity in both, theory and experiment, clearly outruns other attempts to measure the temperature in fermionic gases trapped in a lattice. One example is a temperature measurement based on measuring the double occupancy [45] in the lattice. From the experimental side, a combination of radio-frequency spectroscopy, Stern-Gerlach separation of the spin components and absorption imaging is needed. Moreover, a full theoretical understanding of the dependence of the number of doubly occupied sites with temperature is required and numerical methods have to be employed. The combination of all this is quite demanding to implement. It is also limited to temperatures above the on-site interaction strength such that thermal fluctuations induce double occupancy. There is other theoretical proposals. One possible concept is a temperature measurement based on the fluctuation-dissipation theorem for non-uniform systems combined with a spatially resolved density and its fluctuations [55]. However, very good local resolution is required for measurements which has not been attained in fermionic experiments yet. Alternatively, a temperature measurement based on Raman spectroscopy has been proposed [56], transferring a portion of the atoms stored in the lattice to a third hyperfine state. This somewhat resembles our concept as excitations occur with fixed energy and momentum such that the Raman transition rate depends on temperature only through the Fermi function. However, from the experimental side an additional Raman laser is needed. Finally, measuring the light intensity after diffraction of light from regular arrays of atoms in an optical lattice was proposed to determine the system's temperature resembling the method of x-ray diffraction from crystalline materials [57]. The diffraction pattern from elastic scattering is insensitive to thermal atomic correlations but inelastic scattering events carry information thermal fluctuations which they separate by blocking elastic scattering events. However, this proposal depends on sufficiently large density fluctuations such that it is not practical in the low temperature regime of interest.

Chapter 5.

Summary and outlook

Research in the field of strongly correlated many-body systems has been in the focus of cold atom experiments for more than a decade and fast progress in both, theory and experiment, has enabled us to develop a deeper knowledge of these systems. However, our understanding is far from being complete. In this work we have studied the influence of a periodic superlattice modulation onto both, bosonic and fermionic atoms, trapped in an optical lattice, pursuing the objective to gain a deeper understanding and new insights into the underlying physics. This work constitutes yet a further building stone in genuinely characterizing strongly correlated quantum systems. We have studied the nature of excitations that exhibit interesting properties due to a distinct characteristic of the superlattice modulation. It injects momentum π into the system which strongly affects the underlying physics. Besides a theoretical analysis, we have exploited the possible experimental applications that we can deduce, motivated by the fact that our ability to probe these systems is still very limited. In particular, we have developed a new scheme to measure the temperature of ultracold fermions trapped in an optical lattice.

Modulation spectroscopy of ultracold bosons in optical lattices In the first part of this project, in Chapter 3, we study bosonic particles in a one-dimensional optical lattice at commensurate filling in the Mott-insulating regime subjected to a periodic superlattice modulation. We consider low-lying excitations in a perturbative approach at strong coupling, comparing this to a numerical study employing the time-adaptive density matrix renormalization group method. We study the lowest peak in the absorption spectrum and find that energy is absorbed within a narrow range around a maximum near the on-site interaction strength which corresponds to the energy needed to create an excitation. The reduced width compared to standard lattice shaking setups [17] is a characteristic of the superlattice modulation which creates a particle-hole pair of center of mass momentum π whose lowest excited energy band is particularly narrow. This is appealing for experimental applications. The position of the spectral response may be used to calibrate the lattice depth [21] such that our setup gives a more accurate measure. At weaker interactions approaching the phase transition, a numerical analysis shows a broadening and a shift to higher energies of the spectral response and we expect to gain interesting insights into the rich physics in future studies.

Thermometry of fermions in optical lattices by modulation spectroscopy In the second part of this project, in Chapter 4, we study non-interacting fermions in a three-dimensional optical lattice with an additional external trapping potential subjected to a periodic superlattice modulation along one direction. We show how a clear signature of the Fermi tail appears in the spectral response. Again, this is a consequence of the superlattice modulation which only couples selectively if $\Delta k = \pi$ such that the thermally softened Fermi surface becomes resolved in energy. As a result the temperature can be

reliably extracted down to remarkably low temperatures well below the Néel temperature where antiferromagnetic ordering is expected to occur. These temperatures have not been reached in experiment so far which remains one of the major goals in current experiments. Our scheme clearly outruns other attempts to measure the temperature in fermionic gases trapped in a lattice due to its simplicity in both, theory and experiment, and its validity down to ultra low temperatures. We developed a scheme how to directly measure the spectral response by adiabatic band mapping when including higher bands where the excited states are clearly separated from the initial distribution and taking advantage of the fact that each perturbing frequency only addresses a certain momentum state. This is a major advance as accurate probes for the absorbed energy in fermionic lattice systems are severely limited. We verify that this implementation is possible for a certain lattice setup available in the lab such that we go beyond pure theoretical reasoning. We are hoping to witness experimental implementation in the near future as the status quo of experiments permits this. Prospectively, it may be of interest to incorporate the influence of interactions which will make theory more complicated but should not degrade the basic idea of the measurement scheme.

Outlook Quite generally, one may envisage several routes how to study intriguing physics taking advantage of the periodic superlattice modulation. For example, it could be exploited to gain insight into more complex lattice models such as the ionic or extended Hubbard model which are expected to exhibit a so-called bond-ordered wave-phase of long-range order in a narrow region between a charge density wave phase and a spin density wave phase [58–61] as the order parameter of the bond ordered phase $\sum_{j,\sigma}(-1)^j\langle c^\dagger_{j,\sigma}c_{j+1,\sigma} + \text{h.c.}\rangle$ is essentially the expectation value of what we call the superlattice operator. Furthermore, we may also generalize our perturbation to arbitrary wave numbers of the additional laser beam such that the dimerization $(-1)^j$ is replaced by $\cos(Kj)$ and the momentum kick introduced by the lattice is now of arbitrary value K which may serve to study the properties of various other quantum phases.

Appendix A.

Numerical convergence and error analysis

In this Appendix we carry out a detailed analysis of numerical convergence of the energy absorbed by a single site $E_j(t)$ determined by a time-dependent density matrix renormalization group study in Section 3.2. We exemplify this for two cases, one at strong coupling $U/J = 20$ and one at weak coupling $U/J = 4$. For these two cases we also give the errors on the energy absorption rate defined in Section 3.2.1.

Numerical convergence For each interaction strength U/J and system length L we ensure that the observable $E_j(t)$ numerically converges within a certain total time in a sense defined in the following. We vary the Hilbert-space cut-off D, the time step Δt of the Trotter decomposition and the number of available states per site σ for a few modulation frequencies across the range of absorption. We compute the relative error on the energy $E_j(t)$ when varying the parameters Δt, D and σ and choose the parameter values for our analysis such that the relative error is sufficiently small when varying to a value that would give more precise results. We define the relative error at a certain time t when changing one of the preceding parameters $param$ between values $param = val_a$ and $param = val_b$, while all other parameters are kept fixed, as

$$e_{\mathrm{rel}}^{param}(t) = \frac{(E_j(t, val_a) - E_j(t, val_b))}{E_j(t, val_b)}, \tag{A.1}$$

where val_b is the value that would give better results. We determine the relative error at the time $t_{\max}$ which is the upper bound of the fitting range. We also consider the relative error when varying the system length L to a larger value and the site j to a neighbouring one that is likewise odd or even in order to verify that we can separate bulk properties from boundary effects.
For $U/J = 20$ we choose a fitting range of $t = [1, t_{\max} = 4]$. The variation of parameters Δt, D, σ, L and j are summarized in Table A.1. The first column val_a contains the parameters used for our analysis. The second column contains the parameters val_b that we vary to when determining the relative error. Note, that at each variation of one of the parameters from val_a to val_b all others are kept fix at val_a. The corresponding relative errors are given in Table A.2. We conclude that $E_j(t)$, for $L = 30$ at site $j = 15$, gives satisfactorily precise results for parameters $\Delta t = 0.01$, $D = 128$ and $\sigma = 3$. Additionally, we can separate bulk properties from boundary effects.
For $U/J = 4$ we choose a fitting range of $t = [1, t_{\max} = 6]$. The variation of parameters Δt, D, σ, L and j are summarized in Table A.3 and the corresponding relative errors are given in Table A.4. We find that $E_j(t)$, for $L = 40$ at site $j = 20$, gives satisfactorily precise results for parameters $\Delta t = 0.05$, $D = 128$ and $\sigma = 7$.

Errors on the energy absorption rate We follow the procedure explained in Section 3.2.1 for a few frequencies ω across the range of absorption. We determine the leading

parameter	val_a	val_b
Δt	0.01	0.005
D	128	196
σ	3	5
L	30	50
j	15	13

Table A.1. – Variation of parameters chosen to test the convergence of $E_j(t)$ at a time $t_{\max} = 4$ for $U/J = 20$. Note, that at each variation of one of the parameters from val_a to val_b all others are kept fix at val_a.

ω	$e_{\text{rel}}^{\Delta t}(t_{\max})$	$e_{\text{rel}}^{D}(t_{\max})$	$e_{\text{rel}}^{\sigma}(t_{\max})$	$e_{\text{rel}}^{L}(t_{\max})$	$e_{\text{rel}}^{j}(t_{\max})$
19	$1.2 \cdot 10^{-2}$	$3.0 \cdot 10^{-5}$	$4.3 \cdot 10^{-2}$	$7.4 \cdot 10^{-3}$	$2.3 \cdot 10^{-2}$
20	$7.2 \cdot 10^{-3}$	$1.6 \cdot 10^{-5}$	$2.2 \cdot 10^{-2}$	$5.0 \cdot 10^{-3}$	$2.1 \cdot 10^{-2}$
21	$1.0 \cdot 10^{-2}$	$2.4 \cdot 10^{-5}$	$1.2 \cdot 10^{-2}$	$7.1 \cdot 10^{-3}$	$3.2 \cdot 10^{-2}$
22	$1.4 \cdot 10^{-2}$	$1.2 \cdot 10^{-5}$	$4.4 \cdot 10^{-3}$	$8.1 \cdot 10^{-3}$	$2.6 \cdot 10^{-2}$

Table A.2. – The relative errors $e_{\text{rel}}^{param}(t_{\max})$ on $E_j(t_{\max})$ for $U/J = 20$ when varying the parameter *param* from val_a to val_b as given in A.1.

parameter	val_a	val_b
Δt	0.05	0.01
D	128	196
σ	7	9
L	40	60
j	20	18

Table A.3. – Variation of parameters chosen to test the convergence of $E_j(t)$ at a time $t_{\max} = 6$ for $U/J = 4$. Note, that at each variation of one of the parameters from val_a to val_b all others are kept fix at val_a.

ω $[J]$	$e_{\text{rel}}^{\Delta t}(t_{\max})$	$e_{\text{rel}}^{D}(t_{\max})$	$e_{\text{rel}}^{\sigma}(t_{\max})$	$e_{\text{rel}}^{L}(t_{\max})$	$e_{\text{rel}}^{j}(t_{\max})$
4.1	$1.0 \cdot 10^{-2}$	$2.0 \cdot 10^{-5}$	$4.5 \cdot 10^{-6}$	$3.8 \cdot 10^{-3}$	$2.5 \cdot 10^{-3}$
5	$4.8 \cdot 10^{-3}$	$3.2 \cdot 10^{-4}$	$2.2 \cdot 10^{-5}$	$3.5 \cdot 10^{-3}$	$2.3 \cdot 10^{-3}$
5.9	$6.1 \cdot 10^{-3}$	$8.7 \cdot 10^{-4}$	$1.6 \cdot 10^{-5}$	$5.5 \cdot 10^{-3}$	$3.4 \cdot 10^{-3}$
6.8	$1.7 \cdot 10^{-2}$	$2.5 \cdot 10^{-3}$	$4.6 \cdot 10^{-4}$	$9.3 \cdot 10^{-3}$	$5.0 \cdot 10^{-3}$
7.7	$3.7 \cdot 10^{-2}$	$5.7 \cdot 10^{-3}$	$3.1 \cdot 10^{-4}$	$6.1 \cdot 10^{-3}$	$6.8 \cdot 10^{-3}$
8.6	$1.4 \cdot 10^{-2}$	$4.1 \cdot 10^{-3}$	$2.2 \cdot 10^{-4}$	-	$3.4 \cdot 10^{-3}$

Table A.4. – The relative errors $e_{\text{rel}}^{param}(t_{\max})$ on $E_j(t_{\max})$ for $U/J = 4$ when varying the parameter *param* from val_a to val_b as given in A.3.

ω $[J]$	dominant $e_{\mathrm{rel}}^{param}(t_{\max})$	m	Δ_{num}	Δ_{fit}	Δ_{range}
19	$e_{\mathrm{rel}}^{\sigma}(t_{\max}) = 4.3 \cdot 10^{-2}$	0.19	$8.2 \cdot 10^{-3}$	$5.8 \cdot 10^{-3}$	$4.6 \cdot 10^{-3}$
20	$e_{\mathrm{rel}}^{\sigma}(t_{\max}) = 2.2 \cdot 10^{-2}$	0.33	$1.7 \cdot 10^{-2}$	$1.1 \cdot 10^{-2}$	$1.3 \cdot 10^{-2}$
21	$e_{\mathrm{rel}}^{j}(t_{\max}) = 3.2 \cdot 10^{-2}$	0.36	$5.1 \cdot 10^{-3}$	$5.5 \cdot 10^{-3}$	$1.5 \cdot 10^{-2}$
22	$e_{\mathrm{rel}}^{j}(t_{\max}) = 2.6 \cdot 10^{-2}$	0.22	$4.2 \cdot 10^{-3}$	$9.7 \cdot 10^{-3}$	$7.3 \cdot 10^{-3}$

Table A.5. – For different ω across the range of absorption for $U/J = 20$ we summarize the dominant relative error $e_{\mathrm{rel}}^{param}(t_{\max})$ on $E_j(t)$, the fitted energy absorption rate m and the errors on m given by Δ_{num}, Δ_{fit} and Δ_{range}. These errors are of similar magnitude. The largest of these three errors is used for the errorbars in Figure 3.2a.

ω $[J]$	dominant $e_{\mathrm{rel}}^{param}(t_{\max})$	m	Δ_{num}	Δ_{fit}	Δ_{range}
4.1	$e_{\mathrm{rel}}^{\Delta t}(t_{\max}) = 1.0 \cdot 10^{-2}$	$0.61 \cdot 10^{-2}$	$6.2 \cdot 10^{-5}$	$7.4 \cdot 10^{-4}$	$4.3 \cdot 10^{-4}$
5.0	$e_{\mathrm{rel}}^{\Delta t}(t_{\max}) = 4.8 \cdot 10^{-3}$	$1.5 \cdot 10^{-2}$	$7.8 \cdot 10^{-5}$	$9.0 \cdot 10^{-4}$	$3.0 \cdot 10^{-4}$
5.9	$e_{\mathrm{rel}}^{\Delta t}(t_{\max}) = 6.1 \cdot 10^{-3}$	$2.1 \cdot 10^{-2}$	$2.9 \cdot 10^{-4}$	$9.6 \cdot 10^{-4}$	$3.8 \cdot 10^{-4}$
6.8	$e_{\mathrm{rel}}^{\Delta t}(t_{\max}) = 1.7 \cdot 10^{-2}$	$2.9 \cdot 10^{-2}$	$7.8 \cdot 10^{-4}$	$9.8 \cdot 10^{-4}$	$9.6 \cdot 10^{-4}$
7.7	$e_{\mathrm{rel}}^{\Delta t}(t_{\max}) = 3.7 \cdot 10^{-2}$	$3.4 \cdot 10^{-2}$	$1.0 \cdot 10^{-3}$	$1.5 \cdot 10^{-3}$	$5.6 \cdot 10^{-4}$
8.6	$e_{\mathrm{rel}}^{\Delta t}(t_{\max}) = 1.4 \cdot 10^{-2}$	$1.3 \cdot 10^{-2}$	$4.4 \cdot 10^{-4}$	$1.6 \cdot 10^{-3}$	$1.4 \cdot 10^{-3}$

Table A.6. – For different ω across the range of absorption for $U/J = 4$ we summarize the dominant relative error $e_{\mathrm{rel}}^{param}(t_{\max})$ on $E_j(t)$, the fitted energy absorption rate m and the errors on m given by Δ_{num}, Δ_{fit} and Δ_{range}. Δ_{fit} and Δ_{range} are of same order of magnitude whereas Δ_{num} is one order of magnitude smaller. The largest error is Δ_{fit} for all ω. This error is displayed by the errorbars in Figure 3.2b.

relative error on $E_j(t)$ from a change in parameters Δt, D, σ, L and j and then determine the errors Δ_{fit}, Δ_{range} and Δ_{num} on $m = (1/L) \cdot \overline{dE(t)}/dt$ defined in 3.2.1. The results for $U/J = 20$ and $U/J = 4$ are summarized in Tables A.5 and A.6 respectively. The errorbars presented in Figure 3.2 display the largest of the three errors. For $U/J = 20$ all errors are on the same order of magnitude and the dominating error differs between different ω. For $U/J = 4$ the dominating error is Δ_{fit} for all ω.

Appendix B.

Numerical bandstructure calculation

We carry out a numeric bandstructure calculation for the optical lattice $V_0(x) = V_g \cos^2(k_g x) - V_g/2$ with parameters introduced in Section 4.4.1 and determine the energy bands as well as the corresponding Bloch functions. We need this for the detailed analysis of the experimental implementation in Section 4.4. We rewrite the Schrödinger equation for a particle in a periodic potential $V_0(x)$ given by Equation (4.151) for the periodic function $u_{nk}(x)$ defined through Equation (4.153),

$$\left(\frac{\hbar^2}{2m}(k^2 - 2ik\partial_x + \partial_x^2) + V_0(x)\right) u_{nk}(x) = E_{nk}(x) u_{nk}(x). \tag{B.1}$$

The potential $V_0(x)$ and the function $u_{nk}(x)$ have the same periodicity which is given by the lattice spacing of the optical lattice $a = \lambda_g/2 = \pi/k_g$ such that the first Brillouin zone of the reciprocal lattice is $(k_g, k_g]$. This is equivalent to the Brillouin zone being $(-\pi, \pi]$ in the tight-binding picture. Note that the momentum transfer $\Delta k = \pi$ is now given by $\Delta k = k_g$. Due to the periodicity we can write $V_0(x)$ and $u_{nk}(x)$ as Fourier sums of the reciprocal lattice vector $2k_g$,

$$V_0(x) = \sum_r V_r e^{ix2k_g r} = V_g \cos^2(k_g x) - \frac{V_g}{2} = \frac{V_g}{4}\left(e^{2ik_g x} + e^{-2ik_g x} - 2\right), \tag{B.2}$$

$$u_{nk}(x) = \sum_l c_l^{nk} e^{ix2k_g l}. \tag{B.3}$$

From the first line it follows $V_{r=+1} = V_{r=-1} = V_g/4$ and we set $V_{r=0} = 0$. Substituting into the Schrödinger equation B.1 yields

$$\sum_{l'}\left(\frac{(\hbar k + 2\hbar k_g l')^2}{2m} c_{l'}^{nk}\delta_{l,l'} + V_{l-l'} c_{l'}^{nk}\right) = E_n(k) c_l^{nk}, \tag{B.4}$$

which can be written in matrix form

$$\sum_{l'} H_{l,l'} c_{l'}^{nk} = E_n(k) c_l^{nk}, \tag{B.5}$$

with

$$H_{l,l'} = \begin{cases} \left(\frac{k}{k_g} + 2l'\right)^2 E_r^{\text{green}}, & l = l' \\ \frac{V_g}{4}, & |l - l'| = 1 \\ 0, & \text{else} \end{cases}, \tag{B.6}$$

with the recoil energy $E_r^{\text{green}} = 4E_r^{\text{red}}$, $E_r^{\text{red}} = \hbar^2 k_r^2/2m$ (see Section 4.4.1). We numerically diagonalize the Hamiltonian matrix to obtain the eigenenergies $E_n(k)$ and the

corresponding vectors c^{nk} that define the Bloch function through Equations (B.3) and (4.153). The coefficients c^{nk} become sufficiently small for large $|l|$ such that we can truncate the Hamiltonian in order to carry out the diagonalization. For the lowest bands $l = -5, 4, ..., 5$ is a reasonable choice. We discretize $k = -k_g + 2k_g j/100$, $j = 1, ..., 100$. The bandstructure and the corresponding Bloch functions for our particular lattice setup with $V_g = 40E_r^{\text{red}} = 2.9 \cdot 10^{-30}$J are shown in Figure B.1.

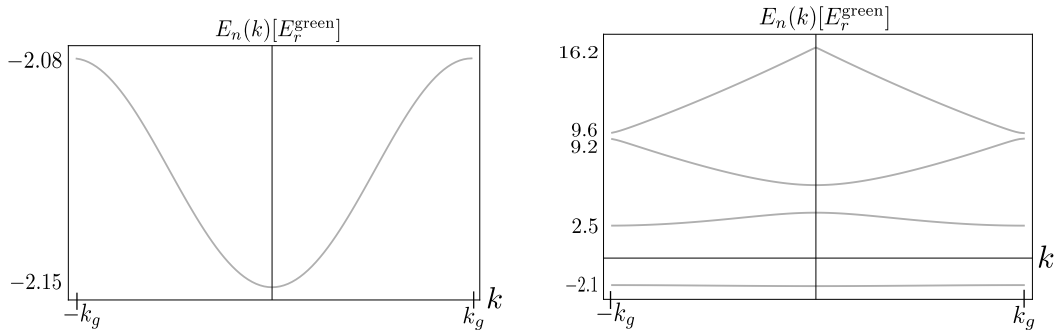

(a) lowest band $n = 1$ **(b)** bands $n = 1 - 4$

Figure B.1. – Bandstructure $E_n(k)$ of the equilibrium lattice $V_0(x) = V_g \cos^2(k_g x) - V_g/2$ in units of the recoil energy $E_r^{\text{green}} = 1.17 \cdot 10^{-29}$J for a lattice depth of $V_g = 40E_r^{\text{red}} = 10E_r^{\text{green}}$.

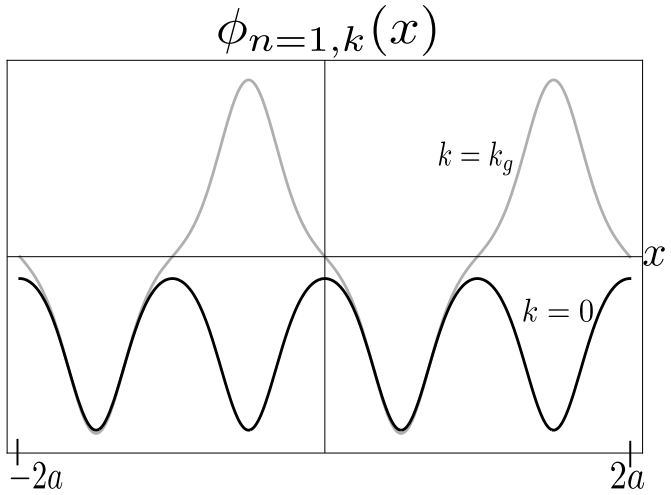

Figure B.2. – Bloch functions of the lowest band $n = 1$ of the equilibrium lattice $V_0(x) = V_g \cos^2(k_g x) - V_g/2$ for quasimomentum $k = 0$ (black) and $k = k_g$ (grey).

Appendix C.

The response in Bloch basis representation

In this appendix we compute the response in Bloch basis representation which is given in Section 4.3 without derivation. We use the spectral representation given by Equation (2.14),

$$\mathrm{Im}\chi_{OO^\dagger}(\omega) = -\frac{\pi}{Z}\sum_{n,m}|\langle m|O|n\rangle|^2 e^{-\beta(E_n-\mu N)}\delta\left(\omega-(E_m-E_n)\right)\left(1-e^{-\beta\omega}\right). \quad \text{(C.1)}$$

Here, the many body states $|n\rangle$ are given by $|n\rangle = \prod_{\{k\}} c_k^\dagger|0\rangle$ where $|0\rangle$ is the vacuum and $c_k^\dagger$ creates a particle in Bloch state k. The product runs over all possible configurations of different k denoted by $\{k\}$. We insert the perturbing operator O in Bloch basis given by Equation (4.157) and constrain the calculation to $\Delta k = k_g$ since the calculation for all Δk is analogous but less clear in notation. We obtain

$$\mathrm{Im}\chi_{OO^\dagger}(\omega) = -\frac{\pi}{Z}\sum_{n,m}\Big|\sum_k M_{k\to k+k_g}\langle m|c_{k+k_g}^\dagger c_k|n\rangle + M_{k\to k+k_g}^*\langle m|c_k^\dagger c_{k+k_g}|n\rangle\Big|^2\cdot \quad \text{(C.2)}$$

$$\cdot\, e^{-\beta(E_n-\mu N)}\delta\big(\omega-(E_m-E_n)\big)\left(1-e^{-\beta\omega}\right) \quad \text{(C.3)}$$

$$= -\frac{\pi}{Z}\left(1-e^{-\beta\omega}\right)\sum_{n(k)}|M_{k\to k+k_g}+M_{k\to k+k_g}^*|^2\langle n|c_{k+k_g}^\dagger c_k|m\rangle\cdot \quad \text{(C.4)}$$

$$\cdot\,\langle m|c_k^\dagger c_{k+k_g}|n\rangle e^{-\beta(E_n-\mu N)}\delta\big(\omega-(E_m-E_n)\big) \quad \text{(C.5)}$$

$$= -\pi\left(1-e^{-\beta\omega}\right)\sum_k 4|M_{k\to k+k_g}|^2 f\big(E(k+k_g)-\mu\big)\cdot \quad \text{(C.6)}$$

$$\cdot\left(1-f\big(E(k)-\mu\big)\right)\delta\Big(\omega-\big(E(k)-E(k+k_g)\big)\Big) \quad \text{(C.7)}$$

$$= -4\pi\sum_k|M_{k\to k+k_g}|^2\left(1-e^{-\beta(E(k)-E(k+k_g))}\right)f\big(E(k+k_g)-\mu\big)\cdot \quad \text{(C.8)}$$

$$\cdot\left(1-f\big(E(k)-\mu\big)\right)\delta\Big(\omega-\big(E(k)-E(k+k_g)\big)\Big) \quad \text{(C.9)}$$

$$= -4\pi\sum_k|M_{k\to k+k_g}|^2\Big(f\big(E(k+k_g)-\mu\big)-f\big(E(k)-\mu\big)\Big)\cdot \quad \text{(C.10)}$$

$$\cdot\,\delta\Big(\omega-\big(E(k)-E(k+k_g)\big)\Big) \quad \text{(C.11)}$$

$$= -4\delta\sum_k|M_{k\to k+k_g}|^2\Big(f\big(E(k+k_g)-\mu\big)-f\big(E(k)-\mu\big)\Big)\cdot \quad \text{(C.12)}$$

$$\cdot\,\frac{1}{\delta^2+\big(\omega-(E(k)-E(k+k_g))\big)^2}\cdot \quad \text{(C.13)}$$

Note that in step 2 we reduce to a sum over $n(k)$ as for a certain k there is only one matching pair of $|n\rangle$ and $|m\rangle$ which gives non-zero expectation values. In step 3 we use

$\langle n|c^\dagger_{k+k_g}c_k|m\rangle\cdot\langle m|c^\dagger_k c_{k+k_g}|n\rangle\cdot e^{-\beta(E_n-\mu N)}/Z = f\big(E(k+k_g)-\mu\big)\cdot\Big(1-f\big(E(k)-\mu\big)\Big)$ and replace by a sum over k. In step 4 we insert the resonance frequeny $\omega = E(k)-E(k+k_g)$. We then simplify. Note that in the last line δ is an infinitesimal parameter and no longer the δ-function. Analogous calculations yield the response including all k'

$$\mathrm{Im}\chi_{OO^\dagger}(\omega) = -4\delta\sum_{k,k'}|M_{k\to k'}|^2\Big(f\big(E(k)-\mu\big)-f\big(E(k')-\mu\big)\Big)\cdot \tag{C.14}$$

$$\cdot\,\frac{1}{\delta^2+\big(\omega-(E(k')-E(k))\big)^2}\cdot \tag{C.15}$$

Including excitations to higher bands we analogously obtain

$$\mathrm{Im}\chi_{OO^\dagger}(\omega) = -\pi\sum_{k}|M_{n=1,k\to n'\neq 1,k'}|^2\Big(f\big(E_1(k)-\mu\big)-f\big(E_{n'}(k')-\mu\big)\Big)\cdot \tag{C.16}$$

$$\cdot\,\delta\Big(\omega-\big(E_{n'}(k')-E_1(k)\big)\Big) \tag{C.17}$$

$$= -\delta\sum_{k}|M_{n=1,k\to n'\neq 1,k'}|^2\Big(f\big(E_1(k)-\mu\big)-f\big(E_{n'}(k')-\mu\big)\Big)\cdot \tag{C.18}$$

$$\cdot\,\frac{1}{\delta^2+\big(\omega-(E_{n'}(k')-E_1(k))\big)^2}\cdot \tag{C.19}$$

Appendix D.

Two representations of the transfer matrix element: Bloch basis and Wannier basis

In Section 4.4.3 we show that the tight-binding representation of the perturbation, i.e. $O = \sum_j (-1)^j (c_j^\dagger c_{j+1} + \text{h.c.}) = \sum_k (\exp(i(k+\pi)) c_k^\dagger c_{k+\pi} + \text{h.c})$ as introduced in Section 1.3, is a good approximation in the case of the particular lattice setup specified in Section 4.4.1. We do so by comparing the response function in Bloch basis representation, Equation (4.162), for the particular lattice setup with the help of numeric bandstructre calculations (Appendix B) to the tight-binding result from Section 4.1.2. In this Appendix we relate the Bloch basis representation from Section 4.3 to the tight-binding representation in order to show that a direct comparison is possible.
The tight-binding Hamiltonian (1.19) is obtained by writing the Hamiltonian H_1 (4.151) and the perturbing potential $\delta V(x,t)$ 1.17 in second quantized form in the Wannier basis representation. Wannier functions $w_n(x - x_j)$ are maximally localized on individual lattice sites j at position $x_j = aj$ in contrast to Bloch functions $\phi_{nk}(x)$ (4.153) that are delocalized over the entire lattice. The Wannier functions can be constructed from the Bloch functions and constitute an orthonormal basis,

$$w_n(x - x_j) = \frac{1}{\sqrt{N}} \sum_k e^{-ikx_j} \phi_{nk}(x), \tag{D.1}$$

where N is a normalization constant. We choose the notation $w_n(x - x_j)$ or $|nj\rangle$. The equilibrium Hamiltonian in second quantization is given by

$$H = \sum_{njn'j'} \langle n'j'|H_1|nj\rangle c_{n'j'}^\dagger c_{nj} \tag{D.2}$$

$$\approx -J \sum_j (c_{j+1}^\dagger c_j + \text{h.c.}), \tag{D.3}$$

where H_1 is given by Equation (4.151). The tight-binding Hamiltonian in the second line is obtained by only considering the lowest band and nearest-neighbor tunneling. The tunneling matrix element is given by

$$J = -\langle n = 1, j+1|H_1|n = 1, j\rangle \tag{D.4}$$

$$= -\int \mathrm{d}x \; w^*(x - x_{j+1}) H_1 w(x - x_j). \tag{D.5}$$

The perturbing operator in the Wannier basis representation is given by

$$O = \sum_{njn'j'} \langle n'j'|\tilde{V}(x)|nj\rangle c^\dagger_{n'j'} c_{nj} \tag{D.6}$$

$$\approx \sum_j (-1)^j (c^\dagger_j c_{j+1} + \text{h.c.}) \tag{D.7}$$

$$= \sum_k (e^{i(k+\pi)} c^\dagger_k c_{k+\pi} + \text{h.c}), \tag{D.8}$$

where $\tilde{V}(x)$ the time-independent part of the perturbing potential 1.17 and we set the lattice spacing $a \equiv 1$. For the time being, the tight-binding representation of the perturbing operator is an assumption. It neglects higher bands and only considers nearest-neighbor tunneling processes. This leads to a k-selective coupling after Fourier transformation $c_j = (1/\sqrt{V}) \sum_k \exp(ikaj) c_k$.
Quite generally, the Fourier transformation can be written in the following form (we neglect the band index for now)

$$O = \sum_{jj'} \langle j'|\tilde{V}(x)|j\rangle c^\dagger_{j'} c_j \tag{D.9}$$

$$= \begin{cases} \frac{1}{V} \sum_{jj'} \sum_{kk'} \langle j'|\tilde{V}(x)|j\rangle e^{i(jk-j'k')} c^\dagger_{k'} c_k \\ \sum_{jj'} \sum_{kk'} \langle j'|k'\rangle \langle k'|\tilde{V}(x)|k\rangle \langle k|j\rangle c^\dagger_{j'} c_j \end{cases} \tag{D.10}$$

$$= \sum_{kk'} \langle k'|\tilde{V}(x)|k\rangle \sum_j \langle j'|k'\rangle c^\dagger_{j'} \sum_j \langle k|j\rangle c_j \tag{D.11}$$

$$= \sum_{kk'} \langle k'|\tilde{V}(x)|k\rangle c^\dagger_{k'} c_k \tag{D.12}$$

$$= \sum_{kk'} M_{k\to k'} c^\dagger_{k'} c_k. \tag{D.13}$$

We identify $c_k = \sum_j \langle k|j\rangle c_j$, $\langle k|j\rangle = (1/\sqrt{V}) \exp(-ikaj)$ and the transfer matrix element in Wannier basis

$$M_{k\to k'} = \langle k'|\tilde{V}(x)|k\rangle = \frac{1}{V} \sum_{jj'} \langle j'|\tilde{V}(x)|j\rangle e^{i(jk-j'k')}. \tag{D.14}$$

In the following we will show that $M_{k\to k'}$ are equivalent in Bloch -and Wannier basis such that the tight-binding approximation may be verified by computing the transfer matrix elements in Bloch basis which is carried out in Section 4.4.3.
We restrict the proof to the lowest band. We denote Wannier states by $|j\rangle$, Fourier transformed Wannier states by $|k\rangle$ and Bloch states of quasimomentum $\tilde{k}$ by $|\tilde{k}\rangle$. We

start with the transfer matrix element in Wannier basis representation.

$$\langle k'|\tilde{V}(x)|k\rangle = \sum_{jj'}\langle k'|j'\rangle\langle j'|\tilde{V}|j\rangle\langle j|k\rangle \tag{D.15}$$

$$= \sum_{jj'}\langle k'|j'\rangle\langle j|k\rangle \int \mathrm{d}x\ w^*(x-x_{j'})\tilde{V}w(x-x_j) \tag{D.16}$$

$$= \sum_{jj'}\sum_{\tilde{k}\tilde{k}'}\langle k'|j'\rangle\langle j|k\rangle e^{i(\tilde{k}'x_{j'}-\tilde{k}x_j)}\frac{1}{V}\int \mathrm{d}x\ \phi^*_{\tilde{k}'}(x)\tilde{V}\phi_{\tilde{k}}(x) \tag{D.17}$$

$$= \sum_{jj'}\sum_{\tilde{k}\tilde{k}'}\frac{1}{V}e^{-ik'aj'}e^{ikaj}e^{i\tilde{k}'x_{j'}}e^{-i\tilde{k}x_j}\frac{1}{V}\int \mathrm{d}x\ \phi^*_{\tilde{k}'}(x)\tilde{V}\phi_{\tilde{k}}(x) \tag{D.18}$$

$$= \sum_{\tilde{k}\tilde{k}'}\delta_{k,\tilde{k}}\delta_{k',\tilde{k}'}\int \mathrm{d}x\ \phi^*_{\tilde{k}'}(x)\tilde{V}\phi_{\tilde{k}}(x) \tag{D.19}$$

$$= \int \mathrm{d}x\phi^*_{\tilde{k}'}(x)\tilde{V}\phi_{\tilde{k}}(x) \tag{D.20}$$

$$= \langle\tilde{k}'|\tilde{V}|\tilde{k}\rangle. \tag{D.21}$$

We finish with the matrix element in Bloch basis representation which completes the proof. We used $w(x-x_j) = (1/\sqrt{V})\sum_k \exp(-i\tilde{k}x_j)\phi_{\tilde{k}}(x)$ in step 3, setting $a \equiv 1$, $x_j = aj \equiv j$, $\langle k|j\rangle = (1/\sqrt{V})\exp(-ikaj)$ in step 4 and $\sum_{jj'}\exp(ij(k-\tilde{k}))\exp(ij'(\tilde{k}'-k')) = V^2\delta_{k,\tilde{k}}\delta_{k',\tilde{k}'}$ in step 5.

Bibliography

[1] M. R. Matthews C. E. Wieman E. A. Cornell M. H. Anderson, J. R. Ensher. Observation of Bose-Einstein condensation in a dilute atomic vapor. *Science*, 269(5221):198–201, 1995.

[2] C. C. Bradley, C. A. Sackett, J. J. Tollett, and R. G. Hulet. Evidence of Bose-Einstein condensation in an atomic gas with attractive interactions. *Phys. Rev. Lett.*, 75:1687–1690, Aug 1995.

[3] K. B. Davis, M. O. Mewes, M. R. Andrews, N. J. van Druten, D. S. Durfee, D. M. Kurn, and W. Ketterle. Bose-Einstein condensation in a gas of sodium atoms. *Phys. Rev. Lett.*, 75:3969–3973, Nov 1995.

[4] B. DeMarco and D. S. Jin. Onset of Fermi degeneracy in a trapped atomic gas. *Science*, 285(5434):1703–1706, 1999.

[5] I. Bloch, J. Dalibard, and W. Zwerger. Many-body physics with ultracold gases. *Rev. Mod. Phys.*, 80:885–964, Jul 2008.

[6] C. Orzel, A. K. Tuchman, M. L. Fenselau, M. Yasuda, and M. A. Kasevich. Squeezed states in a Bose-Einstein condensate. *Science*, 291(5512):2386–2389, 2001.

[7] M. Greiner, O. Mandel, T. Esslinger, T. W. Hänsch, and I. Bloch. Quantum phase transition from a superfluid to a Mott insulator in a gas of ultracold atoms. *Nature*, 415:39–44, 2002.

[8] D. Jaksch, C. Bruder, J. I. Cirac, C. W. Gardiner, and P. Zoller. Cold bosonic atoms in optical lattices. *Phys. Rev. Lett.*, 81:3108–3111, Oct 1998.

[9] R. Jördens, N. Strohmaier, K. Günter, H. Moritz, and T. Esslinger. A Mott insulator of fermionic atoms in an optical lattice. *Nature*, 455:204–207, 2008.

[10] U. Schneider, L. Hackermüller, S. Will, Th. Best, I. Bloch, T. A. Costi, R. W. Helmes, D. Rasch, and A. Rosch. Metallic and insulating phases of repulsively interacting fermions in a 3d optical lattice. *Science*, 322(5907):1520–1525, 2008.

[11] Richard P. Feynman. Simulating physics with computers. *Int. J. Theor. Phys.*, 21:467–488, 1982.

[12] S. Trotzky, L. Pollet, F. Gerbier, U. Schnorrberger, I. Bloch, N.V. Prokof'ev, B. Svistunov, and M. Troyer. Suppression of the critical temperature for superfluidity near the Mott transition: validating a quantum simulator. *Nature*, 6:998–1004, 2010.

[13] M. Lewenstein, A. Sanpera, V. Ahufinger, B. Damski, A. Sen(De), and U. Sen. Ultracold atomic gases in optical lattices: mimicking condensed matter physics and beyond. *Advances in Physics*, 56(2):243, 2007.

[14] T. Stöferle, H. Moritz, C. Schori, M. Köhl, and T. Esslinger. Transition from a strongly interacting 1d superfluid to a Mott insulator. *Phys. Rev. Lett.*, 92:130403, 2004.

[15] U. Bissbort, S. Götze, Y. Li, J. Heinze, J. S. Krauser, M. Weinberg, C. Becker, K. Sengstock, and W. Hofstetter. Detecting the amplitude mode of strongly interacting lattice bosons by Bagg scattering. *Phys. Rev. Lett.*, 106:205303, May 2011.

[16] M. Endres, T. Fukuhara, D. Pekker, M. Cheneau, P. Schauß, C. Gross, E. Demler, S. Kuhr, and I. Bloch. The 'Higgs' amplitude mode at the two-dimensional superfluid-Mott insulator transition. *Nature*, 487:454, 2012.

[17] A. Iucci, M. A. Cazalilla, A. F. Ho, and T. Giamarchi. Energy absorption of a Bose gas in a periodically modulated optical lattice. *Phys. Rev. A*, 73:041608, Apr 2006.

[18] Matthew P. A. Fisher, Peter B. Weichman, G. Grinstein, and Daniel S. Fisher. Boson localization and the superfluid-insulator transition. *Phys. Rev. B*, 40:546–570, Jul 1989.

[19] J. K. Freericks and H. Monien. Phase diagram of the Bose-Hubbard model. *Europhysics Letters*, 26(7):545, 1994.

[20] T. D. Kühner and H. Monien. Phases of the one-dimensional Bose-Hubbard model. *Phys. Rev. B*, 58:R14741–R14744, Dec 1998.

[21] D. Pertot, A. Sheikhan, E. Cocchi, L. A. Miller, J. E. Bohn, M. Koschorreck, M. Köhl, and C. Kollath. Relaxation dynamics of a Fermi gas in an optical superlattice. *Phys. Rev. Lett.*, 113:170403, Oct 2014.

[22] W. Hofstetter, J. I. Cirac, P. Zoller, E. Demler, and M. D. Lukin. High-temperature superfluidity of fermionic atoms in optical lattices. *Phys. Rev. Lett.*, 89:220407, Nov 2002.

[23] T. Stöferle K. Günter M. Köhl, H. Moritz and T. Esslinger. Fermionic atoms in a three dimensional optical lattice: Observing Fermi surfaces, dynamics, and interactions. *Phys. Rev. Lett.*, 94:080403, 2005.

[24] R. Grimm, M. Weidemüller, and Y. B. Ovchinnikov. Optical dipole traps for neutral atoms. *Adv. At. Mol. Opt. Phys.*, 42:95, 2000.

[25] M. Greiner. *Ultracold quantum gases in three-dimensional optical lattice potentials.* PhD thesis, Ludwig-Maximilians-Universität München, 2003.

[26] N. W. Ashcroft and N. D. Mermin. *Solid State Physics.* Thomson Learning, 1976.

[27] W. Zwerger. Mott–Hubbard transition of cold atoms in optical lattices. *J. Opt. B: Quantum Semiclass. Opt.*, 5:9–16, 2003.

[28] V. A. Kashurnikov and B. V. Svistunov. Exact diagonalization plus renormalization-group theory: Accurate method for a one-dimensional superfluid-insulator-transition study. *Phys. Rev. B*, 53:11776–11778, May 1996.

[29] Till D. Kühner, Steven R. White, and H. Monien. One-dimensional Bose-Hubbard model with nearest-neighbor interaction. *Phys. Rev. B*, 61:12474–12489, May 2000.

[30] M. A. Cazalilla, R. Citro, T. Giamarchi, E. Orignac, and M. Rigol. One dimensional bosons: From condensed matter systems to ultracold gases. *Rev. Mod. Phys.*, 83:1405–1466, Dec 2011.

[31] J. Hubbard. Electron correlations in narrow energy bands. *Proc. R. Soc. Lond*, 276:238–257, Nov 1963.

[32] A. Georges and T. Giamarchi. Strongly correlated bosons and fermions in optical lattices. *arXiv:1308.2684*, 2013.

[33] Peter Barmettler and Corinna Kollath. Quantum gases in optical lattices . *arXiv:1312.5772*, 2013.

[34] L. De Leo, J. S. Bernier, C. Kollath, A. Georges, and V. W. Scarola. Thermodynamics of the three-dimensional Hubbard model: Implications for cooling cold atomic gases in optical lattices. *Phys. Rev. A*, 83:023606, Feb 2011.

[35] J. L. Basdevant and J. Dalibard. *Quantum Mechanics*. Springer, 2005.

[36] T. Giamarchi, A. Iucci, and C. Berthod. lecture notes: Introduction to many body physics, 2008-2013.

[37] Sara Bergkvist, Patrik Henelius, and Anders Rosengren. Local-density approximation for confined bosons in an optical lattice. *Phys. Rev. A*, 70:053601, Nov 2004.

[38] Steven R. White. Density matrix formulation for quantum renormalization groups. *Phys. Rev. Lett.*, 69:2863–2866, Nov 1992.

[39] Ulrich Schollwöck. The density-matrix renormalization group in the age of matrix product states. *Annals of Physics*, 326(1):96 – 192, 2011. January 2011 Special Issue.

[40] Peter Barmettler, Dario Poletti, Marc Cheneau, and Corinna Kollath. Propagation front of correlations in an interacting Bose gas. *Phys. Rev. A*, 85:053625, May 2012.

[41] J. J. Sakurai. *Modern Quantum Mechanics*. Addison-Wesley Publishing Company, 1994.

[42] Corinna Kollath. Time-adaptive density matrix renormalization group method –code by private communication.

[43] The MathWorks Incorporated. Confidence and Prediction Bounds. R2014b Documentation.

[44] W. Ketterle and M. W. Zwierlein. Making, probing and understanding ultracold Fermi gases. *arXiv: 0801.2500*, 2008.

[45] R. Jördens, L. Tarruell, D. Greif, T. Uehlinger, N. Strohmaler, H. Moritz, T. Esslinger, L. De Leo, C. Kollath, A. Georges, V. Scarola, L. Pollet, E. Burovski, E. Kozik, and M. Troyer. Quantitative determination of temperature in the approach to magnetic order of ultracold fermions in an optical lattice. *Phys. Rev. Lett.*, 104:180401, 2010.

[46] D. C. McKay and B. DeMarco. Cooling in strongly correlated optical lattices: prospects and challenges. *Rep. Prog. Phys.*, 74:054401, April 2011.

[47] C.J. Foot. *Atomic physics*. Oxford University Press, 2005.

[48] Ameneh Sheikhan. Exact diagonalization results and numeric band structure calculations by private communication.

[49] C. Cohen-Tannoudji, B. Diu, and F. Laloe. *Quantum Mechanics*, volume 2. Hermann and John Wiley And Sons, 1977.

[50] L. P. Pitaevskii and S. Stringari. *Bose-Einstein Condensation*. Oxford University Press, 2003.

[51] F. Werner, O. Parcollet, A. Georges, and S. R. Hassan. Interaction-induced adiabatic cooling and antiferromagnetism of cold fermions in optical lattices. *Phys. Rev. Lett.*, 95:056401, Jul 2005.

[52] L. D. Carr, G. V. Shlyapnikov, and Y. Castin. Achieving a BCS transition in an atomic Fermi gas. *Phys. Rev. Lett.*, 92:150404, Apr 2004.

[53] Lorenzo De Leo, Corinna Kollath, Antoine Georges, Michel Ferrero, and Olivier Parcollet. Trapping and cooling fermionic atoms into Mott and Néel states. *Phys. Rev. Lett.*, 101:210403, Nov 2008.

[54] C. Kollath, A. Iucci, I. P. McCulloch, and T. Giamarchi. Modulation spectroscopy with ultracold fermions in an optical lattice. *Phys. Rev. A*, 74(4):041604, Oct 2006.

[55] Qi Zhou and Tin-Lun Ho. Universal thermometry for quantum simulation. *Phys. Rev. Lett.*, 106:225301, May 2011.

[56] Jean-Sébastien Bernier, Tung-Lam Dao, Corinna Kollath, Antoine Georges, and Pablo S. Cornaglia. Thermometry and signatures of strong correlations from Raman spectroscopy of fermionic atoms in optical lattices. *Phys. Rev. A*, 81(6):063618, Jun 2010.

[57] J. Ruostekoski, C. J. Foot, and A. B. Deb. Light scattering for thermometry of fermionic atoms in an optical lattice. *Phys. Rev. Lett.*, 103:170404, Oct 2009.

[58] Karlo Penc and Frédéric Mila. Charge gap in the one-dimensional dimerized Hubbard model at quarter-filling. *Phys. Rev. B*, 50:11429–11445, Oct 1994.

[59] M. Tsuchiizu and A. Furusaki. Ground-state phase diagram of the one-dimensional half-filled extended Hubbard model. *Phys. Rev. B*, 69:035103, Jan 2004.

[60] S. Glocke, A. Klümper, and J. Sirker. Half-filled one-dimensional extended Hubbard model: Phase diagram and thermodynamics. *Phys. Rev. B*, 76:155121, Oct 2007.

[61] L. Tincani, R. M. Noack, and D. Baeriswyl. Critical properties of the band-insulator-to-Mott-insulator transition in the strong-coupling limit of the ionic Hubbard model. *Phys. Rev. B*, 79:165109, Apr 2009.

Erklärung

Hiermit versichere ich, dass ich die vorliegende Arbeit selbstständig verfasst und keine anderen als die angegebenen Quellen und Hilfsmittel benutzt habe, dass alle Stellen der Arbeit, die wörtlich oder sinngemäß aus anderen Quellen übernommen wurden, als solche kenntlich gemacht sind und dass die Arbeit in gleicher oder ähnlicher Form noch keiner Prüfungsbehörde vorgelegt wurde.

Köln, den 6. November 2014

Karla Loida